Alma Mater Studiorum-Università di Bologna

DOTTORATO DI RICERCA IN
INGEGNERIA BIOMEDICA, ELETTRICA E DEI SISTEMI

Ciclo 34

Settore Concorsuale: 09/E2 - INGEGNERIA DELL'ENERGIA ELETTRICA

Settore Scientifico Disciplinare: ING-IND/33 - SISTEMI ELETTRICI PER L'ENERGIA

PARTICIPATION OF WIND POWER PLANTS IN POWER SYSTEM STABILITY

Presentata da: James Amankwah Adu

Coordinatore Dottorato

Michele Monaci

Supervisore

Carlo Alberto Nucci

Co-supervisore
Alberto Borghetti

Esame finale anno 2022

“Good name in man and woman, dear my lord,

Is the immediate jewel of their souls.

Who steals my purse steals trash; 'tis something, nothing:

'Twas mine, 'tis his, and has been slave to thousands:

But he that filches from me my good name

Robs me of that which not enriches him,

And makes me poor indeed.”

Iago

Ai miei genitori

(To my parents)

Acknowledgment

I am greatly thankful to the members of the LISEP laboratory of the University of Bologna; my main supervisor Prof. Carlo Alberto Nucci, my co-supervisor Prof. Alberto Borghetti, my co-supervisor Prof. Fabio Napolitano particularly for what concerns the results achieved within the OSMOSE H2020 research project, Eng. Fabio Tossani and my colleagues of the PhD program. The thesis presented here is the result of a collective work that would not have been possible otherwise. In many cases the teachings, especially those coming from my tutors, went beyond the scientific field.

I would like to thank Hitachi Central Research Laboratory in Tokyo, Japan, who have welcomed me during my period abroad and have allowed me to expand my knowledge, professional vision and experience.

With much affection, I want to thank all the people that contributed in many ways to my maturement as a person and as a professional and who allowed me to maintain my intentions during the tough path that the doctorate represents.

Most importantly, I am greatly thankful to my parents, brothers and sisters for their support, understanding, patience and love. Also, to Angela Osei for all her immense love and support throughout these past three years.

I dedicate this work to my parents Kwadwo Adu-Atwenewa and Comfort Abena Agyeiwaah.

Abstract

The integration of large amounts of wind power in power systems coupled with the increasing replacement of large conventional synchronous generators (SGs) by wind power plants (WPPs) presents a considerable impact on power system stability. This is partly because most WPPs, particularly variable speed wind turbine (VSWT) types, are connected to the network via power converters which decouples their output power from the grid frequency, and this results in considerable loss of system inertia. Also, VSWTs are in general operated at the maximum power point tracking (MPPT), which makes them unable to increase their output power beyond the maximum power level for long-term frequency support. For this reason, it is important to develop control techniques that enable WPPs to participate in power system stability improvement. In literature, several studies have been reported on the frequency control provision of a wind turbines (WT), mainly classified into two categories: inertial response (IR) and primary frequency response (PFR).

This work investigates the IR and PFR capabilities of VSWTs; the control schemes are presented in detail and the required energy buffers also discussed.

For the IR, the electrostatic energy (EE) stored in the dc-link capacitors and the kinetic energy (KE) reserve of the WT rotors are utilised. Concerning the IR exploitation of the dc-link capacitors EE, two major architectures have been proposed, verified via simulations and their merits and demerits clearly identified. The PFR service is guaranteed by a deloading scheme that reserves a portion of the maximum available power of the WT. Also, the possibility of providing both IR and PFR using external energy storage systems (ESS), in this work supercapacitors and battery energy storage system (BESS), has been considered. For each support scheme analysed for the VSWTs, this work provides a comprehensive survey.

This dissertation further proposes two coordinated control strategies that exploits the full potential of VSWTs to participate in power system frequency response enhancement and small-signal stability support.

For frequency response improvement, large wind power IR and PFR support on the frequency response of two different networks representing grids with either fast or slow dynamics, have been investigated. A control strategy that seeks to provide a coordinated IR and PFR support to the system through simultaneous utilization of dc-link capacitor EE, WT rotor KE and reserved

a portion of the WT available energy is then proposed. The performance of the support schemes is compared to the case in which a large-scale centralized BESS unit is employed to provide frequency support services.

On the other hand, concerning small-signal stability improvement, this work investigates large wind power IR support on the small-signal stability of the Sicilian network for different dispatching profiles (DPs) for the years 2030 and 2050. A control strategy that seeks to provide a coordinated IR support to the system through simultaneous utilization of EE of supercapacitor units installed on the dc-link of the WPPs and WTs rotor KE is proposed for the 2030 network. Since the installation of BESS are predicted for the 2050 network, a strategy that seeks to provide a coordinated IR support to the system through simultaneous utilization of EE of the supercapacitor units, the WTs rotor KE and the stored energy from the BESS units is proposed. Dynamic simulation and modal analysis results presented indicate that the coordinated IR control scheme provides the best improvement in the both frequency response and small-signal stability as compared to when employing the individual frequency support schemes.

All the control schemes are developed and simulation studies performed on DIgSILENT PowerFactory simulation environment.

Contents

List of Figures

List of Tables

Acronyms

AGC	Automatic Generation Control
BESS	Battery Energy Storage System
CCM	Current-Controlled Mode
DFIG	Doubly-Fed Induction Generator
DP	Dispatching Profile
EE	Electrostatic Energy
EM	Electro-Mechanical
ESS	Energy Storage Systems
FCWT	Full Converter Wind Turbine
GSC	Grid-Side Converter
HE	High Export
HI	High Import
HL	High Load
IR	Inertial Response
KE	Kinetic Energy
LL	Low Load
LooS	Lines out of Service
MC	Monte Carlo
MPPT	Maximum Power Point Tracking
PFR	Primary Frequency Response
PI	Proportional-Integral
PLL	Phase-Locked Loop
PWM	Pulse Width Modulation
RES	Renewable Energy Sources
RKC	Rotor Kinetic Energy Control
RoCoF	Rate of Change of Frequency
RSC	Rotor-Side Converter
SG	Synchronous Generator
SoC	State of Charge
SVPWM	Space Vector Pulse Width Modulation
VCM	Voltage-Controlled Mode
VSWT	Variable Speed Wind Turbine
WF	Wind Farm
WPP	Wind Power Plant
WT	Wind Turbine

Chapter 1. Introduction

This PhD thesis presents the development and analysis of frequency support schemes required for the integration of large amount of WPPs in the power system. The developed schemes aim at improving both the frequency response and small-signal stability of the low-inertia future network with high wind power penetration.

1.1 Power System Stability Challenges

Power system stability has been defined in [1] as: “the ability of an electric power system, for a given initial operating condition, to regain a state of operating equilibrium after being subjected to a physical disturbance, with most system variables bounded so that practically the entire system remains intact.” Power system stability can be classified into three classic categories consisting of angle stability, frequency stability and voltage stability [1]. Next to these classic categories, two new stability classes in line with the newly extended stability definition and classification published by the IEEE in 2021 [2], namely resonance stability and converter-driven stability are introduced as shown in Figure 1. These new additions are necessary to cover the effects of the increasing penetration of fast-acting converter-based resources, loads and transmission devices in modern power systems.

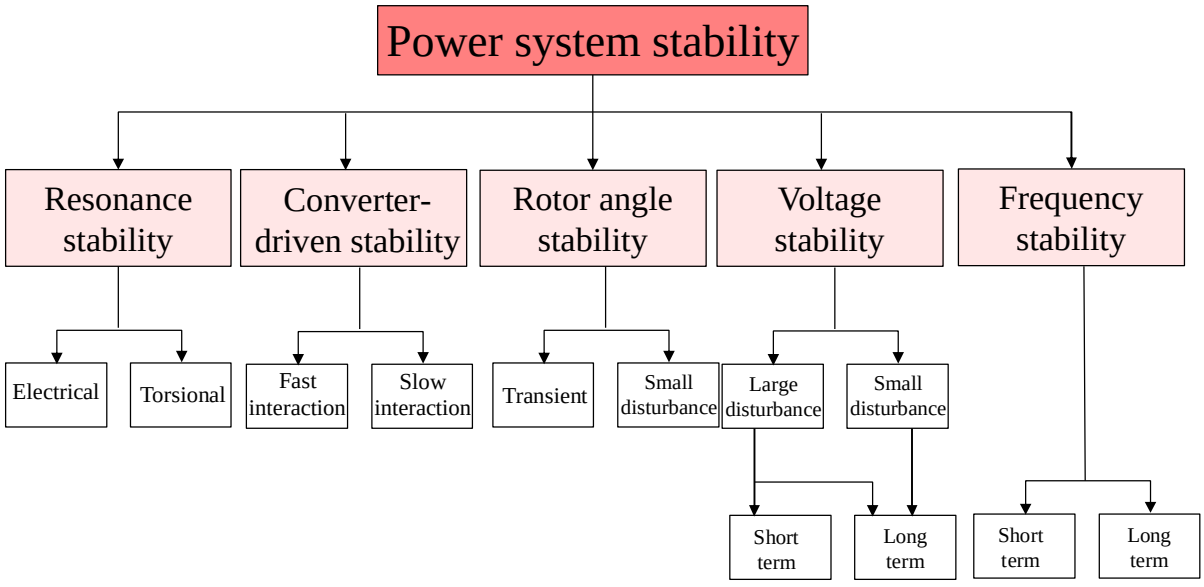

Figure 1. Stability classification of modern power systems with high-penetration power electronics [2].

A brief description of the different categories of system stability are presented below.

Rotor angle stability: This type of stability can be classified into:

(i) Large-disturbance rotor angle stability or transient stability which refers to the ability of synchronous machines in an interconnected power system to remain in synchronism after being subjected a large disturbance which does not allow a generator to deliver its output power into the network such as a short circuit on a transmission line. Aperiodic or non-oscillatory transient instability happens because of insufficient or negative synchronizing torque.

(ii) Small-signal rotor angle stability which refers to the ability of synchronous machines in an interconnected power system to remain in synchronism after being subjected to a small disturbance, small enough that the assumption of system dynamics being linear remains valid for analysis purposes. Small-signal oscillatory instability happens because of the lack of damping torque and it is characterized by a pair of complex conjugate poorly damped eigenvalues of the linearized system state matrix.

Frequency stability: Refers to the ability of a power system to maintain system frequency within the specified operating limits following a severe system upset which results in a significant imbalance between generation and load. Frequency instability that may result occurs in the form of sustained frequency swings leading to tripping of generating units and/or loads.

Voltage stability: Refers to the ability of a power system to maintain steady acceptance voltages at all system's buses after being subjected to a disturbance from an assumed initial equilibrium point. A voltage collapse typically occurs when not enough reactive power is being produced to energise the power system components and is often a slow process. Voltage instability may result because of the loss of load in an area or tripping of transmission lines and other elements by their protective systems, leading to cascading outages.

Resonance stability: Resonance occurs when energy exchange takes place periodically in an oscillatory manner which is manifested in the voltage/current/torque signals. Instability occurs when the amplitudes of the voltage/current/torque increase above a certain threshold and it is caused by insufficient dissipation of energy in the flow path. This type of stability can be classified into:

(i) Electrical resonance which refers to the electromagnetic oscillation caused by the dynamic interaction between the power electronic-based devices and the power grid in the purely electrical sense.

(ii) Torsional vibration which mainly refers to the oscillatory instability caused by the interaction between the mechanical system of the rotating unit and the ac electrical network with the series compensation and other converter-based equipment, such as static var compensator.

Converter-driven stability: The multi-time scale control characteristics of the converter interfaced generations lead to the coupling interaction of electromechanical dynamics and electromagnetic transients between the control systems of power electronic-based devices and the network, resulting in the oscillation in a wide frequency range. Based on the frequency, the converter-driven stability can be classified into:

(i) Fast-interaction converter-driven stability which involve system-wide instability problems driven by fast dynamic interactions of the control systems of power electronic-based devices with fast-response components of the power system such as the transmission network, the stator dynamics of synchronous generators or other power electronic-based devices with high frequency, typically from tens to hundreds of Hz, even up to kHz.

(ii) Slow-interaction converter-driven stability which involve system-wide instability problems driven by slow dynamic interactions of the control systems of power electronic-based devices with slow-response components of the power system such as the electromechanical dynamics of synchronous generators with lower frequency, typically less than 10 Hz.

1.2 Wind Power

1.2.1 Market status and forecast overview

In the last decade, the share of renewable energy sources (RESs) has been steadily increasing worldwide, both in new installed capacity and power consumption. In the year 2020, more than 80% percent (representing 260 GW) of new installed capacity was composed by RES, with 91% of which were wind and solar; this trend is poised to grow in the coming years [3]. The International Renewable Energy Agency reports that wind power almost doubled in the year 2020 compared to 2019 (111 GW in 2020 compared to 58 GW in 2019) [3]. The Global Wind

Energy Council report of 2021 also reports that wind power reached a total installed capacity of 743 GW worldwide at the end of 2020 with an increase of 98 GW (representing 53 %) compared to 2019. Of this, the share of onshore wind capacity increased by 86.9 GW (representing 59 %) whereas the share of offshore wind capacity increased by 86.9 GW (representing 59 %) compared to 2019 [4].

In terms of forecast, the Global Wind Energy Council report in 2020 predicts 469 GW wind capacity to be added over the next 5 years (from 2021), equivalent to 94 GW yearly installations until 2025 [4]. Also, according to the International Energy Agency report 2020, wind power addition forecast includes: 68 GW in the main case and 80.8 GW in the accelerated case for 2021, 60.8 GW in the main case and 75.8 GW in the accelerated case for 2022, 65 GW in the main case and 100 GW in the accelerated case for annually from 2022 to 2025 [5]. Although these two reports present slightly different values of wind power increase in the past year (2020) and in the future, the values presented show that renewable energy's share (particularly, wind energy) in electrical power generation is experiencing a remarkable growth.

1.2.2 Integration challenges

Integration of large wind farms (WFs) into power systems introduces several technical and economic challenges to the reliable operation of power system [6], [7]. Technical challenges, such as angle and voltage control, frequency control, power quality issues, etc. usually arise primarily from the intermittent and unpredictable nature of wind and also the power electronic converters that interfaces most of these WTs, particularly VSWTs, to the power grid. Although these power converters provide numerous benefits because of the scientific and technological advancement [8], they also introduce additional dynamic stability issues [9], not only for the inherent loss of mechanical inertia, but also because VSWTs are usually operated in the MPPT mode with no frequency support capability [10]. Indeed, if no countermeasure is taken, this could undermine the overall stability of the grid. Several papers (e.g. [11]–[17]) have analysed the detrimental effects of the large penetration of wind power on the power system stability.

In [11], the impact of wind power location and penetration levels on voltage stability has been investigated. For the locations, the study observed that installing the wind power plants at several points has a better influence on the network voltage stability as compared to installing them at a centralised location. For the penetration levels, the study observed that as the voltage stability is improved at lower wind power penetration levels. However, in [12], the authors

observed that high penetration levels of wind power improve the system long-term voltage stability since the reactive power capability of WTs increases with increasing penetration level.

In [13], the impact of wind power location and penetration levels on transient stability has been investigated. Results presented indicate that increasing wind power penetration deteriorates the power system transient stability. Also, the locations of the WF and wind speed may affect the power system transient stability. Ref. [14] has studied the transient stability performance based on WF penetration levels and wind generator technology. Considering WTs equipped with fixed-speed induction generator, the power system provides a comparatively high stability at integration at the high-voltage level over low-voltage level due to strong voltage support in the high-voltage network. On the other hand, the transient stability is improved with installation of doubly-fed induction generator (DFIG) based WFs. However, these observations are considered at low wind penetration levels; for high penetration levels (50%), the transient stability experiences a significant degradation due to the high reactive power absorption of wind generators under transient disturbances.

On small-signal stability, [15] has investigated the effects of wind power penetration level and fast frequency response support from WPPs using a two-area four generator system. It was observed that insufficient damping in the inter-area mode is detrimentally affected by the large penetration of DFIG units without any form of fast frequency response support. However, fast frequency response support schemes implemented on DFIG units with sufficient energy stored at the dc-link can play a significant role in improving the small-signal stability of the system. In [16], the authors used the 14-generator South-East Australian equivalent system to study the of high wind power penetration levels on power system small-signal stability. Similarly, it was observed that the damping of inter-area modes was severely affected by high wind power penetration.

Finally concerning the issue of frequency response enhancement, authors in [17] have indicated that high wind power penetration levels resulted in less system IR which leads to high network frequency deviations during disturbances. IR control schemes have therefore been proposed to enable WPPs to support network frequency response. Similarly, various forms of frequency response support schemes have been suggested in [10], [18]–[33].

1.3 Objectives and Contributions of the Work

To maintain the stability of power systems, modern RESs are thus required to provide ancillary services, such as angle, voltage and frequency control in addition to energy production [34], [35]. Hence, the aim of this PhD thesis is to develop control algorithm that enables VSWT power plants to contribute to power system stability improvement, with focus on frequency response and small-signal stability. The main contributions of this PhD thesis are summarised as follows:

- Performance of a sensitivity analysis of IR and PFR parameters on the network frequency response.
- Development of control algorithm for WT IR and PFR support.
- Proposal of a coordinated frequency controller aiming at exploiting the IR and PFR capability of WTs to improve power system frequency response.
- Proposal of a coordinated frequency controller aiming at exploiting the IR capability of WTs to improve power system small-signal stability.

1.4 Outline

This PhD thesis is presented in seven chapters, structured as follows.

Chapter 1: Presents a brief overview of power system stability, current wind power market status, future direction, and integration challenges. The objectives and outline of this work are also presented.

Chapter 2: A brief background on power system frequency control is presented. Also, a parameter sensitivity analysis of an energy storage device participating in both IR and PFR on the network frequency response is presented.

Chapter 3: The adopted WT model, the frequency support schemes and the relevant controllers are developed.

Chapter 4: A validation of the IR provision by two dc-link IR architectures usually adopted in literature is presented. Also, the possibility of forming a coordination between the architectures and other frequency support schemes implemented on the WT is highlighted.

Chapter 5: Studies the coordination between the developed IR and PFR support schemes and their impact on the power system frequency response. Two different types of grids representing networks with fast dynamics and slow dynamics are adopted for the simulation studies.

Chapter 6: Studies the coordination between the developed IR support schemes and their impact on the power system small-signal stability. The network adopted in this section is the portion of the Italian transmission grid corresponding to Sicily for the years 2030 and 2050.

Chapter 7: A summary and conclusion of the work done is presented in this section.

Chapter 2. Power System Frequency Control

Conventionally, the principal behaviour of system frequency to a large disturbance is divided separate control regimes in terms of different time scales: IR, PFR, secondary frequency response also known as the automatic generation control (AGC) and tertiary frequency response as indicated in Figure 2 [10]. Immediately after a disturbance in a power system, the inertia of the synchronous machines in the system limits the frequency deviation even before the electrical governors react to restore the frequency and this action is usually termed as IR. The action of the PFR follows the IR and aims at stabilizing the frequency to a new steady state and arresting the frequency deviation. In units with SGs, governors are responsible for this response and the control consists in providing an output power proportional to frequency deviation. In this manner, slower governor response of SG units leads to network frequency attaining lower nadir. The AGC takes place within minutes and its responsible for restoring the network frequency to its nominal value. After completion of the AGC, the tertiary frequency control acts to restore the power reserve of the generators used for the AGC to handle present or future disturbances.

In this chapter, a mathematical formulation of synchronous inertia background is first presented from which the concept of how employing fast reserves with PFR and/or IR based control can help improve power system frequency response is derived. These mathematical formulations are supported by means of parameter sensitivity analysis performed on a storage unit participating in both PFR and IR.

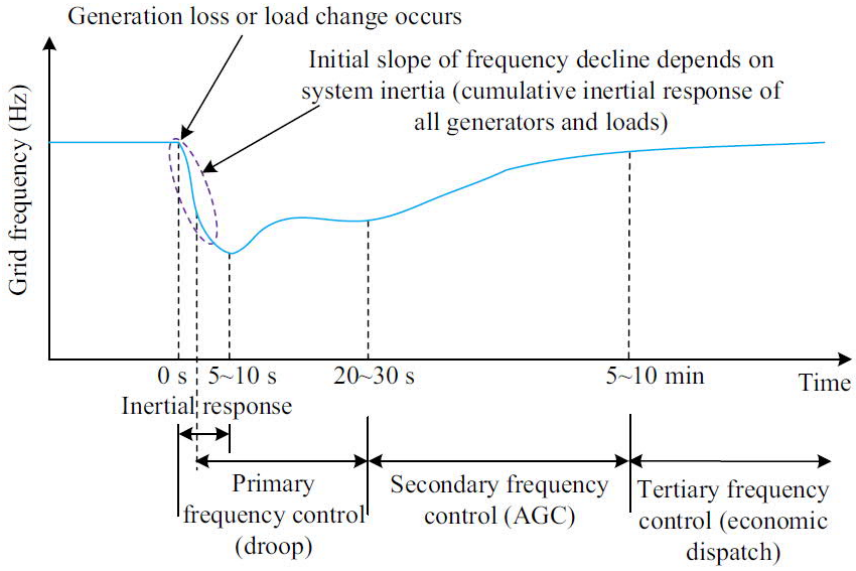

Figure 2. Schematic diagram of comprehensive frequency control [10].

2.1 Synchronous Inertia: Mathematical Background

The initial motion (neglecting any controller action) of a SG immediately following a power mismatch (i.e., between machine output and demand) in terms of frequency f can be expressed in per unit form as [39]:

$$\Delta p_{SG} = p_m - p_e = 2Hf\frac{df}{dt} \tag{0.1}$$

Assuming $f \approx 1$, (0.1) can be approximated as:

$$p_m - p_e = 2H\frac{df}{dt} \tag{0.2}$$

where p_m is the mechanical power, p_e is the electrical power, H is the synchronous generator inertia constant, f is the network frequency. Assuming that p_m is constant immediately after a disturbance in a power system, then it can be considered that frequency regulation will be from the rotation inertia of SGs in the system, frequency dependent loads, devices participating in both PFR and IR with output Δp given as in (0.3). p_e can therefore be expressed as in (0.4):

$$\Delta p = K_D\Delta f + K_I\frac{df}{dt} \tag{0.3}$$

$$p_e = p_{e0} + (D + K_D)\Delta f + K_I\frac{df}{dt} + \Delta p_e \tag{0.4}$$

where p_{e0} represents the base electric power in steady state, D represents the damping factor which considers the electrical loads that change their active power consumption with changes in network frequency, $K_D = K_D(t-t_0)$ is the proportional gain of devices participating in PFR, $K_I = K_I(t-t_0)$ is the proportional gain of devices participating in IR, $\Delta f = f - f_0$ represents the frequency change from the rated frequency f_0 and Δp_e is the perturbation. Both K_D and K_I are time variant terms representing the time taken to activate the devices, t represents the time and t_0 represent the delay due to energy source response time, delays introduced by filters, communication delays and power ramp rate limitations. Substituting (0.4) into (0.2), one obtains:

$$p_m - p_{e0} = \left(2H + K_I\right)\frac{df}{dt} + (D + K_D)\Delta f + \Delta p_e \tag{0.5}$$

In steady state, p_m is equal to p_{e0} and by solving the differential equation, Δf and df/dt can be expressed as in (0.6) and (0.7) respectively:

$$\Delta f(t) = \left(\frac{e^{-\frac{(D+K_D)}{(2H+K_I)}t}}{D + K_D} - \frac{1}{D + K_D} \right) \Delta p_e \tag{0.6}$$

$$\frac{df(t)}{dt} = -\frac{e^{-\frac{(D+K_D)}{(2H+K_I)}t}}{2H + K_I} \Delta p_e \tag{0.7}$$

From (0.6) and (0.7) , it is observed that employing fast reserves with PFR and/or IR based control mitigates the impacts of both frequency deviation and rate of change of frequency (RoCoF) during power imbalances. It is relevant to determine the energy and power ratings of ESS to provide the IR and PFR services at a given WT or WF level. The amount of power P_{ESS}^{IR} and energy E_{ESS}^{IR} required by a storage unit to provide IR during frequency event can be deduced from (0.2) as:

$$P_{ESS}^{IR} = 2H_{syn} S_{ESS} \left.\frac{df}{dt}\right|_{\max} \tag{0.8}$$

$$E_{ESS}^{IR} = 2H_{syn} S_{ESS} \Delta f_{\max} \tag{0.9}$$

where S_{ESS} is the rated power of the storage unit (in MW), H_{syn} is the equivalent inertia to be emulated, df/dt_{max} is the maximum RoCoF permitted, Δf_{max} is the maximum frequency deviation permitted. On the other hand, the amount of power required by a unit to provide PFR depends on the amount of time that the storage device is required to offer the service.

2.2 Parameter Sensitivity Analysis of a Storage Unit Providing PFR and IR Services

In this section, the influence of the parameters of a storage unit (in this case BESS) providing both PFR and IR services according to (0.3) on the frequency response of the power system has been analysed. A detailed description of the BESS control scheme is presented in Section 3.2.4A. The parameters considered are: (a) PFR and IR gains, (b) active power reserve, (c) response time and (d) frequency controller deadband. Figure 3 shows the single line diagram of the network to which the 1 MVA BESS unit, a 4.855 MVA diesel generator (DG) with inertia constant indicated as H_{DG}, and constant active and reactive power load models connected. The frequency event is initiated by the introduction of an active load step. The frequency nadir (F_{min}) and maximum rate of change of frequency ($RoCoF_{max}$) are used as the frequency response performance indicators. Four case studies with different frequency support gain combinations (K_D, K_I) (i.e., Case A is (20,0); Case B is (0,20); Case C is (10,10) and Case D is (0,0)) are considered. These values are adopted for demonstration purpose and are not selected using any special techniques.

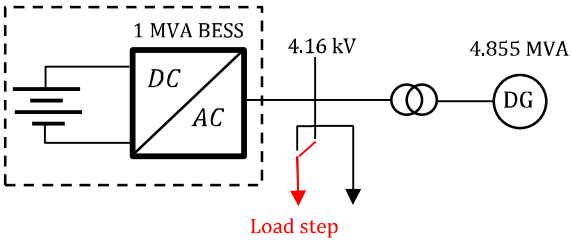

Figure 3. Considered network for the PFR and IR parameter sensitivity analysis.

2.2.1 Effect of PFR and IR gains

A sensitivity analysis is carried out to determine how PFR and IR affect F_{min} and $RoCoF_{max}$ on grids with different inertia values, i.e., H_{DG} ranging from 2s to 20s. The four presented case studies are employed in this analysis. Figure 4a shows F_{min} for the four study cases presented with increasing H_{DG}. At very low H_{DG} (i.e., 2s), case B provides the best improvement in F_{min} followed by cases C and A. Case D has the minimum F_{min}. However, as H_{DG} increases above 2s, case A overtakes case B to provide the minimum F_{min} values. For case C, the value of F_{min} always lies between those of case A and B for all H_{DG} values. It can also be realized that improvement by frequency support scheme of the BESS is better for small H_{DG} values. The observation drawn here is that as the dynamics of the grid gets very fast at very low inertia, IR

provision has a better influence on the frequency nadir of the network as compared to PFR. Figure 4b shows $RoCoF_{max}$ for the four study cases presented. As observed, case B provides the lowest values of $RoCoF_{max}$ for all H_{DG} values. Case D provides the highest $RoCoF_{max}$ values. The observation drawn is that, for all grid dynamics, IR provision always has a better influence on the RoCoF of the network as compared to PFR.

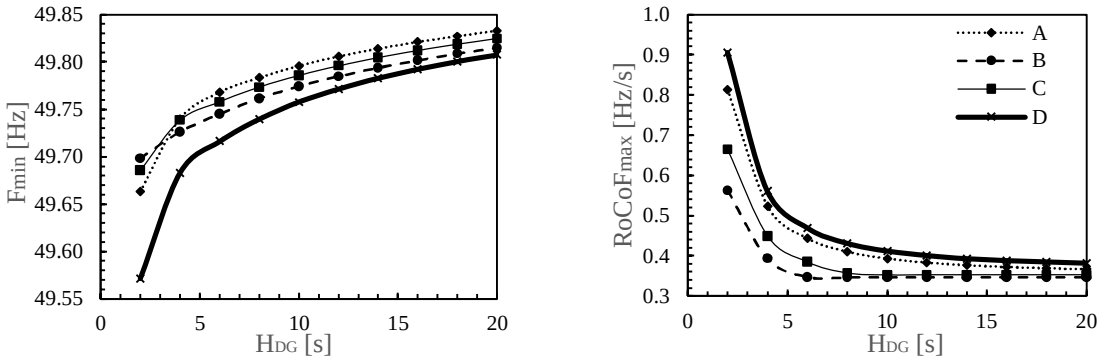

(a) (b)

Figure 4. Influence of parameters K_D and K_I on: (a) frequency nadir and (b) maximum RoCoF for different values of grid inertia.

2.2.2 Effect of active power reserve

In this study, the output active power of the BESS is limited to +/-0.01 p.u. Figure 5a and Figure 5b show F_{min} and $RoCoF_{max}$ for the four study cases presented with increasing H_{DG}. Results indicate only minor improvement in both F_{min} and $RoCoF_{max}$ values for all the four case studies presented. The observation drawn is that unlimited power reserve is required to provide improvement in both frequency nadir and the RoCoF values of the network. High power density devices like supercapacitors and flywheels are more suitable for providing this kind of service.

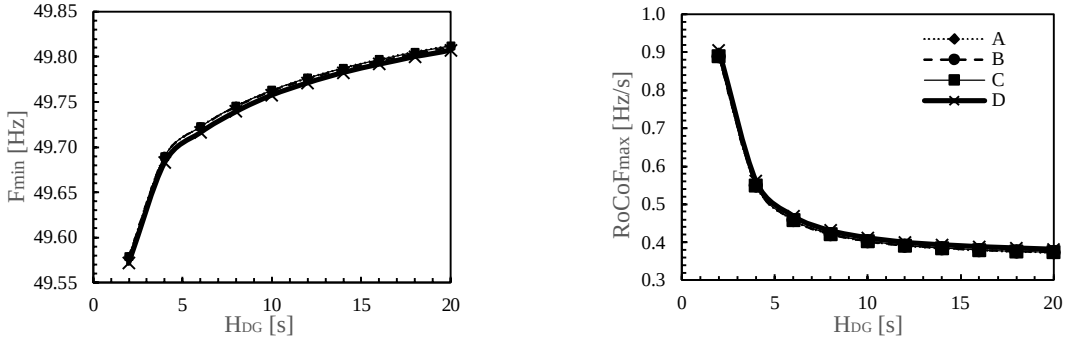

(a) (b)

Figure 5. Influence of parameters K_D and K_I on (a) frequency nadir and (b) maximum RoCoF for different values of grid inertia. Active power reserve is limited to 0.01 p.u.

2.2.3 Effect of response time

Different response times (T_{BESS}) ranging from 0s to 3s representative of different BESS technologies are employed and their effect on both F_{min} and $RoCoF_{max}$ on grids with different inertia values, i.e., H_{DG} of 2s, 4s, 8s and 16s are presented. The base setting for the BESS response time in all the other studies performed in this paper is 0.01s. The analysis is performed for case studies A and B to understand the individual influence of PFR and IR response times on the frequency response of different grids (in terms of inertia value). Figure 6a and Figure 6b show F_{min} versus T_{BESS} values for case studies A and B respectively. For case A, larger T_{BESS} leads to lower F_{min} particularly for small values of H_{DG}. For large H_{DG} values, F_{min} versus T_{BESS} curves flatten. For case B, the observation is somehow different. For small H_{DG} values, increasing T_{BESS} leads to an initial increase in F_{min} and a decrease afterward. For H_{DG} values of 4s and 8s, increasing T_{BESS} leads to increase in F_{min}. The curve flattens for large H_{DG} values. Figure 6c and d show $RoCoF_{max}$ versus T_{BESS} values for case studies A and B respectively. For case A, larger T_{BESS} leads to larger $RoCoF_{max}$ values particularly for small values of H_{DG}. For large H_{DG} values, $RoCoF_{max}$ versus T_{BESS} curves flatten. For case B, similar observations can be drawn.

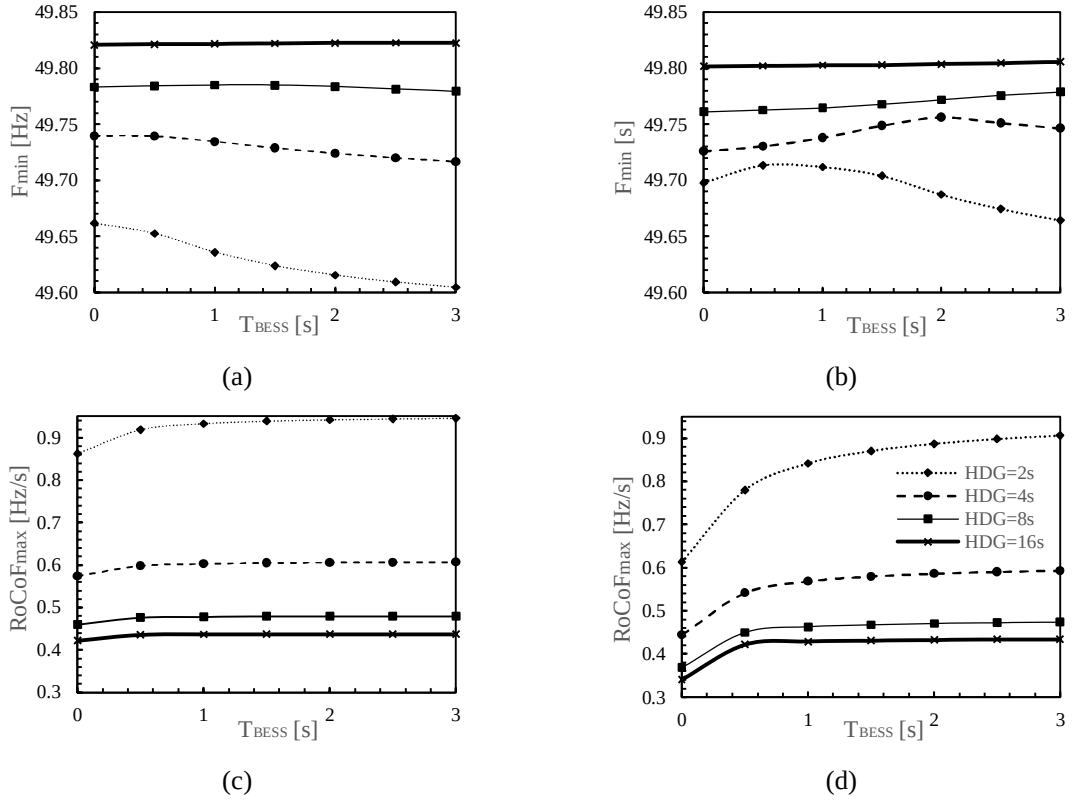

Figure 6. Influence of response time (a) for case study A and (b) for case study B on frequency nadir for different values of grid inertia; influence of frequency controller (c) for case study A and (d) for case study B on maximum RoCoF for different values of grid inertia.

2.2.4 Effect of frequency controller deadband

In this study, different values of frequency controller deadband ranging from 0% to 0.2% will be employed and their effect on both F_{min} and $RoCoF_{max}$ on grids with different inertia values, i.e, H_{DG} of 2s, 4s, 8s and 16s are presented. The base setting for both PFR and IR deadbands in all the other studies performed in this paper are 0%. The analysis is performed for case studies A and B to understand the individual influence of PFR and IR deadbands on the frequency response of different grids (in terms of inertia value). Figure 7a and Figure 7b show F_{min} versus deadband values for case studies A and B respectively. For both cases A and B, larger deadband values leads to lower F_{min}. Particularly the slope is steeper for small values of H_{DG}. Also, the slope is steeper for case A as compared to case B for all values of H_{DG}. This shows that deadband has a higher influence on the frequency nadir when employed in the PFR schemes as compared to it been employed in the IR scheme. Figure 7c and Figure 7d show $RoCoF_{max}$ versus deadband values for case studies A and B respectively. For both cases A and B, larger deadband values lead to higher $RoCoF_{max}$. Similar observations made on the slope F_{min} values can be made on the RoCoFmax values.

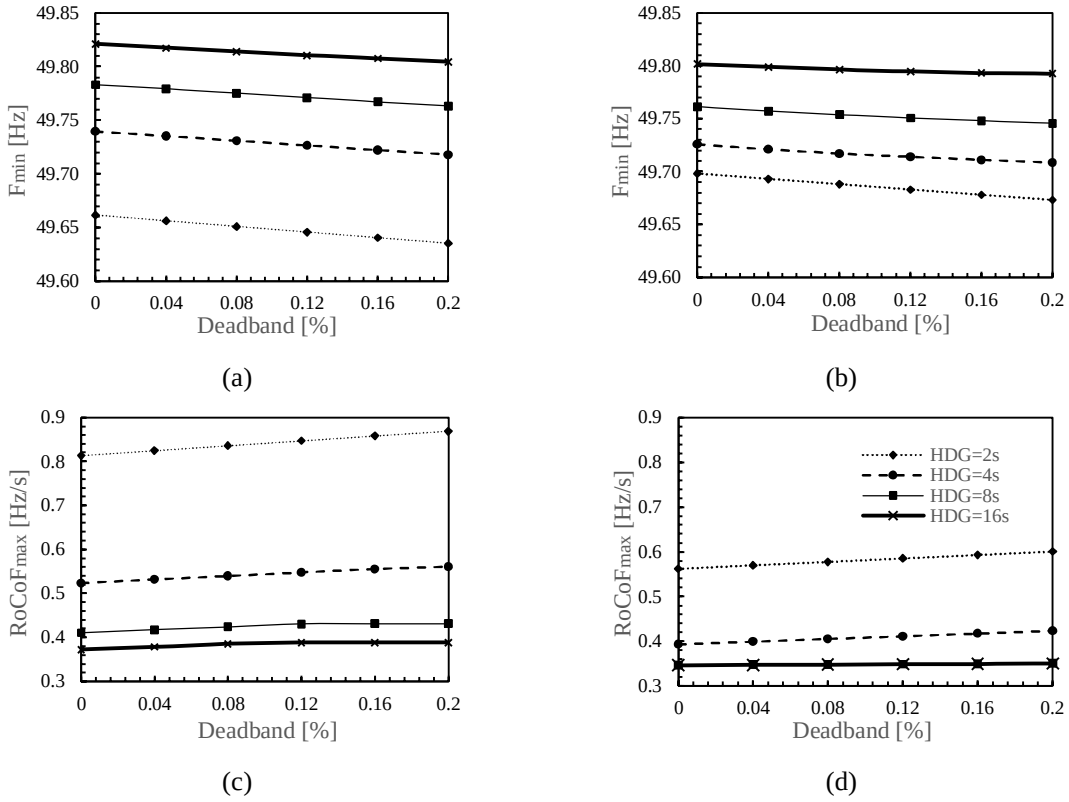

Figure 7. Influence of frequency controller (a) PFR (case study A) deadband and (b) IR (case study B) deadband on frequency nadir for different values of grid inertia; influence of frequency controller (c) PFR (case study A) deadband and (d) IR (case study B) deadband.

2.3 Summary

The chapter first gives a brief description of power system frequency control background and presents a sensitivity analysis study to determine the influence of the parameters (i.e., (a) PFR and IR gains, (b) active power reserve, (c) response time and (d) frequency controller deadband) of a BESS unit providing both PFR and IR on the frequency response of the power system. Simulation results presented show that:

- PFR provides better support of the frequency nadir as compared to IR. However, for grid with very fast dynamics because of low inertia and fast acting governors, IR provides better support of the frequency nadir as compared to PFR. In terms of RoCoF, IR always provides better support as compared to PFR.
- Both PFR and IR require unlimited power reserve to significantly improve both the frequency nadir and RoCoF.
- Increasing response time of the BESS unit deteriorates the support on both frequency nadir and RoCoF particularly, when PFR is employed.
- Deadband deteriorates the frequency response of the network and it is more significant in the PFR scheme compared to in the IR scheme.

Both mathematical formulations performed and simulation studies indicate that PFR and/or IR provision by energy storage units significantly improve power system frequency response.

Chapter 3. Wind Power Plants Frequency Support Schemes

The focus of this chapter is twofold. First, a detailed description of a VSWT equipped with a DFIG is presented and next control algorithms with possible energy buffers that enable VSWT power plants to mimic both the IR and PFR behaviour of traditional SGs are developed.

3.1 Modelling of Wind Turbines

In literature, a WT model usually consists of a: (a) mechanical level: WT aerodynamic model and pitch angle controller model; (b) electrical level: generator model and frequency converters (rotor-side converter (RSC) and grid-side converter (GSC)) and their controls. The type of WT only affects the generator model and its control approach when connected to the power network [36]. WFs are represented by a fully aggregated models of multiple WT units as described in [37]. This next section presents a detail description of a WT equipped with a DFIG.

3.1.1 Wind turbine model

A two-mass drive train model consisting of a large mass corresponding to the turbine rotor inertia J_W and a small mass corresponding to the generator inertia J_G is used to simulate the DFIG drive train. The shaft is modelled by a stiffness K_{sh} and a damping coefficient D_{sh}. The model equations are represented by:

$$\begin{aligned} T_W - T_{SH} &= J_T \dot{\omega}_t \\ T_{SH} - T_G &= J_G \dot{\omega}_r \\ \dot{\theta} &= \omega_t - \omega_r \\ T_{SH} &= K_{sh}\theta - D_{sh}\dot{\theta} \end{aligned} \tag{0.10}$$

where T_W is the wind torque, T_{SH} is the shaft torque, T_G is the electrical torque of the generator, θ is the angular difference between the two ends of the flexible shaft and ω_r is the generator rotor speed. With $\dot{\theta}$, the time derivative of θ is denoted. The wind power P_W and mechanical power of the generator P_M are related to T_W and T_{SH} as:

$$P_W = T_W \omega_t$$
$$P_M = T_{SH} \omega_r \quad (0.11)$$

The extracted wind power P_W is expressed as a function of the wind speed v_w and rotational speed of the turbine ω_t with an algebraic equation [38]:

$$P_W = 0.5 C_P(\lambda, \beta) \rho \pi R^2 v_w^3 \quad (0.12)$$

where, as known, ρ is air density, R is the radius of the rotor, $\lambda = \omega_t R / v_w$ is the tip speed ratio, β is the blade pitch angle, C_p is the power coefficient which describes the aerodynamic efficiency of the rotor, expressed as a function of λ and β.

The dynamic power balance equation during mismatch between P_W and the WT output P_{WT} is expressed as:

$$2H_S \omega_s \frac{d\omega_r}{dt} = p_W - p_{WT} \quad (0.13)$$

where $H_S = H_T + H_G$; H_S represents the total WT mechanical inertia constant, H_T represents the turbine inertia constant and H_G represents the generator inertia constant.

3.1.2 Pitch angle control

In Figure 8, the pitch angle control system model is shown. The control is implemented to prevent over-speeding of the WT rotor in both normal operations and during grid faults. The input to the controller is the difference between the measured generator speed and the maximum generator speed. Below maximum speed $\omega_r^{\max}$ of the generator, the output of the PI controller is zero. In case of over-speeding i.e., when the generator speed exceeds $\omega_r^{\max}$ due to excess wind power or during faults, the proportional-integral (PI) controller increases β^{ref} to decelerate the generator back towards $\omega_r^{\max}$. The first-order actuator models the physical process of bringing the pitch angle β to its reference value β^{ref}, with limitation both for the pitch angle β and its rate of change $\dot{\beta}$.

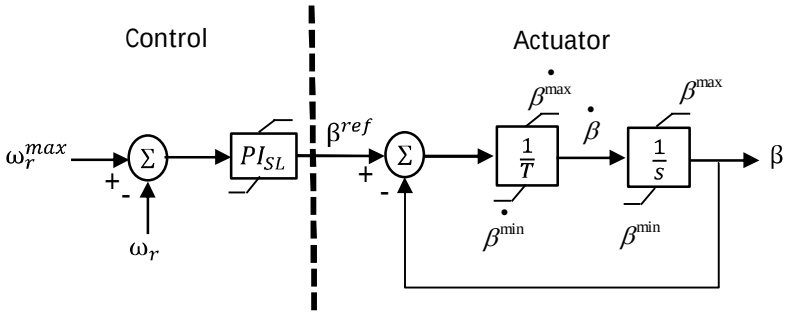

Figure 8. Pitch control system model.

3.1.3 DFIG model

The DFIG stator and rotor voltage vector equations in a synchronous reference frame ω_s are defined as:

$$-u_s = R_s i_s + \frac{d\psi_s}{dt} + j\omega_w \psi_s \tag{0.14}$$

$$-u_r = R_r i_r + \frac{d\psi_r}{dt} + js\omega_s \psi_r \tag{0.15}$$

where u_s and u_r are the space phasor of the stator and rotor voltages respectively; R_s and R_r are the stator and rotor resistances respectively; s is the slip; p is the number of pole pairs; ψ_s and ψ_r are the stator and rotor flux linkages given as (0.16) and (0.17) respectively:

$$\psi_s = L_s i_s + L_m i_r \tag{0.16}$$

$$\psi_r = L_m i_s + L_r i_r \tag{0.17}$$

Where L_s, L_r and L_m are the stator, rotor and mutual inductance respectively. The electromagnetic torque T_E can be expressed using the *d*-*q* components as:

$$T_E = \frac{3}{2} p \frac{L_m}{L_s} \left(i_s \psi_{sq} - i_{rq} \psi_{sd} \right) \tag{0.18}$$

3.1.4 Rotor-side converter control

The RSC control consists of the *d*-axis and the *q*-axis channels both adopting typical PI controllers as illustrated in Figure 9. The *d*-axis channel consisting of three PI control loops in cascade, controls mainly the generator active power p_{WT} and works as follows: as known, the objective of the MPPT curve is to drive the wind generator automatically to the operation point of highest efficiency at any given time. The rotor speed reference for maximum power extraction from the WT is generated by a predefined power-speed MPPT characteristics (in this

work we consider the case in which the reference speed generated by the MPPT controller is related to the WT output power by a quadratic relationship). The first PI controller acts on the difference between the measured rotor speed and the reference speed generated from an MPPT controller to determine the active power reference for the RSC. The second PI controller controls the WT output active power to the reference generated from the speed controller and generates the *d*-axis reference rotor current for the fast inner current PI control loop that controls the *d*-axis current component to define the *d*-axis modulation index for the converter. The *q*-axis channel consisting of two PI control loops in cascade, controls the generator stator reactive power and works as follows: The first PI controller controls the WT output reactive power to a specified reference and generates the *q*-axis reference rotor current for the fast inner current PI control loop that controls the *q*-axis current component to define the *q*-axis modulation index for the converter.

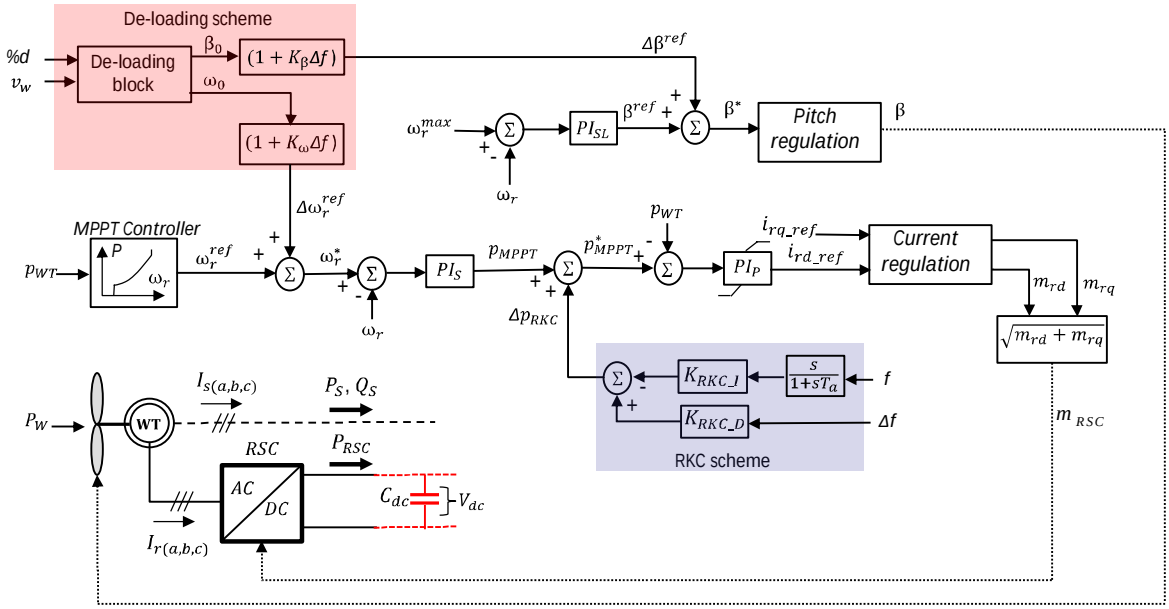

Figure 9. Schematic diagram of RSC control architecture for RKC IR and deloading scheme PFR. The model adopted consists of rotor speed control scheme.

3.1.5 Grid-side converter control

Like the RSC, the GSC control consists of the *d*-axis and the *q*-axis channels both adopting typical PI controllers as illustrated in Figure 10. The *d*-axis channel consisting of two PI control loops in cascade and works as follows: The first PI controllers regulates the dc-link voltage to a specified reference regardless of the magnitude and direction of the power from the RSC and generates the *d*-axis reference rotor current for the fast inner current PI control loop that controls the *d*-axis current component to define the *d*-axis modulation index for the converter. The *q*-

axis channel usually (as in this work) consists of only one PI control loop that regulates the *q*-axis reference rotor current to a reference of zero (unity power factor) to define the *q*-axis modulation index for the converter. In this way, the reactive power flow from the GSC is set to zero to reduce the GSC rating.

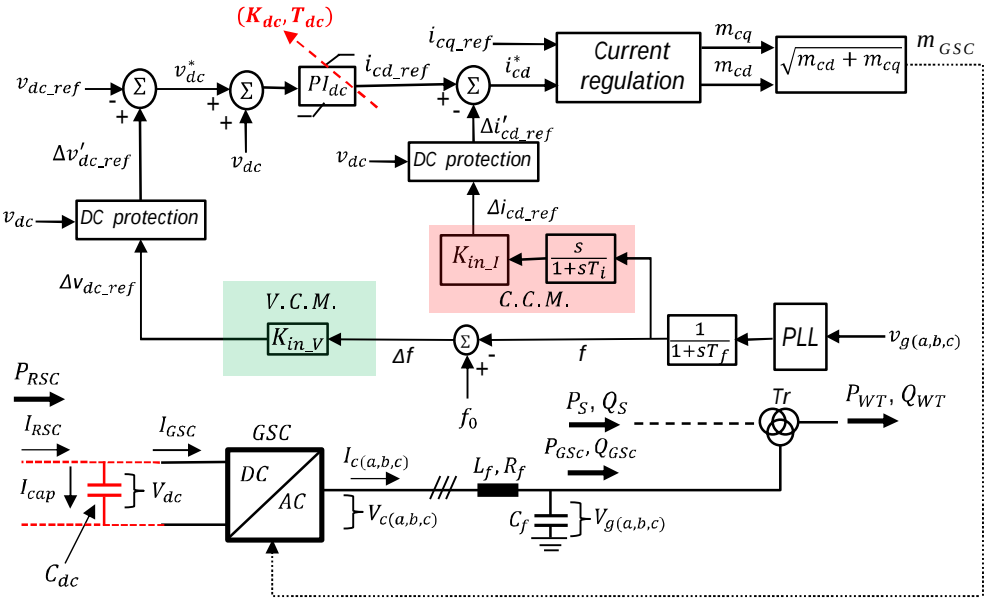

Figure 10. Schematic diagram of GSC control architectures for dc-link IR.

3.1.6 Power converter models

Since this work is focused on power system stability, switching frequencies and high frequencies phenomenon are neglected and the only response of the system at the utility frequency is considered. The converters are based on fundamental frequency model which operates in a stator voltage-oriented reference frame. For sinusoidal pulse width modulation (PWM) technique with modulation index $|m|<1$, the line-line rms ac-side voltage U_{ac} voltage and dc voltage U_{dc} are related by:

$$U_{ac} = \frac{1}{2}\sqrt{\frac{3}{2}} m U_{dc} \qquad (0.19)$$

where $m = \sqrt{m_d + m_q}$; m_d and m_q are the *d*-axis and *q*-axis components of the *m*. The PowerFactory PWM-converter model has m_d and m_q as inputs; m_d drives the active power output of the converter while the m_q controls the reactive power. For values of $|m|>1$, the converter starts to saturate with the appearance of low-order harmonics. Adopting the space vector pulse width modulation technique (SVPWM), the value of *m* can be increased to 1.15.

3.2 Frequency Support Schemes

VSWTs can mimic both the IR and PFR behaviour of traditional SGs with the appropriate control schemes and energy reserve. Since IR requires short term power provision, additional controllers need be installed on the converters of VSWTs to exploit the EE stored in the dc-link capacitors or the KE of their rotors by using the rotor kinetic energy control (RKC) method. To participate in PFR, VSWTs require sufficient power margin to deliver steady-state power exchange. This is usually achieved by (a) operating the generators at non-optimal operating conditions under a constant wind speed, a method known as deloading, or (b) employing external ESS, for example, a BESS.

For convenience, the support schemes and the relevant controllers are briefly illustrated in the next subsections. All control signals are measured in per units.

3.2.1 Inertial response emulation from dc-link capacitors

The dc-link capacitors are mainly employed in almost all grid-connected power converters for dc-link voltage support, filtering dc voltage ripples, reactive power compensation [40]–[43]. Their presence ensures power balance between the RSC and GSC and any unbalance in the power results in dc voltage change. Although limited in capacitance, the electrostatic energy stored in these capacitors can be accessed for IR via the GSC by varying the dc-link voltage V_{dc} in response to frequency changes.

A. Dc-link inertial response architectures

In literature, two major architectures to realize dc-link IR are proposed as illustrated in Figure 10 and are described as follows:

Current-controlled mode (CCM): This scheme considers a derivative relation between the injected power (active current reference) and the measured network frequency as illustrated in colour red in Figure 10 and has been presented in [44]–[47]. This control scheme takes the derivative of the network frequency as input and multiplying it by a constant gain K_{in_I}, outputs the variation of the direct current reference (generated by the dc-voltage controller) thus regulating the active power injected into the grid. An additional first-order low-pass filter with time constant T_i is employed to filter out the noise from the derivative signal and prevents sudden jumps. A negative sign is introduced to increase active power injection in case of an under-frequency event, exploiting the discharge of the dc capacitors and vice versa. To realise

IR this way, the dynamics of the dc-link voltage controller must be very slow to allow the stored electrostatic energy to be released/ absorbed before the voltage controller reacts to restore the dc voltage to its nominal value. The IR contribution of the dc-link capacitors adopting the CCM architecture can thus be derived as:

$$\Delta p_{dc} = \frac{2H_{dc}}{\left(1+sT_f\right)\left(1+sT_i\right)}\frac{df}{dt} \tag{0.20}$$

where T_f and T_i are filtering time constants. Ignoring these time constants, (0.20) can be approximated as:

$$\Delta p_{dc} \simeq 2H_{dc}\frac{df}{dt} \tag{0.21}$$

The relationship between H_{dc} and K_{in_I} can be derived as follows:

$$H_{dc} = \frac{K_{in\_I}}{2} \tag{0.22}$$

The maximum allowed dc voltage variation in realistic application is determined with respect to insulation applications, PWM functionality etc. It can be realised that for very large frequency transients, even smaller IR gain values may not keep the dc voltage within acceptable limits, therefore a proper protection of the dc-link is desirable. A protection scheme is implemented to decouple the design of IR gain from the public power network characteristics and keep the dc-link voltage always within the acceptable range. A detailed overview of the CCM IR dc protection scheme is shown in Figure 11. The dc protection scheme takes the output of the IR scheme and measured dc voltage as the input and activates the IR only when the charging or discharging process is compatible with the dc voltage ratings. In this way, discharging process is inhibited whereas charging process is allowed when dc voltage is lower than the minimum allowed value $v_{dc}^{\min}$. On the other hand, charging process is inhibited whereas discharging process is allowed when dc voltage is higher than the maximum allowed value $v_{dc}^{\max}$. To guarantees the maximum exploitability of the available energy reserve while the fulfilling the technical/security constraints associated to the converters, the dc voltage limits, i.e., $v_{dc}^{\max}$ and $v_{dc}^{\min}$, required for the design of the dc protection scheme is presented in Section B .

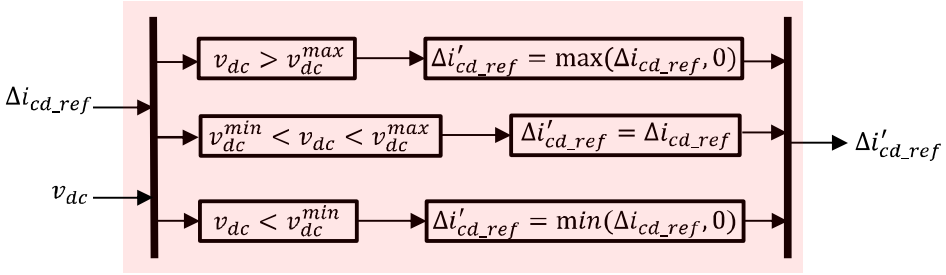

Figure 11. CCM IR with dc protection scheme.

Voltage-controlled mode (VCM): This scheme considers a proportional relation between the dc-link voltage reference and the measured network frequency deviation as illustrated in colour green in Figure 10 and has been presented in [20], [27], [34], [47]–[49]. A frequency controller with a constant gain K_{in_V} takes the frequency deviation signal as the input and the outputs the variation of the dc voltage reference. To make IR possible this way, the dynamics of the dc-link voltage controller is made very fast to allow the stored electrostatic energy to be released/ absorbed in response to the dc-link voltage deviation. The scheme links frequency and dc-link voltage in such a way that: (i) the change of network frequency will lead to a change of dc-link voltage and (ii) the derivative of the resulting change in dc-link voltage causes the absorption or release of power from dc-link capacitors. Although the input signal for the frequency controller is the frequency deviation signal, the dynamics of the voltage controller introduces a derivative and modifies the frequency response scheme to an IR control. However, since the dc-link voltage is linked to the frequency deviation signal by only a proportional term, a steady state drop in frequency causes a deviation in the dc-link voltage in steady state. Contrary to the CCM scheme, the VCM architecture does not use any frequency derivative measurement which undermines IR by angular oscillations in its output [50].

In the VCM IR architecture, the energy stored in the supercapacitors for IR can be accessed via the GSC by varying the dc-link voltage V_{dc}. Ignoring the power losses in the converters, the power balance of the power into the RSC P_{RSC} and the power transmitted to the grid via the GSC P_{GSC} is reflected by the dc-link voltage. The instantaneous power absorbed or released by the capacitor in per unit form is expressed as:

$$c_{dc} v_{dc} \frac{dv_{dc}}{dt} = p_{RSC} - p_{GSC} = \Delta p_{dc} \tag{0.23}$$

$$c_{dc} = \frac{C_{dc} V_{dc0}^2}{S_{WT}} \tag{0.24}$$

where S_{WT} is the WT rated power; C_{dc} and c_{dc} are the total capacitance in F and the equivalent capacitance in p.u., respectively; v_{dc} is the dc-link voltage in per unit form; V_{dc0} represent nominal dc voltage in V; p_{RSC} and p_{GSC} are the per unit form of P_{RSC} and P_{GSC} respectively and Δp_{dc} is the absolute power exchange from charging or discharging the capacitors. To assign the WT GSC with a IR constant H_{dc}, equating Δp_{SG} in (0.1) and Δp_{dc} in (0.23) gives:

$$2H_{dc} f \frac{df}{dt} = c_{dc} v_{dc} \frac{dv_{dc}}{dt} \tag{0.25}$$

where H_{dc} is the equivalent IR constant provided by the capacitors. Integrating both sides of (0.25), one obtains:

$$\int_{f_0}^{f} 2H_{dc} f df = \int_{v_{dc0}}^{v_{dc}} c_{dc} v_{dc} dv_{dc} \tag{0.26}$$

$$H_{dc}\left(f^2 - f_0^2\right) = \frac{c_{dc}\left(v_{dc}^2 - v_{dc0}^2\right)}{2} \tag{0.27}$$

where f_0 is the nominal network frequency. For small dc voltage variations, (0.27) can be linearized around its equilibrium point as:

$$2H_{dc} f_0 \Delta f = c_{dc} v_{dc0} \Delta v_{dc} \tag{0.28}$$

The reference dc-link voltage signal can be derived from (0.28) as follows:

$$v_{dc}^{*} = K_{in\_V} \Delta f + v_{dc0} \tag{0.29}$$

Combining (0.28) and (0.29), the relationship between H_{dc} and K_{in_V} can be derived as follows:

$$H_{dc} = K_{in\_V} \frac{c_{dc} v_{dc0}}{2 f_0} \tag{0.30}$$

The implementation of the VCM dc protection scheme, shown in Figure 12, although a bit different to the CCM IR dc protection scheme, they both have similar objectives of keeping the dc voltage within $v_{dc}^{\max}$ and $v_{dc}^{\min}$. The dc protection scheme takes the output of the IR scheme and measured dc voltage as the input and limits the IR outputs to values compatible with the dc voltage ratings. The IR output is limited to a value of $v_{dc0} - v_{dc}^{\min}$ during discharging process and only charging is allowed when dc voltage is lower than the minimum allowed value $v_{dc}^{\min}$. On the other hand, the IR output is limited to a value of $v_{dc}^{\max} - v_{dc0}$ during charging process and only discharging is allowed when dc voltage is higher than the maximum allowed value $v_{dc}^{\max}$.

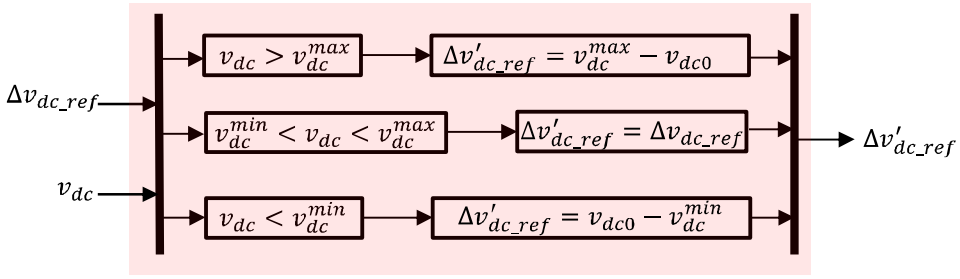

Figure 12. VCM IR with dc protection scheme.

To realise the two dc-link IR architectures, an import factor to consider are the parameters of the dc voltage controller as already mentioned. The parameters of the dc voltage PI controller are set to realise a slow dc voltage response for the CCM IR architecture whereas for the VCM IR architecture, the dc voltage PI controller parameters are set to realise a fast dc voltage response. The adopted parameters in this work are indicated as in Table 1.

Table 1. Dc-link voltage control parameters.

Parameter	CCM	VCM
K_{dc} [s^{-1}]	0.1	5
T_{dc} [s]	30	0.02

B. Dc-link voltage limits

For dc-link scheme IR implementation whereby the power released during a frequency disturbance is linked to the magnitude of the dc voltage variation, the GSC operation limits the maximum dc voltage deviation range. For over-frequency events, the dc-link capacitors are regulated to absorb energy by increasing the dc-link voltage. The maximum allowable voltage $V_{dc}^{\max}$, is determined by the voltage ratings of active and passive components of the GSC unit. On the other hand, for under-frequency events, the dc-link capacitors are regulated to release stored electrostatic energy by decreasing the dc-link voltage. However, the minimum allowable dc-link voltage $V_{dc}^{\min}$, is limited by pulse width modulation constraints.

In this section, a detailed mathematical analysis regarding the estimation of $V_{dc}^{\min}$ in both steady state and transient conditions and the factors that affect $V_{dc}^{\min}$ are presented. The estimation of $V_{dc}^{\min}$ and the fixed $V_{dc}^{\max}$ are required in the design of the dc-link protection schemes for IR implementations. The analysis is presented here on the GSC of a DFIG unit shown in Figure 10 but can also be applied to any grid connected converter unit. The GSC is connected to the grid by an inductive filter with inductance L_f and resistance R_f. To simplify the control, the *dq*

transformation method with a reference frame oriented along the stator (or supply) voltage vector position is adopted, enabling independent control of the active and reactive power flowing between the supply and the GSC. The voltage balance across the inductor expressed in the *dq*-frame is given by [51]:

$$\begin{cases} V_{sd} = R_f I_{cd} + L_f \dfrac{di_{cd}}{dt} - \omega_{dq} L_f I_{cq} + V_{cd} \\ V_{sq} = R_f I_{cq} + L_f \dfrac{di_{cq}}{dt} + \omega_{dq} L_f I_{cd} + V_{cq} \end{cases} \tag{0.31}$$

where ω_{dq} is the grid angular frequency. The quantities $V_{s(d,q)}$, $V_{c(d,q)}$ and $I_{c(d,q)}$ are respectively the voltage at the transformer low voltage side, the GSC ac-side terminal voltages and the GSC ac-side input currents expressed in the *dq*-frame. The complex power S_{GSC} drawn through the GSC can be written as [52]:

$$S_{GSC} = \frac{3}{2}\left[\left(V_{sd} I_{cd} + V_{sq} I_{cq}\right) + j\left(V_{sq} I_{cd} - V_{sd} I_{cq}\right)\right] \tag{0.32}$$

Aligning the *d*-axis of the reference frame along the voltage V_s, the voltage value of the *q*-axis V_{sq} will be zero, therefore, the active and reactive power can be expressed as:

$$\begin{cases} P_{GSC} = \dfrac{3}{2} V_{sm} I_{cd} \\ Q_{GSC} = -\dfrac{3}{2} V_{sm} I_{cq} \end{cases} \tag{0.33}$$

where V_{sm} represents the magnitude of the phase voltages V_s. As a result, the output active and reactive current of the GSC can be determined as:

$$\begin{cases} I_{cd} = \dfrac{2}{3} \dfrac{P_{GSC}}{V_{sm}} \\ I_{cq} = -\dfrac{2}{3} \dfrac{Q_{GSC}}{V_{sm}} \end{cases} \tag{0.34}$$

By neglecting the voltage drop across R_f, substituting (0.34) in (0.31) and rearranging, the converters output voltage can be expressed as:

$$\begin{cases} V_{cd} = \dfrac{2}{3} \dfrac{L_f}{V_{sm}} \left(-\dfrac{dP_{GSC}}{dt} - \omega_{dq} Q_{GSC} \right) + V_{sm} \\ V_{cq} = \dfrac{2}{3} \dfrac{L_f}{V_{sm}} \left(\dfrac{dQ_{GSC}}{dt} - \omega_{dq} P_{GSC} \right) \end{cases} \tag{0.35}$$

According to the adopted dc-link dynamic model, the GSC dc current I_{GSC} is given by:

$$I_{GSC} = I_{RSC} - I_{cap} \tag{0.36}$$

where I_{RSC} is the dc current flowing from the RSC and I_{cap} is the current absorbed by the dc-link capacitor. The dc-voltage must be controlled according to the following power balance,

$$P_{RSC} = V_{dc} I_{RSC} \tag{0.37}$$

At the utility frequency, the GSC is modelled by a dc-voltage controlled ac-voltage source conserving active power balance between ac and dc-side. For values of modulation index magnitude $m_{GSC} < 1.15$ using the SVPWM, the following expression can be applied [53]:

$$V_c = \frac{1}{2}\sqrt{\frac{3}{2}} m_{GSC} V_{dc} \tag{0.38}$$

where V_c is the line-to-line rms ac-voltage of the GSC. From (0.38), it can be observed the necessity of keeping adequate dc-link level to meet the inverter voltage, thus:

$$V_{dc} \geq 2\sqrt{\frac{2}{3}} \frac{V_c}{m_{GSC}} \tag{0.39}$$

Therefore, the minimum required dc-link voltage at maximum modulation index $m_{GSC}^{\max}$ can be computed as:

$$V_{dc}^{\min} = 2\sqrt{\frac{2}{3}} \frac{V_c}{m_{GSC}^{\max}} \tag{0.40}$$

Substituting (0.35) into (0.41), one gets (0.42).

$$V_c^2 = \frac{3}{2}(V_{cd}^2 + V_{cq}^2) \tag{0.41}$$

$$\begin{aligned} V_c^2 &= \frac{3}{2} V_{sm}^2 - 2L_f \left(\frac{dP_{GSC}}{dt} + \omega_{dq} Q_{GSC} \right) \\ &+ \frac{2}{3}\left(\frac{L_f}{V_{sm}} \right)^2 \left[\left(\frac{dP_{GSC}}{dt} + \omega_{dq} Q_{GSC} \right)^2 + \left(\frac{dQ_{GSC}}{dt} - \omega_{dq} P_{GSC} \right)^2 \right] \end{aligned} \tag{0.42}$$

The minimum required dc-link voltage, under the assumption of neglecting the third term in (0.42), can be expressed as (0.43).

$$V_{dc}^{\min} \simeq \frac{2}{m_{\max}} \sqrt{V_{sm}^2 - \frac{4}{3} L_f \left(\frac{dP_{GSC}}{dt} + \omega_{dq} Q_{GSC} \right)} \tag{0.43}$$

Under steady state operation $V_{dc}^{\min}$ is mainly affected by the transferred reactive power Q_{GSC}, while the active power P_{GSC} effect is negligible. Under dynamic conditions, $V_{dc}^{\min}$ is more sensitive to P_{GSC} changes rather than those of Q_{GSC}.

C. Capacitor energy capacity and sizing

The stored electrostatic energy E_{cap} in a capacitor is dependent on the voltage across the capacitor and can be expressed as:

$$E_{cap} = \frac{1}{2} C_{dc} V_{dc}^2 \tag{0.44}$$

For a capacitor of maximum energy rating given by $E_{cap}^{\max}$, the usable energy E_{cap}^{use} for underfrequency IR services is related to $E_{cap}^{\max}$ by:

$$E_{cap}^{use} = \underbrace{\frac{1}{2} C_{dc} (V_{dc0})^2}_{E_{cap}^{\max}} \left[1 - \left(1 - \frac{\Delta V_{dc}}{V_{dc0}} \right)^2 \right] \tag{0.45}$$

where $\Delta V_{dc} = V_{dc0} - V_{dc}^{\min}$. The usable energy is thus only a portion of the total stored energy and depends on the value of the voltage deviation. For a DFIG GSC operating at a common rated ac voltage of 0.69 kV and rated dc voltage of 1.15 kV, a graph of the ratio between the E_{cap}^{use} and $E_{cap}^{\max}$ versus the ratio of ΔV_{dc} and V_{dco} is shown in Figure 13. From the figure, two interesting observations can be made:

- At 50% of voltage variation, the capacitor module delivers 75% of its total stored energy.
- $V_{dc}^{\min}$ is estimated as 978 V using (0.40) and adopting the SVPWM technique. The ratio of voltage deviation and the maximum voltage is 0.15 (15%). The total energy of the supercapacitor available for the proposed IR application is only 28% of its total energy stored.

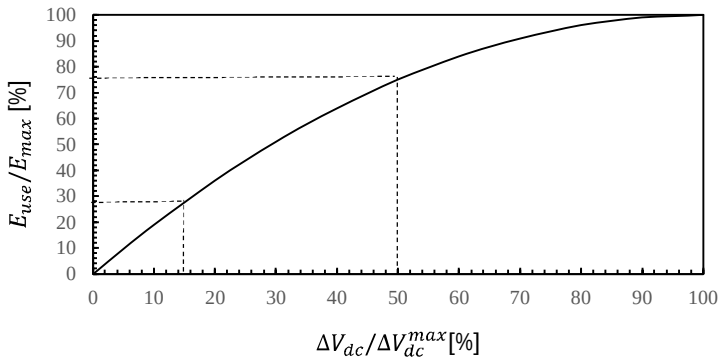

Figure 13. Ratio of the usable energy and the maximum stored energy versus the ratio of voltage deviation and the maximum voltage.

The sizing of the capacitors for the WTs dc-link IR provision can be derived as:

$$C_{dc} = \frac{x\%S_{WT}\Delta t}{0.5[(V_{dc0})^2 - (V_{dc}^{\min})^2]} \tag{0.46}$$

where the capacitors are designed to provide *x%* of the WTs nominal power rating S_{WT} for an expected time-length of the frequency transient given as Δt.

3.2.2 Inertial response emulation from rotor kinetic energy

To provide IR using the RKC method, the WT rotor is controlled to release/absorb KE by adding a frequency sensitive auxiliary signal p_{RKC} to the active power reference as illustrated in colour blue in Figure 9 as mostly found in literature [10], [18], [20], [29], [31], [48], [54]–[56]. Unlike SGs whose speeds are directly coupled to the network frequency, VSWTGs operate at rotor speed ω_r different from synchronous speed ω_s for both MPPT and deloading operations and thus, the speed variation of VSWTs can be much larger than the network frequency change. Consequently, the VSWT IR, which is a factor of the pre-disturbance rotor speed, can be several times of its natural inertia. The total kinetic KE ΔE_{RKC} released/absorbed by the RKC, with all the variables in the analysis in the per unit form, is given as:

$$\begin{aligned}\Delta E_{RKC} &= \int_{t_0}^{t_1} \Delta p_{RKC}(t)dt = \frac{1}{2}J(\omega_{r0}^2 - \omega_{r1}^2) \\ &= \frac{1}{2}J(2\omega_{r0}\Delta\omega_r - \Delta\omega_r^2)\end{aligned} \tag{0.47}$$

where ω_{r1} represents the rotor speed after the control; $\Delta\omega_r = \omega_{r0} - \omega_{r1}$ represents the rotor speed change; J represents the mechanical moment of inertia of the WT; the inertia duration is given by (t_0 -t_1). From (0.47), it is observed that the higher the pre-disturbance speed ω_{r0} of the WT, the higher the amount of energy released for RKC for a given change of rotor speed. It is

important to note that the WT ability to perform RKC depends on the available margin for absorbing/releasing KE under initial operating condition. For a WT operating close to the cut-in speed, due to low wind or under-speed deloading condition, RKC is not possible during under-frequency events because of lack of KE to release; similarly, for a WT operating close to the maximum speed, RKC is not possible during over-frequency events.

The auxiliary signal adopted in this work comprises of both RoCoF and frequency deviation proportional components and it is given by:

$$p_{RKC} = -K_{RKC\_I}\frac{df}{dt} + K_{RKC\_D}\Delta f \tag{0.48}$$

where K_{RKC_I} represents the inertia coefficient of the WT for generating the RoCoF component of the IR and K_{RKC_D} represents the droop coefficient for generating the frequency deviation component. Since Δp_{RKC} is added to the speed controller output, the rotor is driven to its original operating condition after the frequency fluctuation. This however contradicts the droop component of Δp_{RKC} which considers the steady-state frequency deviation and deteriorates the effectiveness of the RKC scheme. A modified active power reference for the WT can therefore be obtained as:

$$p^{*}_{MPPT} = p_{MPPT} + \Delta p_{RKC} \tag{0.49}$$

where p^{*}_{MPPT} is the modified active power reference for the WT. Due to the fast responses of power electronic devices, the assumption $p^{*}_{MPPT} = p_{WT}$ holds. Hence (0.13) can be rewritten as:

$$2H_S\omega_r\frac{d\omega_r}{dt} = p_W - p^{*}_{MPPT} \tag{0.50}$$

To assign the WT RSC with a IR constant H_R, (0.1) can be modified as (0.50) to give:

$$2H_R f\frac{df}{dt} = p_{WT0} - p^{*}_{MPPT} \tag{0.51}$$

where p_{WT0} is the initial value of the WT output power before the disturbance. Equating (0.50) to (0.51) gives:

$$2H_R f\frac{df}{dt} = 2H_s\omega_r\frac{d\omega_r}{dt} \tag{0.52}$$

Integrating both sides of (0.52), one obtains:

$$\int_{f_0}^{f} 2H_R f df = \int_{\omega_{r0}}^{\omega_r} 2H_s \omega_r d\omega_r \tag{0.53}$$

$$H_R\left(f^2 - f_0^2\right) = H_s(\omega_r^2 - \omega_{r0}^2) \tag{0.54}$$

where ω_{r0} represents the initial rotor speed before the disturbance. For small variations in system states during system dynamics, (0.54) can be linearized around its initial operating point as:

$$H_R f_0 \Delta f = H_s \omega_{r0} \Delta \omega_r \tag{0.55}$$

$$H_R = \frac{H_s \omega_{r0} \Delta \omega_r}{f_0 \Delta f} \tag{0.56}$$

From (0.56), it is observed that H_R depends on the pre-disturbance rotor speed ω_{r0} and the change of the rotor speed $\Delta\omega_r$. The larger ω_{r0}, the larger the amount of inertia that can be provided by the WT. Similarly, the larger $\Delta\omega_r$, larger the amount of inertia that can be provided by the WT. To understand the influence of the RKC gain parameters (i.e., K_{RKC_I} and K_{RKC_D}) on the inertia coefficient H_R, the following modifications can be made: Substituting (0.49) into (0.51) gives,

$$2H_R f \frac{df}{dt} = p_{WT0} - p_{MPPT} - \Delta p_{RKC} \tag{0.57}$$

Integrating both sides of (0.57) over time, one obtains:

$$\int_{t_0}^{t} 2H_R f \frac{df}{dt} = \int_{t_0}^{t} p_{WT0} dt - \int_{t_0}^{t} p_{MPPT} dt - \int_{t_0}^{t} \Delta p_{RKC} dt \tag{0.58}$$

$$2H_R f_0 \Delta f = p_{WT0} \Delta t - \int_{t_0}^{t} p_{MPPT} dt - \int_{t_0}^{t} \Delta p_{RKC} dt \tag{0.59}$$

$$H_R = \frac{p_{WT0}\Delta t - \int_{t_0}^{t} p_{MPPT} dt}{2 f_0 \Delta f} - \frac{\int_{t_0}^{t} \Delta p_{RKC} dt}{2 f_0 \Delta f} \tag{0.60}$$

$$H_R = \frac{p_{WT0}\Delta t - \int_{t_0}^{t} p_{MPPT} dt}{2 f_0 \Delta f} - \frac{\int_{t_0}^{t} \left(-K_{RKC\_I} \frac{df}{dt} + K_{RKC\_D} \Delta f\right) dt}{2 f_0 \Delta f} \tag{0.61}$$

The rotor speed controller output is computed by a PI controller whose gains are suitably selected to ensure transient speed variation for the RKC support and fast speed recovery afterwards. During speed recovery, the WT rotors absorbs energy which leads to a period of under-production (with output power lower than the pre-disturbance value) in the WT output power: this may be detrimental especially if the speed recovery occurs while the other

conventional generators have not increased their output enough to arrest the frequency decline. In [18], it is noted that for a proper generator performance, a rotor speed recovery time of 20s is fast enough. However, the time span of the network frequency transient depends on the dynamics of the network. For a network with fast dynamics, the frequency transients occur in a short time, usually in the order of about 2-3s and hence a speed-recovery time of 20s will be enough to provide dynamic frequency support. However, for a network with very slow dynamics, the frequency transients may occur in a relatively long period of time greater than 20s and the RKC may worsen frequency nadir.

3.2.3 Primary frequency response emulation from deloading

In VSWT, MPPT control is employed to maximize its energy conversion efficiency and makes the WT incapable to provide any long-term frequency support. For VSWT to participate in PFR, some amount of primary reserve must be established by deloading the WT output continuously by a constant proportion of the available maximum active power (known as delta control), by imposing an upper limit on the WT output (known as balance control) or by reserving a fixed amount of active power (known as fixed reserve) [10]. The delta deloading control is adopted in this work and it is designed to obtain a fixed percentage (%d) of the WT output as power reserve either by the over-speed deloading or the pitch deloading methods as illustrated in colour red in Figure 9.

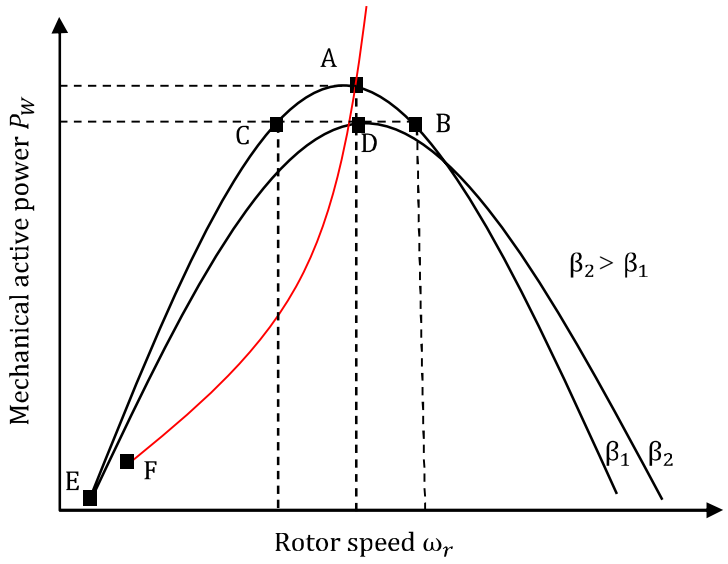

Figure 14. Deloading possibilities for a WT under a given wind speed.

The deloading concept is illustrated in Figure 14: when the turbine speed in increased (from the optimal operating point A to, e.g., B) or decreased (from A to, e.g., C), the mechanical power output reduces. These two techniques are termed as over-speed deloading and under-speed deloading, respectively. However, from the power system point of view, the under-speed deloading method may be unstable [30], [57]. As an alternative, pitch deloading is achieved by increasing the pitch angle β while maintaining the optimal rotational speed of the rotor (so to change the state condition from A to, e.g., D in Figure 14).

The over-speed deloading control increases the KE reserve of the rotation mass because of increased rotor speed above its optimum value. This is achieved by increasing the rotor speed reference ω_r^{ref} generated from the MPPT controller by a factor ω_o which corresponds to the desired active power deloading level *%d*. To perform PFR, the WT responds to frequency deviation by adjusting ω_o as follows:

$$\Delta\omega_r^{ref} = \omega_0(1+K_\omega\Delta f) \tag{0.62}$$

where $\Delta\omega_r^{ref}$ is the adjusted rotor speed deloading factor and K_ω is the adjustment coefficient.

For the pitch deloading, the pitch angle reference β^{ref} generated from the rotor speed limiting controller is increased by a factor β_o which corresponds to *%d*. To perform PFR, the WT responds to frequency deviation by adjusting β_o as follows:

$$\Delta\beta^{ref} = \beta_0(1+K_\beta\Delta f) \tag{0.63}$$

where $\Delta\beta^{ref}$ is the adjusted pitch angle deloading factor and K_β is the adjustment coefficient. The relationship between *%d* and ω_o/β_o is obtained from pre-defined curves.

For the DFIG unit considered with power curve shown in Figure 15, three speed wind speed regimes are identified for the present analysis: low wind speed regime denoted as zone 1 (<8 m/s), medium wind speed regime denoted as zone 2 (8-11 m/s) and high wind speed regime denoted as zone 3 (>11 m/s). At medium and high wind speeds regimes, there is the possibility of the rotor speed to exceed the maximum value during deloading operation. Hence, in the proposed strategy, over-speed deloading is adopted at the low-speed regime, a coordinated use of both over-speed and pitch deloading is adopted at the medium-speed regime, and pitch deloading is adopted at the high-speed regime.

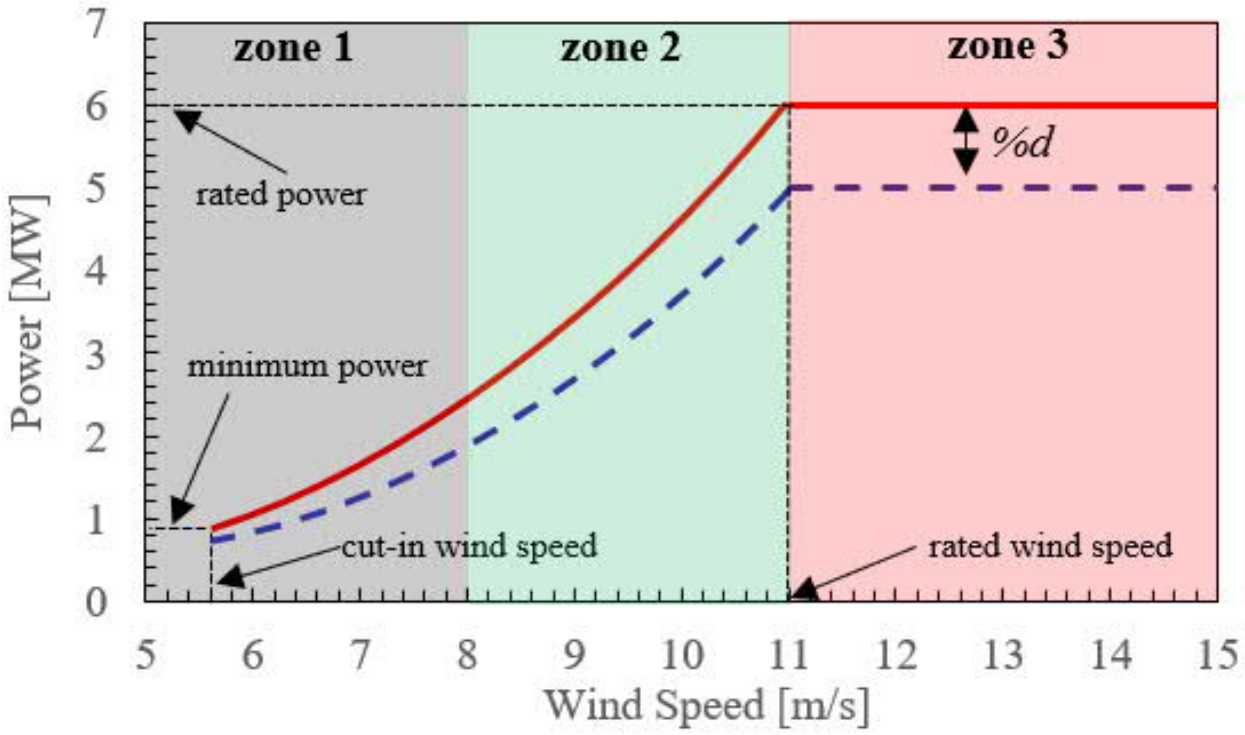

Figure 15. The WT power curve.

3.2.4 Frequency support from energy storage systems

Several energy-storage technologies have been classified and investigated for different grid applications such as improving power quality and providing frequency regulation to the grid during network disturbance [40], [58]–[60]. When employed in frequency regulation, ESS inject/absorb power to/from the grid in response to decrease/increase in network frequency. In Figure 16, the comparison of power ratings and rated energy capacities; also the nominal discharge time duration at the rated power are shown for different ESS technologies [61]. For IR services that require high-power low-energy density devices, Figure 16 indicate the suitability of the technologies on the left-hand side of the chart, with low energy capacity and less discharge time (e.g., supercapacitors and flywheels). However, despite of high-power density, these technologies cannot provide sustained energy support for long term PFR. Technologies such as lithium-ion batteries with typical discharge time ranges from 1-10 hours have sufficient energy to provide sustained support over the time horizon of PFR. Practical applications using BESS for frequency response include the recently installed 100 MW/129 MWh BESS unit of the Hornsdale Power Reserve in Australia [62] and the 300 MW/1200 MWh BESS unit at Moss Landing in California [63].

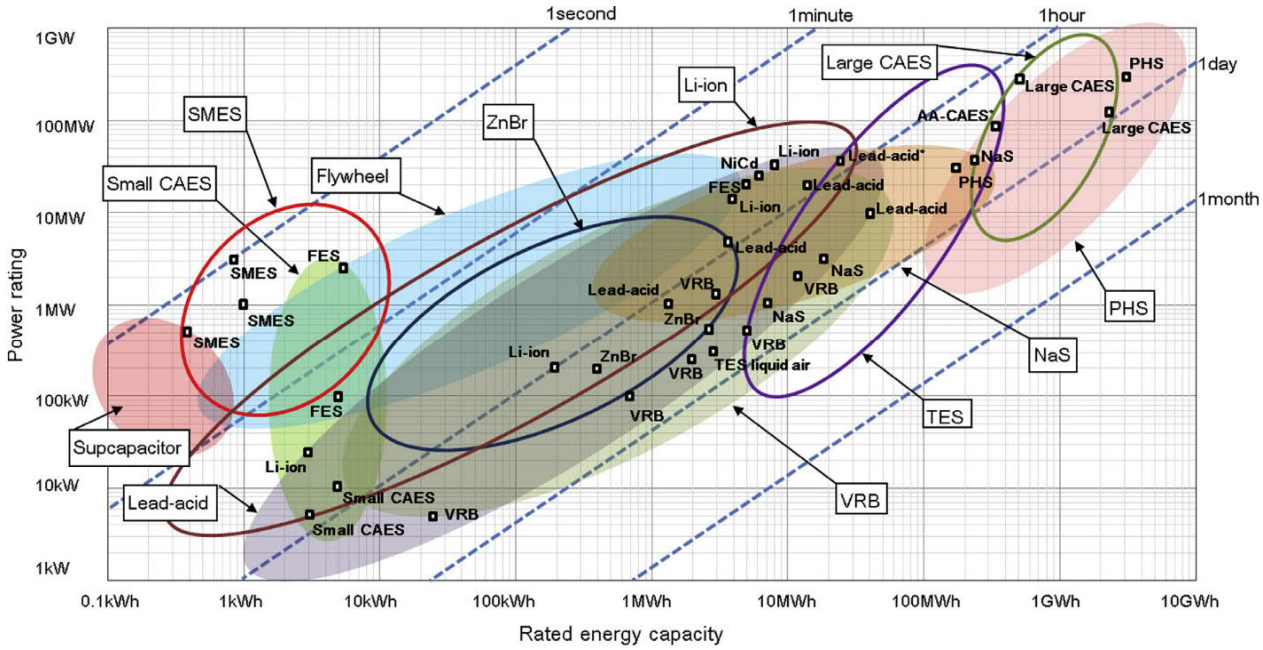

Figure 16. Comparison of power rating and rated energy capacity with discharge time duration at power rating [61].

Concerning placements of ESS, four potential locations already suggested in literature are analysed in this work as shown in Figure 17.

Location 1: This placement option is considered at the WT level with the ESS interfaced directly to the dc-link without employing a dc/dc converter as in Figure 17a. Ref. [64] proposed the use of Li-ion capacitor connected directly to the dc-link to smooth the power output of WTs. For the purpose of frequency regulation, [27] uses supercapacitor units connected directly to the dc-link of DFIG WTs to provide the needed IR support with results indicating that, the IR support can effectively reduce the system RoCoF and also provide damping to frequency oscillations. The merits of this configuration involve: (1) avoidance of addition conversion stage reduces cost and minimizes energy losses and, (2) reduction in complexity of control coordination. However, the demerits concerning this configuration are: (1) since the power released for the IR support passes through the GSC, the GSC would require the rerating to match the total expected power and (2) for the purpose of IR implementation whereby the energy released is linked to the magnitude of the dc voltage variation, the GSC operation limits the total available supercapacitor usable energy due to limitations in maximum allowed dc voltage variation of the GSC as already verified in Section 3.2.1B.

Location 2: This placement option is considered at the WT level with the ESS interfaced to the dc-link using a bidirectional dc/dc converter as in Figure 17b. In [65], the authors use supercapacitor units connected to the dc-link of DFIG WTs via a dc/dc converter to provide the needed IR needed to enhance the system small-signal stability. In this configuration, the minimum allowable supercapacitor voltage is not limited by PWM constraints of the GSC and can be zero if required. Hence, the total stored energy in the supercapacitor units can be utilized for the IR support. However, the demerits concerning this configuration are: (1) since the power released for the IR support passes through the GSC, the GSC would require the rerating to match the total expected power, (2) the addition conversion stage increases cost and energy losses and, (3) the addition conversion stage increases the complexity of control coordination.

Location 3: This placement option is considered at the WT level with the ESS interfaced to the WT via an dc/ac converter at the ac side of the GSC as in Figure 17c. From the point of view of energy transmission, there is no difference between Location 2 and Location 3. In [66], a BESS operating as a virtual synchronous generator was proposed to be connected to the ac side of the GSC. In this configuration, rerating of the GSC is avoided since the power released for the IR support does not pass through the GSC. However, the demerits concerning this configuration are: (1) the addition conversion stage increases cost and energy losses, and (2) the addition conversion stage increases the complexity of control coordination.

Location 4: This placement option is considered at the WF level with the ESS interfaced to the point of common coupling of the WF as in Figure 17d. This approach has been adopted in [66], [67].

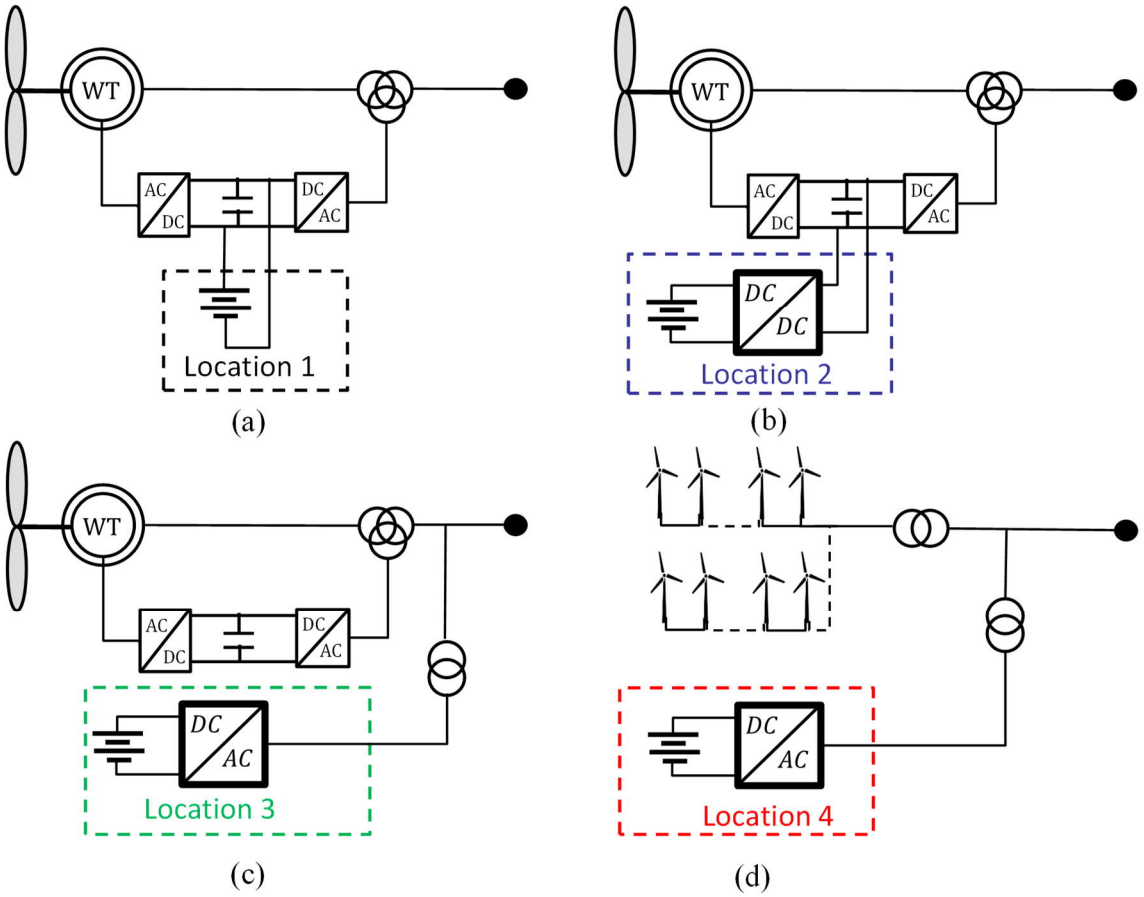

Figure 17. Considered locations for the ESS at (a) WT and (b) WF level.

Four typical control concepts usually adopted in literature for ESS for power system frequency response support are classified under two main categories, i.e., current-controlled and voltage-controlled architectures as indicated in Figure 18. The current-controlled architecture is sub-divided into the:

- Grid-following converters which are controlled as current sources that inject active and reactive power to the grid according to specified references by measuring the angle of the grid voltage using a phase-locked loop [68]. This mode of operation offers no dynamic frequency support to the grid.
- Grid-supporting converters are like the grid-following scheme which are further enhanced to provide dynamic frequency response by linking their active power control loop to frequency changes. This method has been termed as virtual synchronous generator in [69].

The voltage-controlled architecture is also sub-divided into the:

- Grid-leading converters which controlled to build the grid voltage by keeping the voltage angle and frequency fixed. This type of control, usually referred to as V/f control, is typically adopted in small islands and offshore grids, whereby the grid voltage is formed exclusively by one converter. In [70], this approach is adopted, whereby the voltage is regulated and the voltage angle or the frequency is given by an oscillator.
- Grid-forming converters which are controlled to build the grid voltage and simultaneously synchronise with other converters or generators. In literature, various concepts of grid-forming controls including virtual synchronous machines, synchronverter and droop control have been proposed [71], [72].

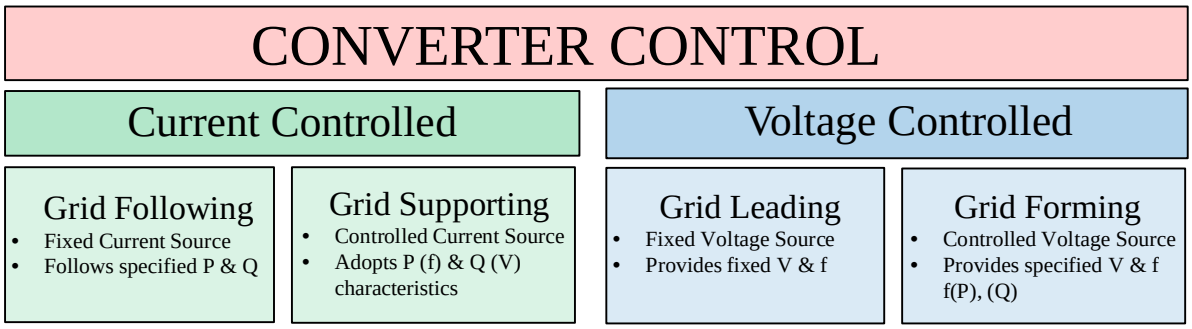

Figure 18. Classification of Converters – Grid Behaviour.

A. Adopted energy storage model

This sub-section presents the BESS model and its control scheme adopted in simulation studies of Section 2.2, Chapter 5 and Chapter 6. The BESS consists of the:

Battery Model: A simple battery model that depicts the terminal voltage and internal resistance is adopted in this study. The internal resistance is assumed constant and with a voltage source that is dependent on the batteries state of charge (SoC) defined by (0.64). Table 2 lists the battery parameters and values adopted in this paper.

$$U_{dc} = U_{\max} SOC + U_{\max}(1 - SOC) - I_{bat} Z_i \qquad (0.64)$$

where U_{dc} represents terminal voltage; I_{bat} the battery current.

Frequency Controller: The frequency controller is highlighted in 'Red' as shown in Figure 19. The variation in active power reference generated by the frequency controller consists of both the frequency derivative component and the frequency deviation component based on (0.3)

.

PV Controller: The PV controller is highlighted in 'Green' as shown in Figure 19. It is responsible for regulating the output active power and output voltage (or reactive power) to specified reference values. The voltage controller has a very slow integer-controller for set point tracking and a slope with a deadband for proportional voltage support.

Charger Controller: The charge controller is highlighted in 'Blue' as shown in Figure 19. It is responsible for achieving the described boundary conditions in Table 3 and limiting the absolute value of the current order.

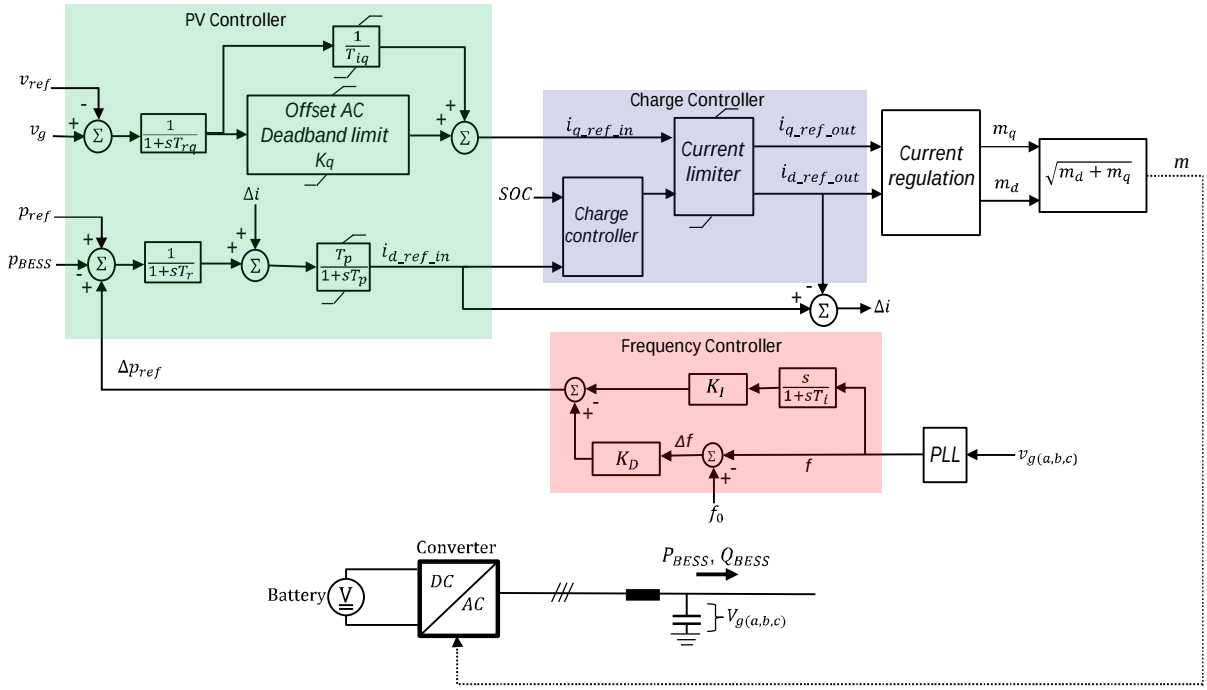

Figure 19. BESS control scheme. The adopted converter control is the grid supporting control mode.

Table 2. BESS parameters values.

Parameters	Value
SoC	0.8
Single Cell Capacity	1.2 Ah
Min. Voltage of empty cell	12 V
Max. Voltage of full cell	13.85
Number of parallel connected cells	60
Number of series connected cells	65
Nominal BESS Voltage	0.9 kV
Internal Resistance per cell	0.001 ohm

Table 3. Charge controller parameter values.

Parameters	Value
Charging Current	0.1 p.u.
Minimal SoC Discharge Current	0.0
Maximal SoC Charging Current	1.0
Rated Current	1.0 p.u.

3.3 Summary

Modern WTs are indeed programmable power sources which give them the flexibility to participate in power system stability support. To achieve this, their control system architecture needs to be elaborated, which allows the implementation and coordination of specific functionalities to meet these requirements. The development of these functionalities and architecture is addressed in the following chapters. The chapter finally presents a detailed description of a VSWT equipped with a DFIG and discusses the frequency control schemes and their respective energy buffers. The following schemes have been considered:

- Dc-link IR scheme that utilises the electrostatic energy stored in the dc-link capacitors. Under this scheme, two major architectures are identified and developed.
- RKC IR that exploits the KE of the WTs rotating mass. Proposals have been presented for adopting this scheme for networks with different kind of dynamic.
- The PFR service is guaranteed by a deloading scheme that reserves a portion of the maximum available power of the WT. The deloading scheme presented adopts a combination of both over-speed deloading and pitch deloading at different wind speed levels to provide the power required for long-term PFR. The controllers for the individual IR and PFR schemes are first presented and then the coordinated control scheme is derived.
- The possibility of using external storage devices to provide both IR and PFR has been discussed. Different ESS technologies, their potential locations and control strategies have been analysed. A detailed description of a BESS unit controlled in the grid-supporting mode has been presented.

Although the above analysis has been performed considering a DFIG WT unit, the main characteristics of the proposed approach can be adapted for other types of VSWTs.

Chapter 4. Validation of Dc-Link Inertial Response Architectures

In this chapter, the IR response provision capabilities of the CCM and VCM IR architectures (described in Section 3.2.1A) are first verified by means of dynamic simulation. Next, the chapter highlights the possibility of the architectures to coordinate with other frequency support schemes implemented on the WT unit, in this work the RKC IR scheme (described in Section 3.2.2). The comparison is first demonstrated by means of dynamic simulations and then by modal analysis studies.

4.1 Dc-Link IR Architectures: Inertial Response Comparison

In this section, the IR of CCM and VCM IR architectures are tested and compared by using a simple network as shown in Figure 20. For the sake of simplicity, the RSC side of the WT unit has been ignored and only the GSC side with supercapacitor storage connected to the dc-link has been simulated. A generic frequency signal shown in Figure 21, which is set to change from 50 Hz at t=50s to 48 Hz at t=52 s (representing a steady state deviation of 2 Hz and fixed RoCoF of 1 Hz/s) has been applied to the GSC unit implementing the IR architectures. The simulation parameters specified in Table 4.

For the study performed, an inertia coefficient H_{dc} of 1 s is to be emulated by the IR architectures. The values of K_{in_I} (of CCM architecture) and K_{in_V} (of VCM architecture) are estimated as 2 and 0.069 respectively based on (0.22) and (0.30) respectively. Based on (0.8) and (0.9), the required IR power and energy are estimated as 6 MW and 0.00333 MWh respectively.

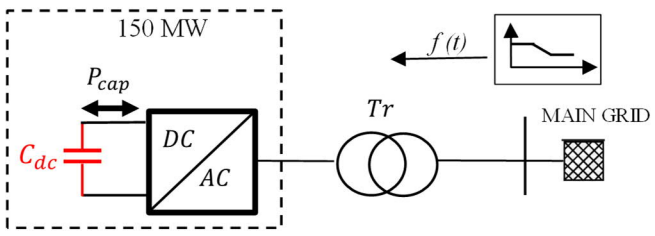

Figure 20. Adopted test network for the CCM and VCM IR architectures validation. Only the GSC side of the WT has been considered.

Table 4. Simulation parameters of GSC adopted for the comparison of CCM and VCM IRs.

Parameter	Symbol	Value
Rated power	S_{WT}	150 MW
Capacitance of supercapacitor	C_{dc}	100 F
dc nominal voltage	V_{dc0}	6.6 kV
Synthetic inertia coefficient	H_{dc}	1 s
Synthetic inertia time constant	T_{in}	0.1 s
Nominal frequency	F_0	50 Hz

In Figure 22, the supercapacitor output powers for both architectures are shown. For the VCM architecture, the IR power rises to the estimated 6 MW and maintain a constant value for the whole duration of the frequency transient, and it cuts off as soon as the RoCoF returns to zero after 2s. For the CCM architecture, the IR power rises to a maximum value of 5.4 MW and reduces gradually even when the RoCoF remains fixed at 1 H/s. After 2 s when the RoCoF returns to zero, the CCM IR is cut off. In Table 5, the ramp times (in this case defined as settling times: the time taken for the responses to reach 98% of final value) are presented for both IR architectures. As shown, the VCM architecture provides a faster response (almost ideal) compared to the CCM architecture. Concerning the IR energy, the VCM architecture produced 0.00333 MWh and agree with the estimated value whereas the CCM architecture provides a lower value of 0.003 MWh.

In Figure 23, the dc-link voltages are shown. For the CCM IR architecture, the dc voltage recovers its initial state once the frequency transient has passed unlike the VCM IR architecture where a permanent frequency deviation results in the dc voltage converging to a non-nominal steady state value. The opposing interaction of the slow dc-link controller to the CCM IR control (i.e., while the CCM IR scheme releases power from the supercapacitor units resulting in dc-link voltage reduction, the dc-link controller on the other hand tends to restore the dc bus voltage to its nominal value) results in the lower power and energy levels released for the IR implementation.

Table 5. Simulation results for IR architectures.

IR architecture	Active Power [MW]	Energy [MWh]	Response Time [s]
CCM	6	0.00333	0.052
VCM	5.4	0.00300	0.300

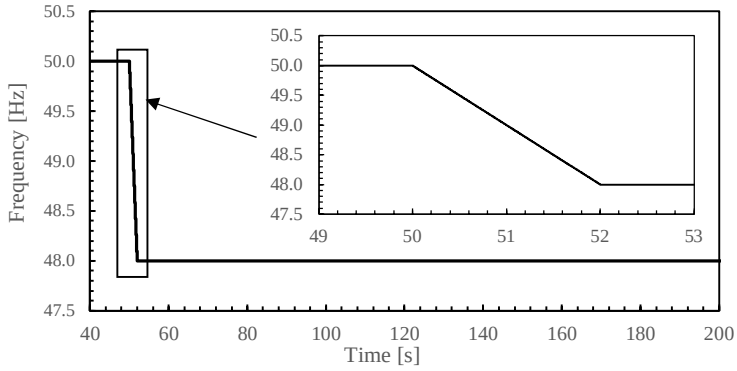

Figure 21. Frequency test signal.

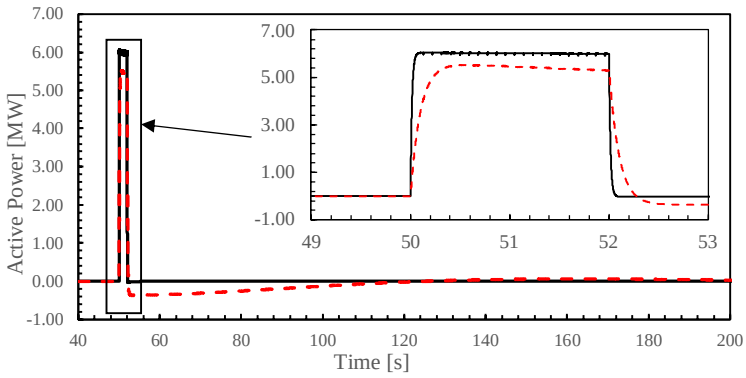

Figure 22. Active power response of the CCM and VCM IR architectures.

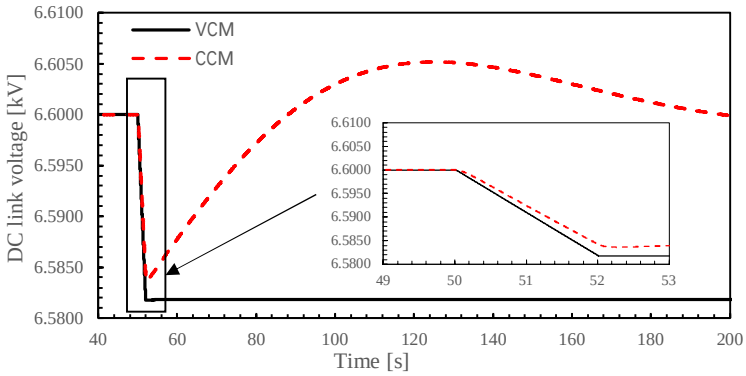

Figure 23. Dc-link voltages.

4.2 Dc-Link IR Architectures: Possibility to Coordinate with the RKC IR Scheme

In this section, the capability of the dc-link IR architectures to coordinate with other frequency support schemes of the WT is presented. In the coordinated control schemes proposed in this section for the analysis, the RKC IR scheme is chosen to form a coordinated control schemes with either of the dc-link IR architectures. The two coordinated control strategies proposed include:

- Strategy A: consisting of the CCM dc-link IR and the RKC IR and
- Strategy B: consisting of the VCM dc-link IR and the RKC IR.

4.2.1 Simulation studies

In this section, the impact of the resulting control strategies on both frequency response and small-signal stability are studied on a modified version of the well-known Two-Area network with 750 MW WF connected at bus 2 as shown in Figure 24. The capacitance of the dc-link supercapacitor is 33 F.

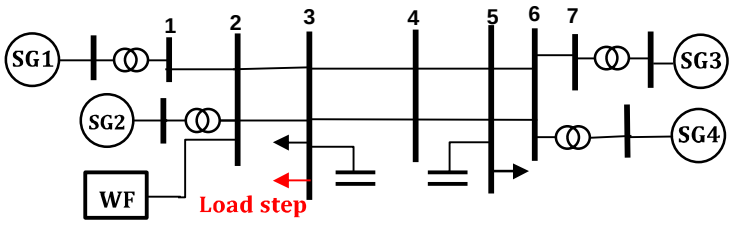

Figure 24. Modified version of the two-area network [88].

A. Frequency response

An under-frequency event initiated by the introduction of an active power load step on Bus 3 at time of 2s is used to study the impact of the control strategies on frequency response.

In Figure 25, the results are presented for the network: (a) without any IR support with (K_{RKC}, K_{in_I}) = (0,0), (b) RKC IR support provision adopting Strategy A with (K_{RKC}, K_{in_I}) = (20,0) and (c) RKC IR support provision adopting Strategy B with (K_{RKC}, K_{in_V}) = (20,0). Without IR support, the frequency experiences the minimum nadir. Strategy B improves the frequency nadir whereas Strategy A offers no improvement. From Figure 25b, both Strategies A and B release the transient IR power from the RSC into the dc-link. However, from Figure 25c, only Strategy B delivered the transient power through the GSC to the network while maintaining a fixed dc-link voltage. Due to the slow response of the dc-link voltage control adopted in control Strategy A, the transient power from the RSC results in an increased dc-link voltage and 'blocks' the power injection into the network as shown in Figure 25d.

In Figure 26, the results are presented for the network: (a) without any IR support with (K_{RKC}, K_{in_I}) = (0,0), (b) dc-link IR support provision adopting control Strategy A with (K_{RKC}, K_{in_I}) = (0,20) and (c) dc-link IR support provision adopting control Strategy B with (K_{RKC}, K_{in_V}) = (0,20). Both strategies improve the frequency nadir and delivers the transient power from the dc-link to the network. However, with control Strategy A, the dc voltage recovers its initial

state once the transient has passed unlike in control Strategy B where a permanent frequency deviation results in the dc voltage converging to a non-nominal steady state value.

In Figure 27, the results are presented for the network: (a) without any IR support with (K_{RKC}, K_{in_I}) = (0,0), (b) coordinated IR support provision adopting Strategy A with (K_{RKC}, K_{in_I}) = (20,20) and (c) coordinated IR support provision adopting Strategy B with (K_{RKC}, K_{in_V}) = (20,20). However, with IR provision, control Strategy B provides a better improvement in terms. For Strategy B, the transient power released to the network for frequency support consists of the rotor and dc-link IR powers whereas only the dc-link power is released for IR provision with strategy A. Hence, with the coordinated control, Strategy B provides a better support as compared to Strategy A.

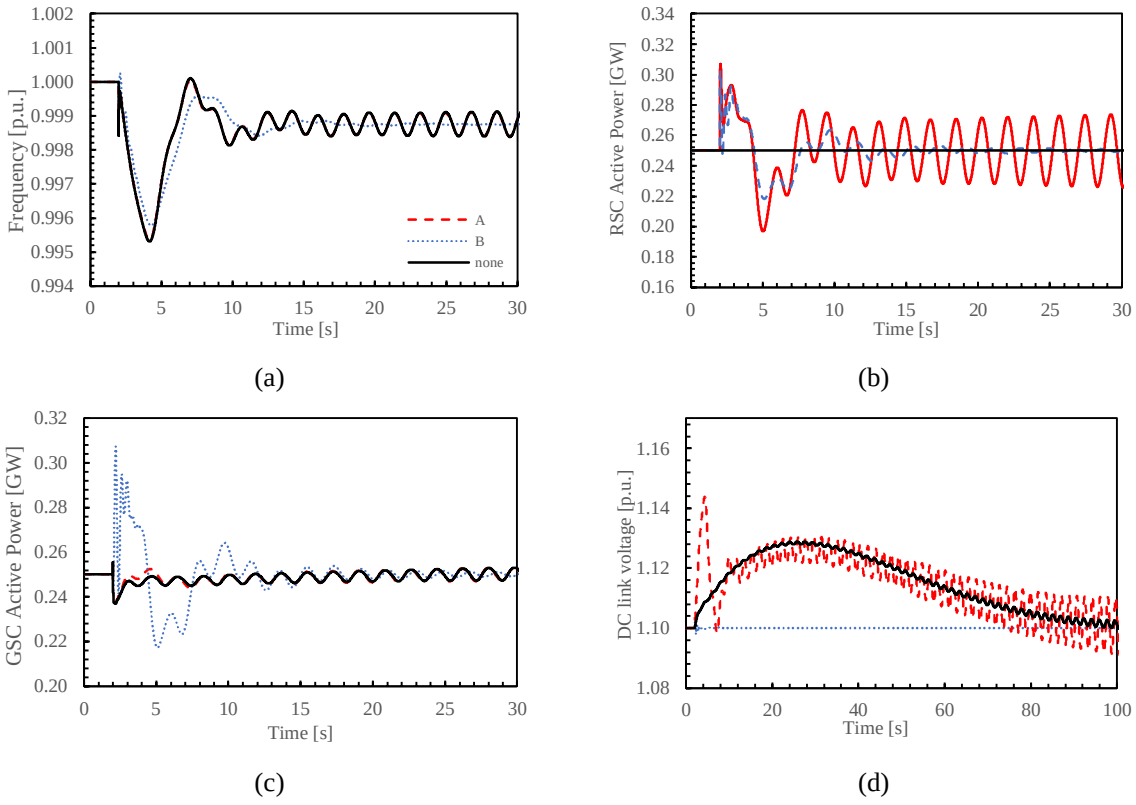

Figure 25. (a) Frequency (b) total WF RSC active power, (c) total WF GSC active power (d) dc-link voltage. Results presented for load step case for RKC IR.

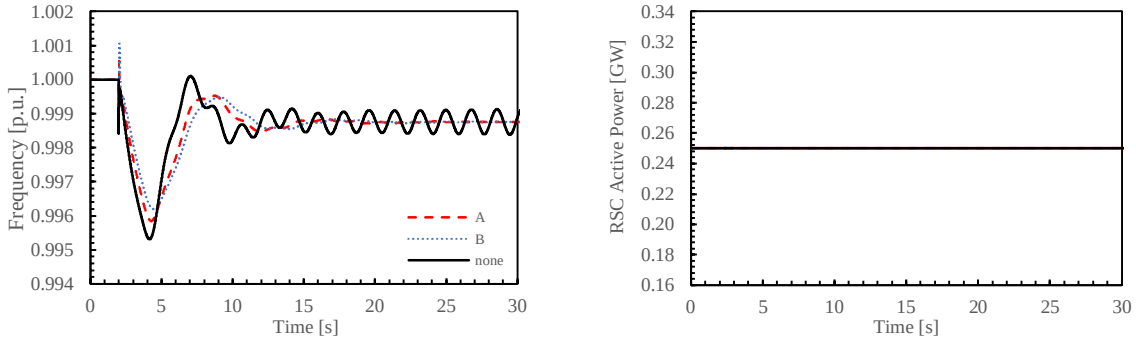

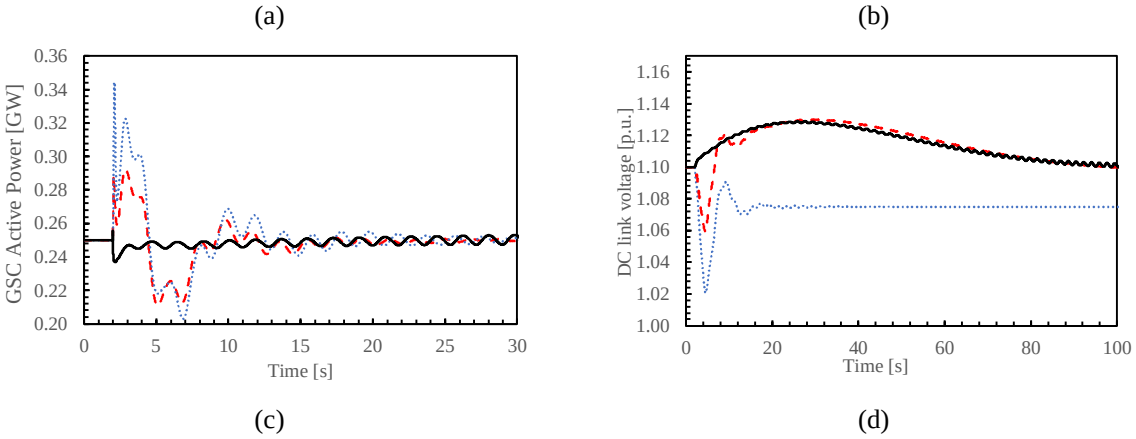

Figure 26. (a) Frequency (b) total WF RSC active power, (c) total WF GSC active power (d) dc-link voltage. Results presented for load step case for dc-link IR.

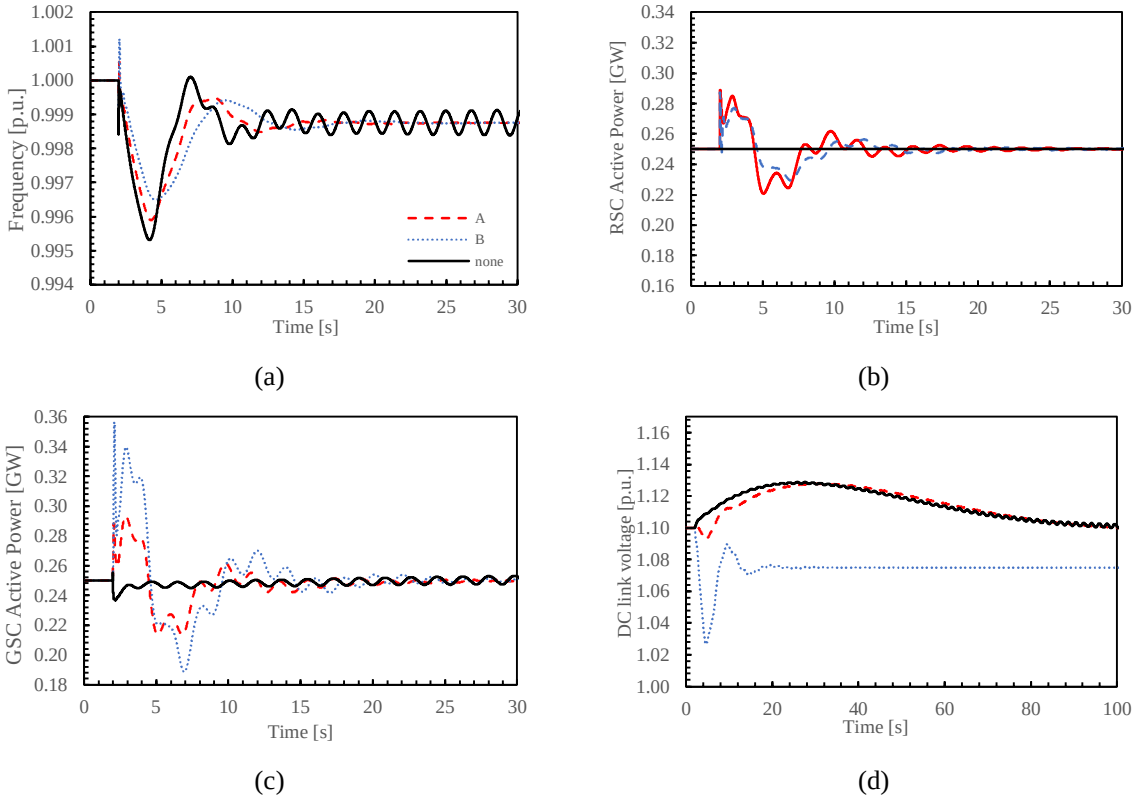

Figure 27. (a) Frequency (b) total WF RSC active power, (c) total WF GSC active power (d) dc-link voltage. Results presented for load step case for coordinated contribution of dc-link IR and RKC IR.

B. Modal analysis

A modal analysis is performed to study the impact of the control strategies on small-signal stability. Detailed analysis of modal analysis study is presented in Chapter 6. The network originally displays three EM modes: an inter-area mode and two local modes. In the inter-area mode, G1 and G2 oscillate coherently against G3 and G4.

The modal analysis is performed and repeated for different controller gain combinations, for both Strategy A and B, focusing on the inter-area mode and the results presented in Table 6. For Strategy A, increasing K_{in_I} improves the damping ratio of the mode with K_{RKC} having minimal effect. On the other hand, for Strategy B, both the individual and coordinated contributions from K_{in_V} and K_{RKC} significantly improve the damping ratio of the mode.

Table 6. Influence of control strategies A and B gain combinations on the inter-area mode.

(K_{RKC}, K_{in_I}) or (K_{RKC}, K_{in_V})	Strategy A		Strategy B	
	f (Hz)	ζ (%)	f (Hz)	ζ (%)
(0, 0)	0.58	0.61	0.58	0.46
(0,10)	0.57	2.84	0.56	2.83
(0,20)	0.56	4.19	0.55	3.69
(0,30)	0.55	4.89	0.54	4.04
(10,0)	0.58	0.64	0.57	2.27
(20,0)	0.58	0.66	0.56	3.48
(30,0)	0.58	0.68	0.56	4.21
(10, 10)	0.57	2.87	0.55	3.61
(20,20)	0.56	4.24	0.54	4.32
(30,30)	0.55	4.95	0.53	4.50

4.3 Summary

In this chapter, dynamic simulation tests have been conducted on the CCM and VCM IR architectures to validate their IR capabilities. By applying a generic frequency signal to the IR architectures, it has been shown the VCM IR architecture releases higher power and energy with a faster response time as compared to the CCM IR architecture for the same synthetized inertia coefficient.

Also, both frequency response and modal analysis results presented indicate that the CCM dc-link IR strategy cannot form a coordinated control with other frequency support strategies implemented on the generator side of the WT due to the slow response of the dc-link voltage controller. However, with the VCM dc-link IR strategy, it is possible to form a coordinated control with other frequency support strategies implemented on the generator side of the WT due to the fast response of the dc-link voltage controller.

Chapter 5. Enhanced Frequency Support by Coordinated Inertial and Primary Frequency Response Provision by Wind Turbine Generators

Existing literature on the potential involvement of VSWTs in frequency response support during transient and steady state conditions usually focus on the providing frequency support via the individual contribution of RKC, dc-link capacitor, PFR participation through deloading or a combination of any of these two (e.g. [7]-[19]). More specifically, in [23], [73], [74] the RKC scheme is adopted to provide IR. Due to the limited size of typical dc-link capacitors, [15], [27] propose the use of supercapacitors to increase the IR of the WT. The possibility of exploiting the combined inertia support provided by the dc-link and RKC schemes of VSWTs are presented in [20], [26], [48]. The control strategies proposed in these schemes are focused on the improvement of the frequency transient, but they do not facilitate participation to PFR services due to the lack of power margin required to sustain the output power increase during persistent low-frequency transients. For the provision of PFR services, [75], [76] propose the shifting of the WT operating condition from MPPT to create the required margin. These works have not considered the self-inertial capabilities of the turbines. In [32], [56], [77], the possibility of exploiting both IR and PFR is explored. The proposed control strategy adopts a combination of RKC and deloading control with results indicating that the combined scheme provides a better improvement in the network frequency response as compared to when only one of the schemes is adopted.

In this chapter, a coordinated control scheme is proposed to fully utilize the WT (referring to a DFIG WT) potential contribution to IR and PFR. For the IR services, both the RKC and dc-link schemes are utilized, while the proposed deloading scheme is adopted for the PFR services.

The first part of this chapter presents the coordinated control scheme aimed at fully exploiting these capabilities. Subsequently, simulation results are presented on two different types of grids: a single bus medium voltage network that represents a system with fast dynamics; and a modified version of the New England 10-machine 39-bus high voltage network that represents a system with slow dynamics. Moreover, for different network disturbances (such as active

load power steps and three-phase short circuit faults) and wind conditions, the performance of the support schemes are compared to the case in which a large-scale centralized BESS unit is employed to provide frequency support services. Simulation results are presented in DIgSILENT PowerFactory environment.

5.1 Coordinated IR and PFR Control

In the proposed coordinated control scheme, both the RKC and dc-link capacitor simultaneously provide IR whereas the deloading control scheme provides PFR during frequency events. With this strategy, the WT self-inertia capability is fully utilized to provide short term frequency support whereas the available energy reserve supports long term frequency regulation. In the low wind speed range, DFIG adopts the dc-link inertia control, the RKC and over-speed deloading strategy. In the medium wind speed range, DFIG adopts the dc-link inertia control, the RKC and a coordinated use of both over-speed and pitch deloading. In the high-speed range, DFIG adopts the dc-link inertia control, the RKC and the pitch deloading strategy.

The sequence and time frame of the control actions is described below.

- Immediately after the disturbance, the inertial control provided by the dc-link acts on the RoCoF and dies out in few seconds.
- The inertial control provided by the RKC scheme lasts a few more seconds because of the droop component in its control scheme. The speed controller regulates the rotor speed to its original value and the support dies out after some seconds.
- The deloading control scheme response remains for an extended period until a secondary control takes over to restore the network frequency to the nominal value.

5.2 Simulation Studies

The frequency response of a network is influenced by a number of parameters such as system inertia, droop coefficient, damping ratio, time constants, generation capacity, load disturbance etc. and these differ from system to system [78]. The frequency of networks with slow dynamics (usually characterized by very large inertia and with units equipped with slow acting governors such as steam turbine governors) after a perturbation experiences a slow rate of change and

takes a long time to reach its nadir before the slow-acting governors react fully to arrest the decline. The opposite phenomenon is experienced in networks with fast dynamics (usually characterized by low inertia and with units equipped with fast acting governors such as hydro turbine governors).

In this section, time domain simulations are presented to demonstrate the effectiveness of the individual frequency support schemes and the proposed coordinated support scheme on two different networks representing system with fast and slow dynamics. Both load steps and three-phase faults are considered to simulate frequency and voltage events respectively.

5.2.1 System with fast dynamics

The network used in this study is shown in Figure 28 and it consists of a 15 MVA SG (equipped with a hydro turbine governor and an exciter) serving as the grid and a 6 MW DFIG wind unit. The SG is given an inertia constant of 2.0 s. To achieve the reserve requirement, a 5% deloading is applied to the wind unit at all wind speeds. The frequency disturbance is initiated by the introduction of a fixed load step of 1 MW at 10 s. Three different scenarios are considered, aiming at showing the effect of the individual and coordinated control schemes at three different values of wind speed levels, after the application of a load step event.

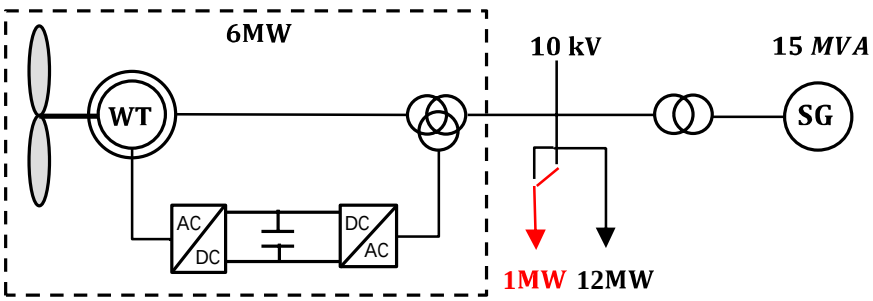

Figure 28. Test network representing a system with fast dynamics.

Scenario 1: In this scenario, it is assumed that the WT is operating in the high wind speed range with constant wind speed (11 m/s). The penetration level of wind generation is approximately 50%. Figure 29a show the frequency of the network and Table 7 presents the frequency nadirs. It can be observed that without any frequency support from the WT, the frequency takes only 1s to reach the nadir and the fast-acting SG governors quickly react to arrest the frequency to a new steady state. All the support schemes improve the frequency nadir. The deloading scheme, although with available power reserve and its droop implementation, provides the least improvement in the frequency nadir. This is because of the slow response of the pitch angle

controller. The dc-link scheme provides a minor improvement in the frequency nadir even without the lack PFR implementation. On the contrary, the RKC scheme provides a major improvement in the frequency nadir. With the coordinated scheme, the nadir has the maximum value. In terms of steady state frequency, only the deloading scheme and the coordinated scheme provides an improvement. The active power, rotor speed and pitch angle for all schemes are shown in Figure 29b, c, and d respectively. From the active power curve for the RKC scheme, it can be observed that the over-production lasts for at least 5 s, enough time for the SG governor to pick up fully and restore the frequency to a new steady state.

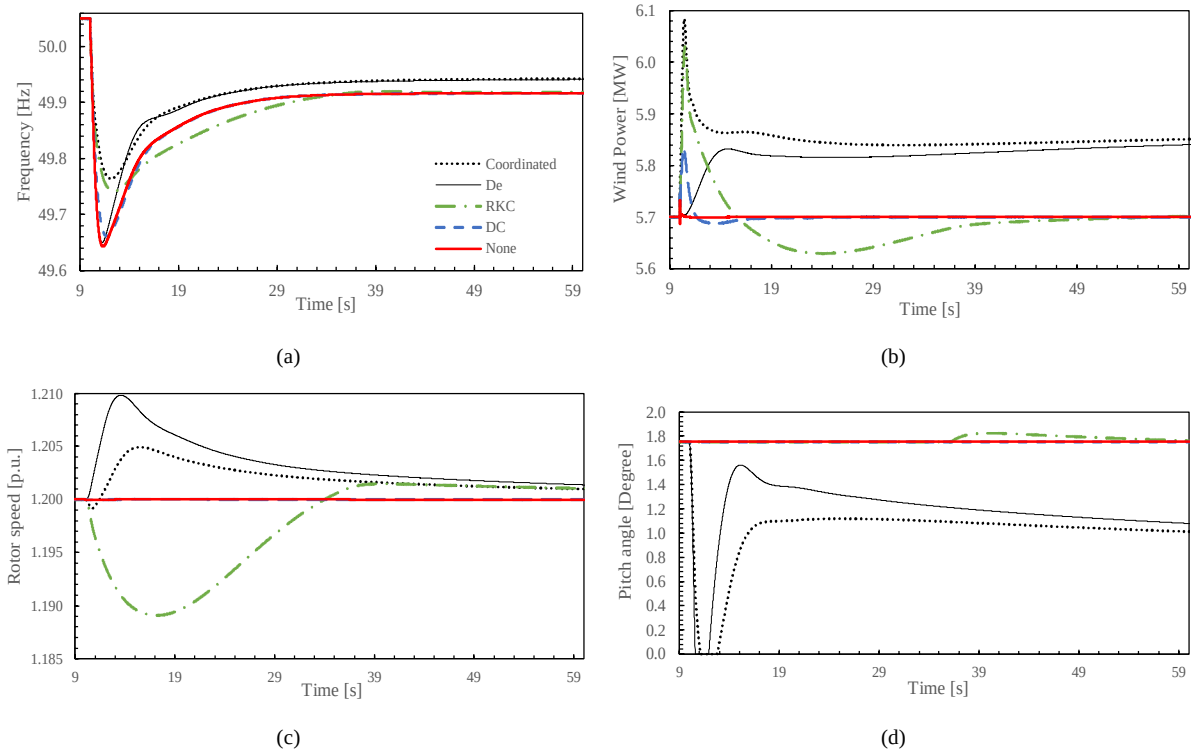

Figure 29. (a) Frequency (b) active power (c) rotor speed and (d) pitch angle in response to a load step for Scenario 1.

Scenario 2: In this scenario, it is assumed that the turbine is operating in the medium wind speed range with constant wind speed (9 m/s). The penetration level of the wind generation is approximately 30%. Figure 30a show the frequency of the network and Table 7 presents the frequency nadirs. Similarly, all the support schemes improve the frequency nadir. The results for the dc-link and RKC schemes are similar to those of Scenario 1. However, the deloading scheme in this scenario provides a major improvement in the nadir. This is because the active power provision for the deloading scheme is partially provided by the dynamic change in the rotor speed setpoint through fast-acting power electronics interface. Also, with the coordinated

scheme, the nadir has the maximum value. The active power, rotor speed and pitch angle for all schemes are shown in Figure 30b, c and d respectively.

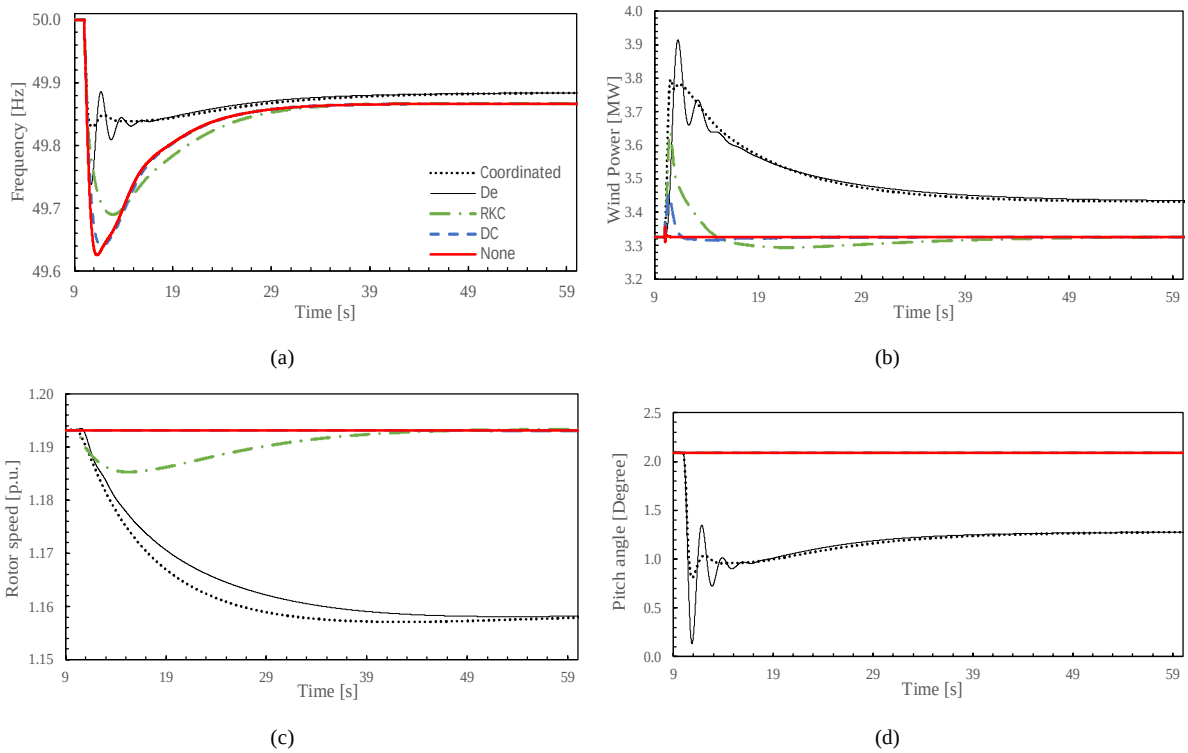

Figure 30. (a) Frequency (b) active power (c) rotor speed and (d) pitch angle in response to a load step for Scenario 2.

Scenario 3: In this scenario, it is assumed that the turbine is operating in the low wind speed range with constant wind speed (6.8 m/s). The penetration level of the wind generation is approximately 13%. Figure 31a shows the frequency of the network and Table 7 presents the frequency nadirs. All the support schemes improve the frequency nadir. The results for the dc-link and RKC schemes are similar to those of Scenario 1. The wind active power, rotor speed and pitch angle for schemes are shown in Figure 318b, c and d respectively. The pitch angle remains zero in all the schemes. The improvement in steady state frequency deviation (7.5 mHz) is lower in this scenario compared to in Scenario 1 (24.92 mHz) and in Scenario 2, (18.34 mHz). This is because the power margin for the adopted delta deloading scheme is higher for increasing wind speed. For the three scenarios considered, the power margins for the 5% deloading are 0.05 pu, 0.025 pu, and 0.0125 pu for Scenario 1, 2, and 3 respectively.

As expected, networks with fast dynamics require fast acting power sources to significantly improve the frequency response, which the analysis performed has allowed to quantify.

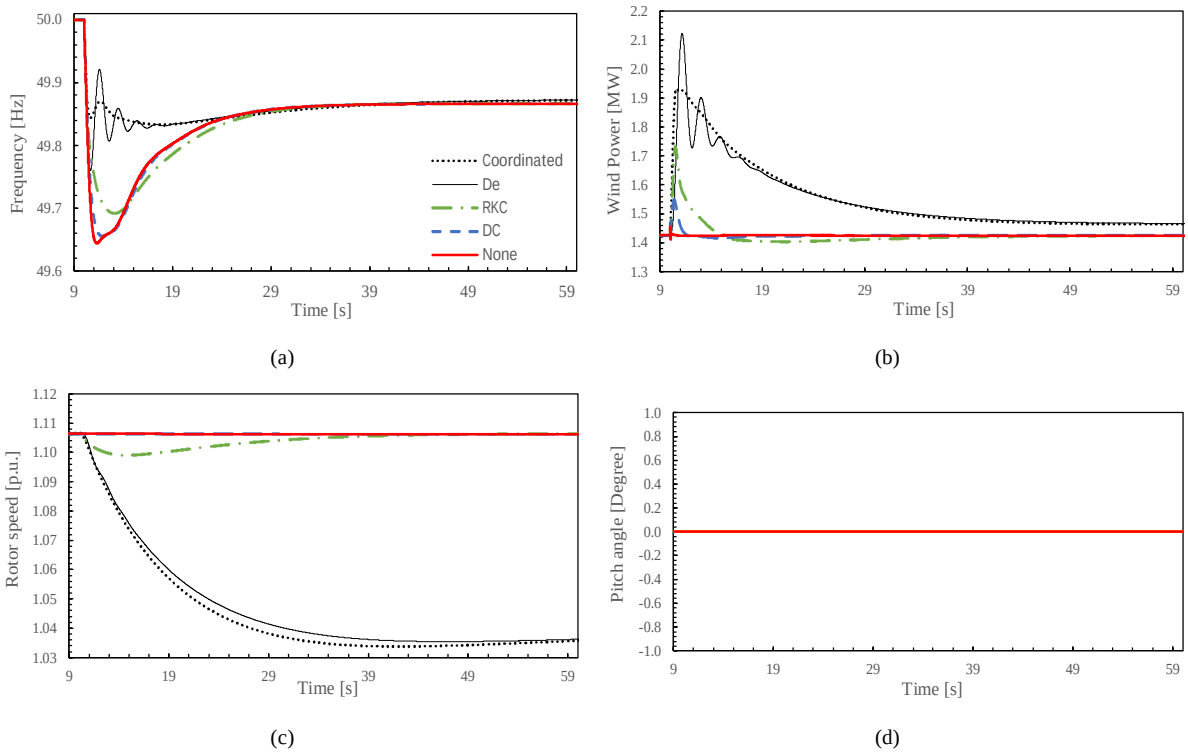

Figure 31. (a) Frequency (b) active power (c) rotor speed and (d) pitch angle in response to a load step for Scenario 3.

Table 7. Frequency nadir in Hz for the three considered scenarios.

Scenario	Control scheme				
	None	dc-link	RKC	De	Coord.
1	49.59	49.61	49.69	49.60	49.71
2	49.63	49.64	49.69	49.74	49.83
3	49.64	49.66	49.69	49.76	49.83

5.2.2 System with slow dynamics: New England 10-machine 39-bus network

A modified version of the New England 10-machine 39-bus network, which represents a simplified model of the transmission system in New England area, USA shown in Figure 32 is used in this section. The original 345 kV network consists of 10 synchronous generator units supplying 19 loads. For all the parameters we make reference to as in [79]. Unit G1 has no governor, G2 to G9 are equipped with a slow steam turbine governor model with droop of 20%, G10 is equipped with a fast hydro turbine governor model with droop of 4%. The loads are represented as PQ buses. For this study, G3, G4 and G9 are replaced by WFs denoted as WF3, WF4 and WF9 respectively with equivalent ratings. The total inertia of the modified network without any frequency support from the WFs is equivalent to 68.38 GVAs.

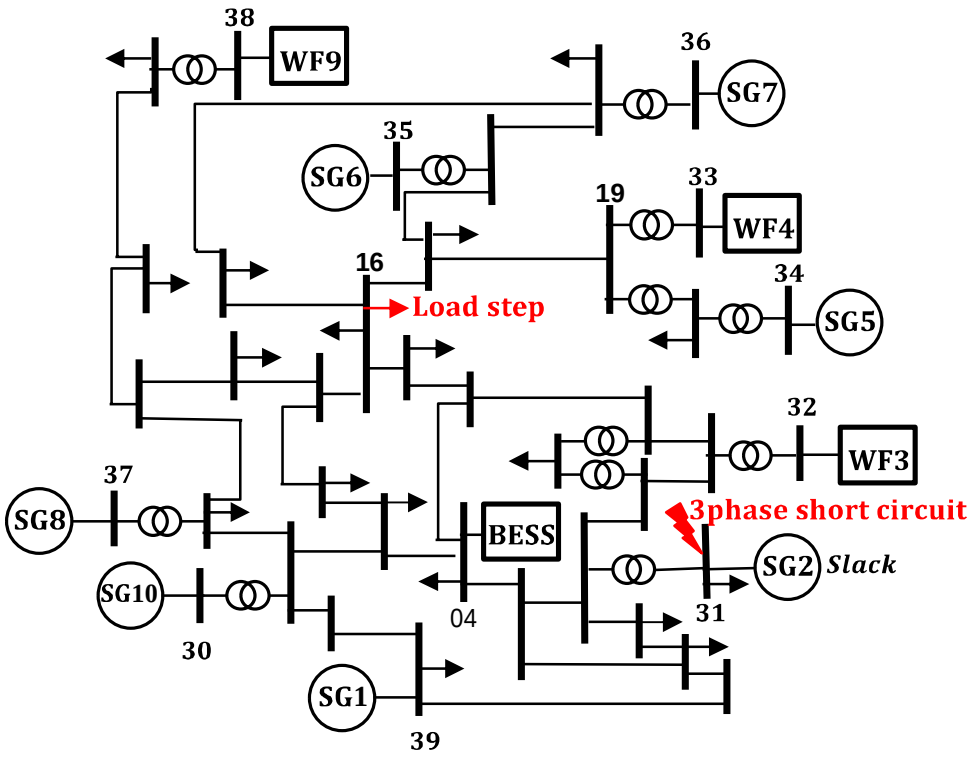

Figure 32. Single line diagram of the 39-Bus New England System with synchronous generators at bus 32, 33 and 38 replaced with WFs. A 130MVA BESS unit is installed at bus 4.

The case studies are selected to analyze the WF active power frequency response, for the cases of load changes and short circuits, as described in detail in the next subsections. The results obtained by using the proposed control scheme is compared with those obtained by using an external energy storage device for frequency support. The energy storage unit employed consists of a single centralized 130 MVA BESS unit (representing 5% of the total WFs ratings, which corresponds to the maximum WF deloading at high wind speed) installed at bus 04. It is assumed that the total output power of the BESS is available for frequency support in all scenarios. The BESS model adopted in this study is equipped with both IR and PFR capabilities with control scheme described in Section 3.2.4A. The BESS controller gains are tuned to provide similar frequency support to the case where a 5% pitch-angle based deloading is applied to all WFs operating in the high wind-speed range.

A. Load change

The under-frequency events are initiated by the introduction of an active power load step of 450 MW (representing approximately 7% of the total demand) at Bus 16. Five different scenarios are considered. The scenarios are defined to simulate the impact of either different WF deloading levels (scenarios 1, 2 and 3), different wind speed level (scenario 4) or varying

nature of wind speed (scenario 5) on the frequency support provision schemes. Results and relevant discussion follow

Scenario 1: In this scenario, all WFs are operating in the high wind speed range with different constant wind speeds. The penetration level of wind generation is approximately 35%. A 5% pitch-angle deloading is applied to all WFs. The simulation results in this study are presented considering the individual contributions from all the support schemes and the coordinated control scheme compared to the case of BESS. In the next scenarios, the results will be presented for only the coordinated control scheme and the BESS case. The simulation results are presented in Figure 33 and Table 8 presents the frequency nadirs. In Figure 33a, it can be observed that without any frequency support from the WFs, the frequency takes about 25 s to reach the nadir before the slow-acting SGs governors react enough to restore it to a new steady state. The dc-link IR scheme has no significant influence on the frequency because of the limited capacitance and permitted variability range of the dc-link voltage. The RKC IR scheme although, improves the initial RoCoF, it worsens the frequency nadir. The rotor speed recovery schemes cut off the RKC IR when the conventional SGs have not increased their output powers enough to arrest the frequency decline. During the speed recovery period, the WFs undergo an underproduction period which worsens the frequency nadir. Increasing the RKC frequency controller gains further worsens the nadir. Both the deloading and BESS cases provides similar improvement in frequency nadir and steady state frequency. However, the coordinated control scheme provides the best improvement in the frequency nadir. In Figure 33b, the total output power of all the WFs is shown while the output power for the case of BESS is shown in Figure 33c. In this scenario, both the deloading scheme and the BESS provide sufficient power for the underfrequency event. This is evident from the similar frequency response of the deloading and the BESS schemes. The coordinated support scheme of the WFs provides the largest initial increase in power needed to improve the nadir.

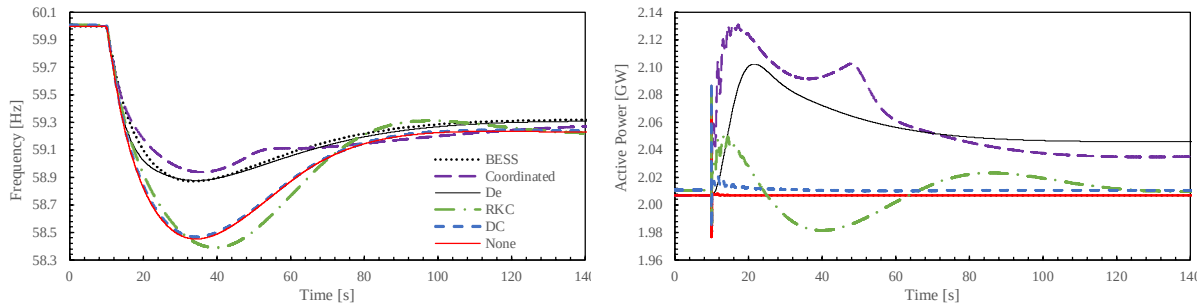

(a) (b)

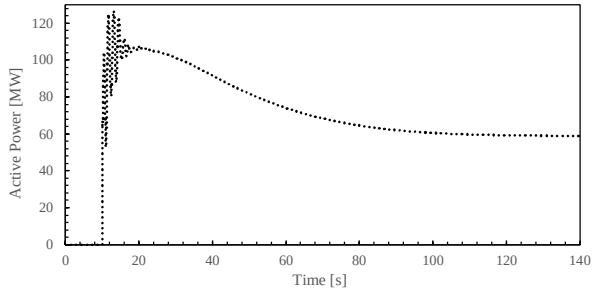

(c)

Figure 33. (a) Frequency (b) total active power of WFs and (c) active power of BESS. Results presented for Scenario 1 of load step case.

Table 8. Frequency nadir in Hz for scenario 1 of the load change case.

Scenario	Control scheme					
	None	dc-link	RKC	De-loading	Coord.	BESS
1	58.45	58.47	58.39	58.88	58.93	58.87

Scenario 2: In this scenario, the 5% pitch-angle deloading is applied to WF3 and WF4 only. WF9 is without deloading. As in Scenario 1 all WFs are operating in the high wind speed range with different constant wind speeds and wind generation is approximately 35%. The simulation results are presented in Figure 34 and Table 9 presents the frequency nadirs. In Figure 34a, it is observed that BESS case provides a highest nadir compared to the coordinated control scheme. In Figure 34b, the total output power of all the WFs is shown while the output power for the case of BESS is shown in Figure 34c. It can be observed that the change in output power of the WFs for the coordinated scheme is less than the output power of the BESS for the frequency support. The limited output power of the WFs available for frequency support provided by the deloading scheme results in the coordinated scheme providing less improvement in frequency as compared to the BESS.

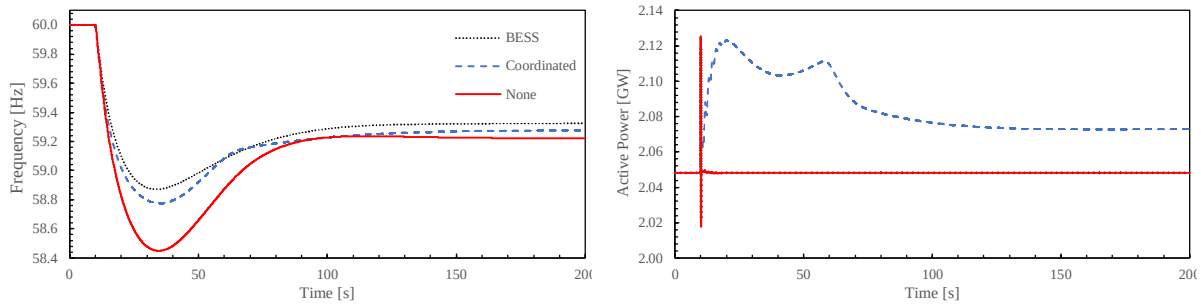

(a) (b)

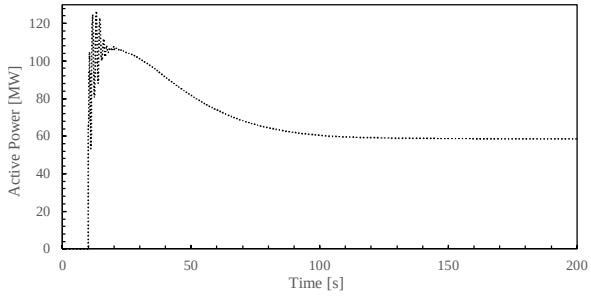

(c)

Figure 34. (a) Frequency (b) total active power of WFs and (c) active power of BESS. Results presented for Scenario 2 of load step case.

Scenario 3: In this scenario, the 5% pitch-angle deloading is applied to WF3 only. WF4 and WF9 are without deloading. As previous scenarios, all WFs are operating in the high wind speed range with different constant wind speeds and wind generation is approximately 35%. The simulation results are presented in Figure 35 and Table 9 presents the frequency nadirs. In Figure 35a, it is observed that BESS case provides a higher nadir compared to the coordinated control scheme. Also, the improvement in nadir by the coordinated scheme is less compared to scenarios 1 and 2. This is due to the very limited power available for frequency support provided by the deloading scheme. In Figure 35b, the total output power of all the WFs is shown while the output power for the case of BESS is shown in Figure 35c.

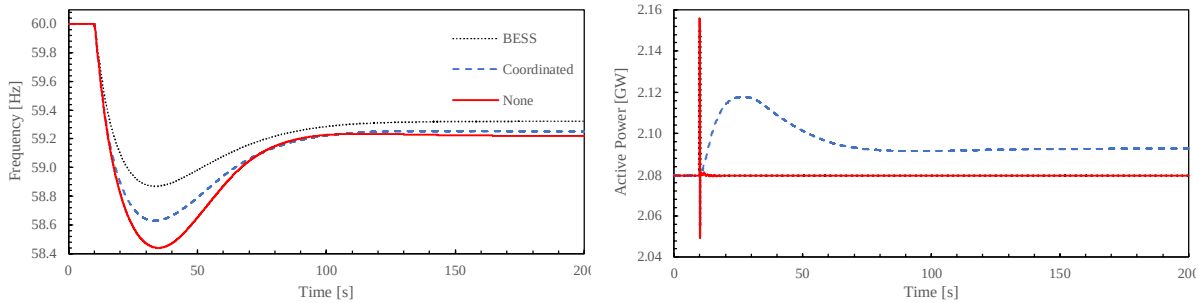

(a) (b)

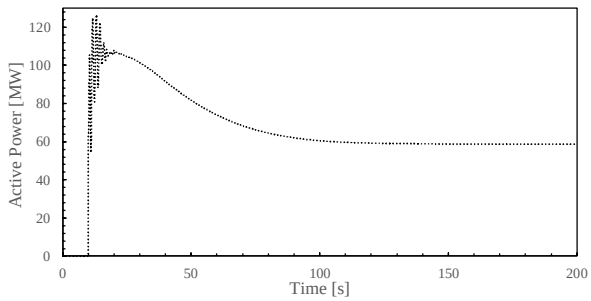

(c)

Figure 35. (a) Frequency (b) total active power of WFs and (c) active power of BESS. Results presented for Scenario 3 of load step case.

Scenario 4: This scenario assumes that WF3 and WF4 are operating in the high wind speed range while WF9 operates in the low wind speed range with different constant wind speeds. Wind generation is approximately 25%. The 5% pitch-angle deloading is applied to WF3 and WF4. A 5% overspeed deloading is applied to WF9. The simulation results are presented in Figure 36 and Table 9 presents the frequency nadirs. In Figure 36a, it is observed that BESS case provides the highest nadir. In Figure 36b, the total output power of all the WFs is shown while the output power for the case of BESS is shown in Figure 36c. It can be observed that the change in output power of the WFs for the coordinated scheme (22 MW) is less than the change in output power of the BESS (58 MW) for the frequency support although all the WFs were subjected to a 5% deloading as in scenario 1. This is because, the amount of active power reserve of the WFs decreases with decreasing wind speed for the same deloading percentage.

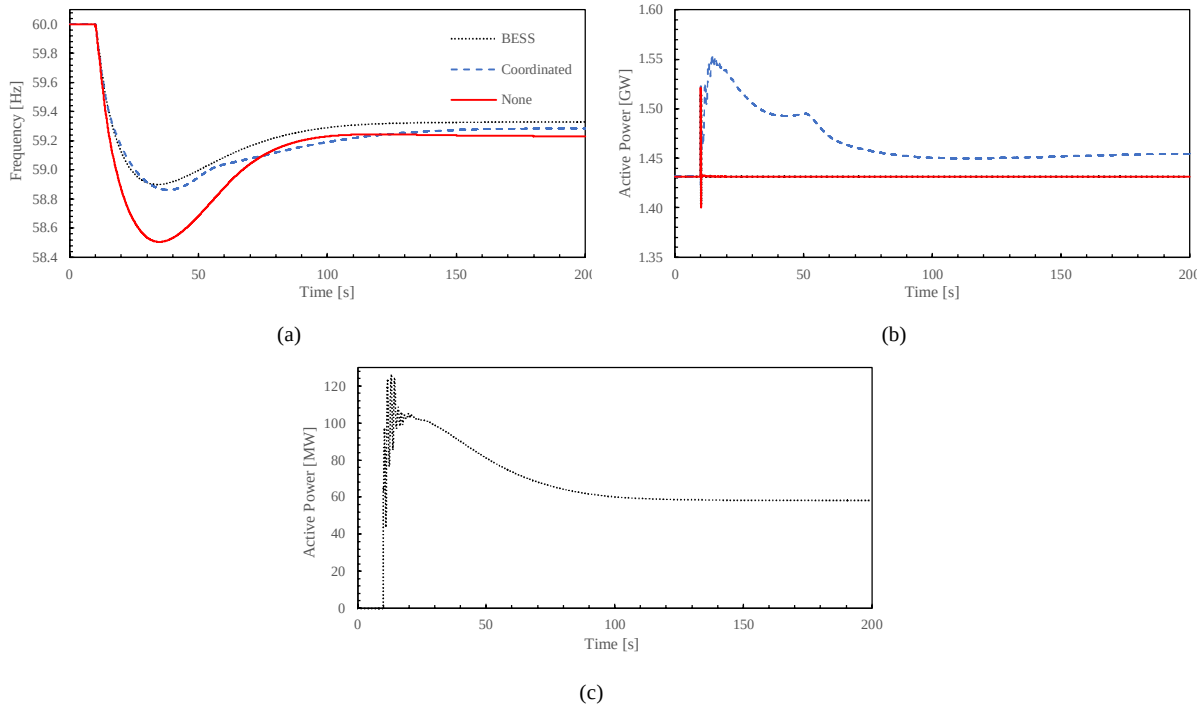

Figure 36. (a) Frequency (b) total active power of WFs and (c) active power of BESS. Results presented for Scenario 4 of load step case.

Scenario 5: In this scenario, all WFs are operating in the high wind speed range. However, WF9 is subjected to a variable wind speed pattern. A 5% pitch-angle deloading is applied to all WFs. The simulation results are presented in Figure 37 and Table 9 presents the frequency nadirs. Figure 37a, b, c, d, e and f show the wind speed pattern, the frequency response, the total active power of WFs and BESS, the rotor speed and pitch angle of WF9 turbines, respectively. The improvement in nadir and steady state frequency are similar to what observed and discussed for scenario 1.

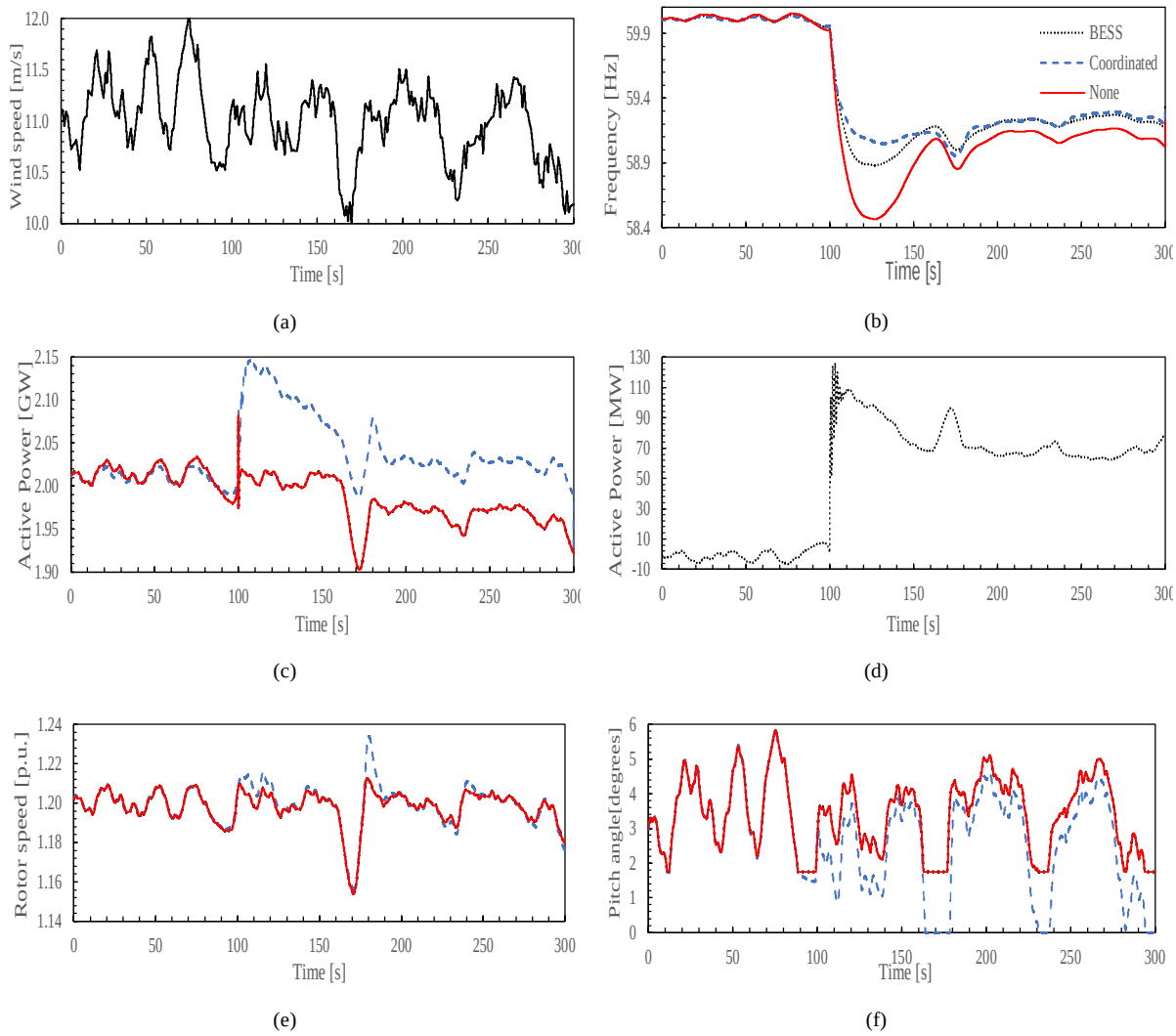

Figure 37. (a) variable wind speed (b) frequency (c) total active power of WFs (d) active power of BESS (e) rotor speed and (f) pitch angle of turbines of WF 9. Results presented for Scenario 5 of load step case.

Table 9. Frequency nadir in Hz for the five considered scenarios of Load change case.

Scenario	Control scheme		
	None	Coord.	BESS
2	58.45	58.78	58.87
3	58.44	58.63	58.87
4	58.51	58.86	58.90
5	58.47	58.88	59.04

B. Three-phase fault

The voltage event is initiated by introducing a three-phase short circuit at bus 31 at time 10s and cleared after 200ms. All WFs are operating in the high wind speed range with different constant wind speeds. Wind generation is approximately 35%. A 5% pitch-angle based deloading is applied to all WFs. The simulation results are presented in Figure 38 and Table

10. The fault leads to a severe 100% voltage depression at bus 31 shown in Figure 38b. From Figure 38a, it can be noticed that without any frequency support scheme, the frequency has the maximum value. Both the coordinated control and the centralized BESS scheme significantly improve the frequency zenith. With the coordinated control scheme, a significant enhancement of the oscillation damping is observed, and the frequency rapidly settles to steady state compared to the case without any frequency support and the centralized BESS scheme. Figure 38c, d, e and f show the total active power of WFs, total reactive power of WFs, active power of BESS and reactive power of BESS respectively.

Table 10. Simulation results for three-phase fault case.

	Control scheme		
	None	Coord.	BESS
Maximum frequency [Hz]	60.22	60.17	60.19
Time for frequency stabilization [s]	29.93	17.64	29.93

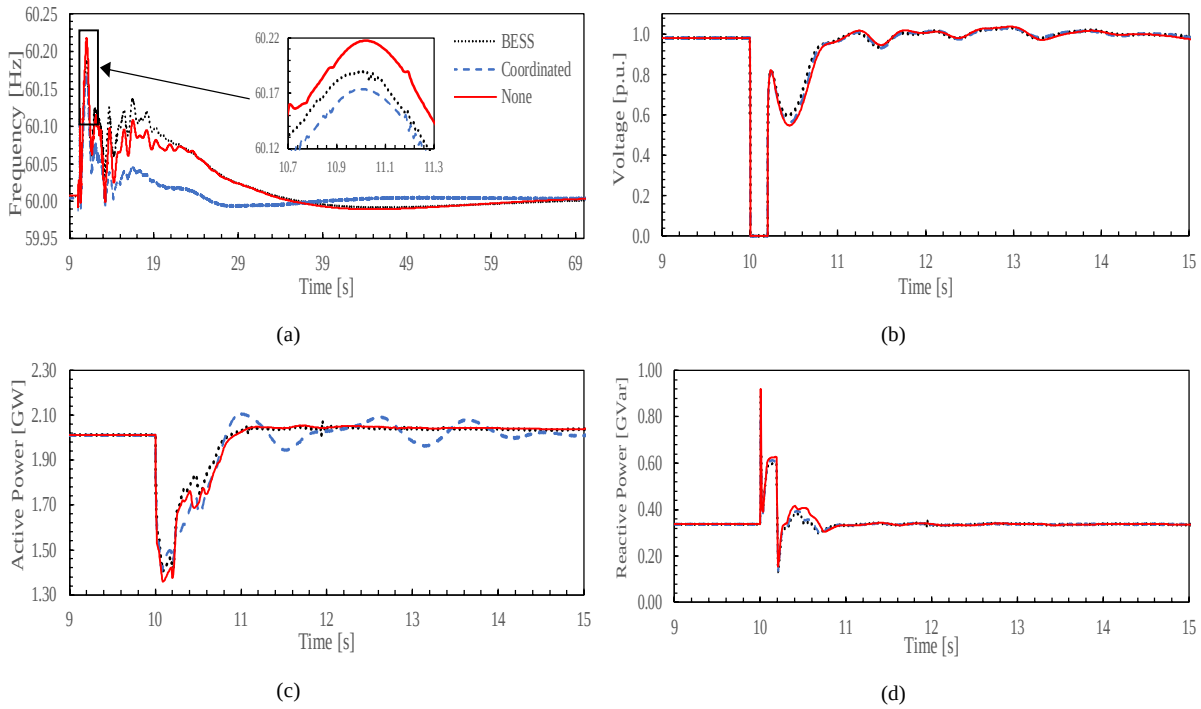

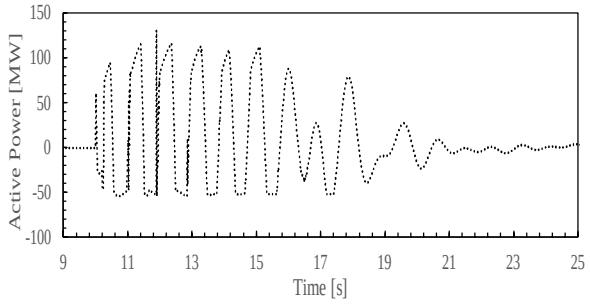

(e)

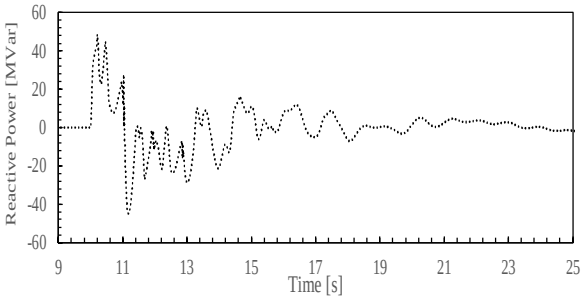

(f)

Figure 38. (a) Frequency (b) voltage at bus 31 (c) total active power of WFs (d) active power of BESS, (e) total reactive power of WFs and (f) reactive power of BESS. Results presented for three-phase short circuit case.

5.3 Summary

This chapter focuses on a frequency support scheme that exploits the coordinated use of RKC, the available dc-link capacitor energy, and deloading for the improvement of the IR and PFR that can be provided by a WT. The chapter refers to a DFIG turbine, but the main characteristics of the proposed approach can be adapted for other types of variable speed WTs. Two different networks representing systems with fast and slow dynamics are used to validate the performance of the individual and coordinated control schemes.

For networks with very fast dynamics, a relatively slower rotor speed PI controller ensures transient speed variation required for the IR provided by RKC and smooth rotor speed recovery afterwards. Higher gains adopted for the RKC scheme significantly raises the frequency nadir. For networks with very slow dynamics, a relatively fast rotor speed PI controller improves significantly the initial RoCoF but worsens the frequency nadir due to the slow picking up of the full demand by the synchronous generator units present in the network, before the RKC IR is cut off.

Slow acting regulations, such as the pitch angle control, have less effect on the frequency nadir when employed on networks with very fast dynamics. Possible solution is to employ fast acting power sources like supercapacitor storage, BESS, or flywheels. In networks with very slow dynamics, the pitch angle control has enough time to react, so to limit the RoCoF and improve frequency nadir.

The proposed coordinated control, irrespective of the grid dynamics, improves effectively not only the frequency response (RoCoF and frequency deviation) but also damps the frequency oscillations that follow typical perturbations, such as sudden load changes and faults.

Chapter 6. Participation of Wind Power Plants on Power System Small-Signal Stability

The concept of RES participation in power system stability has been mainly focused on improving frequency response as already described in chapter 3. Particularly, results presented in [20], [21], [23], [26], [27], [48], [73], [74] indicate that increasing IR support from RES always has a positive effect on the frequency response of the network. However, the stability of the power system is not assured without considering the impact of IR on the small-signal stability. While results presented in [15] only indicate the positive impact of IR on small-signal stability, findings in [80] indicate that IR may positively or negatively impact the system damping depending on the PI controller parameters of the phase-locked loop (PLL) used. Also, results presented in [81] indicate a trend of decreasing network small-signal stability when IR is introduced in the control scheme of DFIG WTs. Similarly, [82] concludes that network instability may occur with an improper setting of IR parameters and thus proposes prohibited regions of IR parameter settings to avoid the negative impact of IR control on the small-signal stability. In [83], a coordinated control parameter setting method of WF with IR control that satisfies frequency response and small-signal stability simultaneously is proposed.

In this chapter, the influence of IR services provided by WPPs on the small-signal stability of the Sicilian Island for the different DPs for the years 2030 and 2050 is presented. For the 2030 a controller adopting the proposed RKC and dc-link IR schemes to exploit the KE of the WT rotors and EE of supercapacitor units interfaced to the dc-link respectively is proposed and assessed to guarantee the small-signal stability of the future low-inertia power systems due to high-RES penetration: WPPs based on Full converter WTs (FCWT) are considered for this scope.

The first part of this chapter gives a theoretical overview of the small-signal stability concept. Subsequently, the small-signal stability of different DPs for the year 2030 and 2050 are analysed without support from WPPs. Finally, the contribution to small-signal stability provided by WPPs is investigated. Analysis is focused on electromechanical (EM) modes with damping ratio below 10 %, with those with a damping ratio below 5 % being the critical ones.

6.1 Theory: Modal Analysis

To perform the small-signal stability analysis, the classical modal/eigenvalue analysis tool, available in DIgSILENT, has been used. The modal analysis tool determines the state matrix using numerical algorithms and calculates its eigenvalues using a standard QR method. The idea is to write the matrix as a product of an orthogonal matrix and an upper triangular matrix, multiply the factors in the reverse order, and iterate.

An important role in power system small-signal stability analysis is played by the right eigenvectors of the state matrix. If the eigenvectors are normalized, then the i^{th} element of right eigenvector k, that is $w_k(i)$, determines the share of modal variable $z_k(t)$ in the activity of state variable $x_i(t)$ and it is usually referred to as observability or mode shape. The mode shape represents an inherent feature of a linear dynamic system and does not depend on where and how a disturbance is applied. Regarding electromechanical modes (i.e., modes involving swings of rotors generators), the generator speed mode shape is the key factor for determining the influence of individual oscillatory modes on swings of the rotors of individual generators.

Other important coefficients are the participation factors, obtained multiplying element by element left and right eigenvectors related to the same mode. Participation factors are a good measure of correlation between modes and state variables; they are typically used to determine the siting of stability enhancing devices (typically, PSSs). Generally, a stabilizer is preferably installed where the modal variables associated with a given eigenvalue are both well observable and controllable (i.e., the magnitude of the participation factor is large).

EM modes can be identified as those modes in which rotor angle deviation and rotor speed deviation have a large participation factor. These types of modes will be the primary focus of this report. However, only the magnitude of the participation factor carries relevant information. For this reason, it is useful to define the oscillation vector which is composed by the magnitude of the participation vector and the angle of the observability [84]. The magnitudes of the oscillation vectors capture the most influential participants. At the same time, the angles identify the groups of oscillating participants in a specific mode of interest, i.e., if the groups are in phase or counter-phase. The oscillation vector of state variable $x_i(t)$ with respect to mode k is defined as:

$$ov_{ki} = |pf_{ki}| \angle w_k(i) \qquad (0.65)$$

where pf_{ki} is the participation factor of state variable x_i in the k^{th} mode and w_k(i) is the i^{th} element of the observability vector k (i.e., the right eigenvector associated with mode k).

Using the modal analysis toolbox of DIgSILENT, small-signal stability analyses have been performed focusing on the EM modes with a damping ratio below 10% (being this value the conservative threshold). Damping ratios lower than 5% have been considered as the critical ones.

6.2 Networks Description: 2030 and 2050 Forecasted Networks

The network used is the portion of the Italian transmission grid corresponding to Sicily Figure 39; basic data have been provided by Terna and tailored for the dynamic simulations and analyses carried out by the ENSiEL consortium for the European OSMOSE project [85]. Regarding the grid configuration, Sicily presents few lines with a voltage higher or equal to 220 kV and, considering the geographic dimension and the high amount of generation capacity installed, they are poorly meshed. Since 2016, Sicily is connected to the Italian system through two ac interconnections at 400 kV, both starting from Rizziconi substation in the mainland and getting to the Sorgente substation on the Island. In particular, the interconnection activated in 2016 is composed by two parallel ac undersea cables. The 400 kV system (in red in Figure 39) essentially consists in a single backbone starting from the just mentioned link in the extreme North-East and ending in the Syracuse petrochemical nucleus in the south-eastern part of the region; it goes through the powerful interconnection substations of Sorgente, Paternò and Chiaramonte Gulfi up to the ISAB plants near Priolo Gargallo. Primary transmission system is made by a big 230 kV ring, extended along the coastal territories with a double circuit (in green in Figure 39).

Concerning the 2030 network, the following relevant changes have been applied:

- Power rating of the links with the mainland has been increased according to the available transfer capacity data for 2030 MW.
- A model of the external system is connected close to the continental terminal of the link Sicily-continental Italy to reasonable reproduce the dynamic behaviour of the rest of the Italian system.

- Twenty WFs (FCWT models), able to provide IR, has been assumed to be installed. Supercapacitors interfaced to the dc-links are designed to provide 10% of the WTs nominal power rating and are sized based on (0.46) for Δt=2s.
- Capacities of all generators have been upgraded according to provided data.
- No batteries have been considered since their installations is not expected in 2030.

As a first approximation, the model of the external system is represented by a generation unit rated power equals the sum of the active power of the synchronous machines of the other Italian market zones at the time frame considered, divided by a power factor (0.8), and starting time constant equal to 10 s. The equivalent machine represents only a portion of the generating units of the continental Italy able to provide primary frequency control. It is equipped with a governor, an automatic voltage regulator and a power system stabilizer properly tuned

Concerning the 2050 network, the relevant changes applied to the 2030 grid include:

- Power rating of the cables with the mainland have been increased to meet the available transfer capacity data provided of 2300 MW.
- Beside the wind plants already existing and equipped with a controller able to provide IR, another wind model (DFIG types), has been connected to the 230 kV system for an additional installation of 15 plants.
- As in 2050 installation of batteries has been nonzero, BESS units have been considered, installed either near each new wind plant or at the sites of the few SGs not decommissioned, with rated power of each battery/converter unit set equal to 20 % of the rating of the close-connected plant.
- Controlled loads, able to provide both frequency and voltage control, have been installed near 16 already existing loads considered large enough (at least 13 MW).
- The 220 kV ring circuit of the Island has been doubled to accommodate the demand expected for 2050.
- Capacities of all generators have been upgraded using the same approach of 2030.
- The equivalent model of the continental Italy has been updated as well.

The OSMOSE project and, in particular, the work package 1 [86], focused on the Optimal Mix of Flexibilities, and started with Task 1.1 by proposing long-term future scenarios for both 2030 and 2050, which differ on demand levels, installed capacities, investment opportunities, and the

amount of flexibility options. Within Task 2.2, static reserve adequacy analysis had been carried out, aiming to assess and validate these scenarios [87].

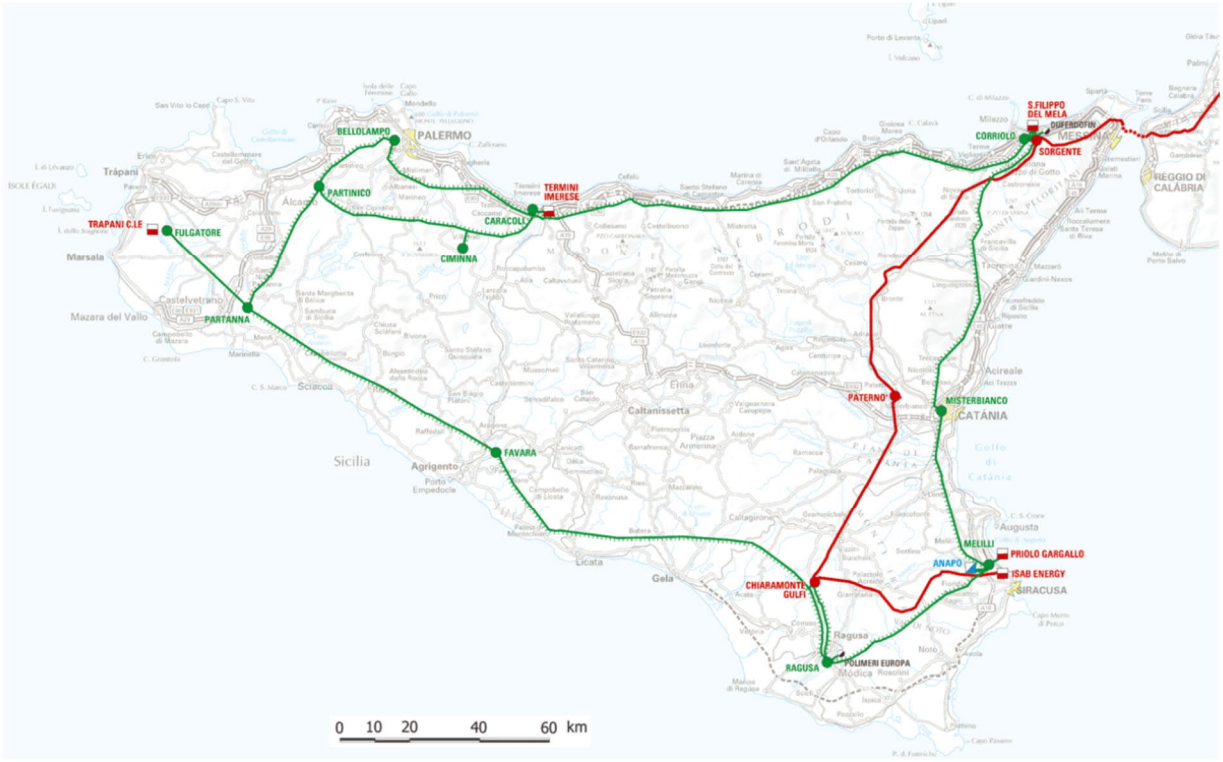

Figure 39. The Sicilian grid.

Utilizing the data generated from Task 1.1 and Task 1.2 as input, the impact of innovative flexibility sources (e.g., BESS and demand-side response) on power system stability has been evaluated. Tests have been done for 2030 and 2050 under the most typical and critical generation/demand conditions. Six significant DPs have been identified for both 2030 and 2050, considering the load demand, the generation technology mix, and the generation balance between traditional and renewable. The DPs considered in the stability analysis of 2030 network are:

- High Export (HE): represented by 22nd of March of Monte Carlo (MC) year 4 at 8.00 a.m., characterized by quite high PV, but low traditional generation production.
- High Import (HI): represented by 9th of April of MC 1 at 7:00 p.m., characterized by almost zero PV production and high load demand; such active power request is provided by rest of Italy.
- High Load (HL): represented by 19th of June of MC 1 at 9:00 a.m., characterized by high load demand; high PV, medium wind and low traditional generation production.

- Low Load (LL): represented by 21st of August of MC 1 at 2 a.m., characterized by low load and low generation by thermal plants, dispatched at their minimum active power, and medium wind production.
- Island: it is the High Load / Low Gas profile, with the link with the mainland out of service.
- Lines out of Service (LooS): it is the Low Load / Low Gas profile with the following 230 kV lines out of service: Favara_Chiaramonte and Caracoli_Sorgente.

Also, the DPs considered in the stability analysis of 2050 network are:

- HE: represented by 24th of May of MC 4 at 2:00 a.m., characterized by quite high wind production, no photovoltaic and low load demand.
- HI: represented by 11th of January of MC 1 at 1:00 a.m., characterized by almost no renewable production and medium/high demand.
- HL: represented by 27th of May of MC 1 at 4:00 p.m., characterized by high load demand, high wind and photovoltaic production.
- Island: represented by the 23rd of June of MC 5 at 3:00 p.m., with high photovoltaic and wind production and the link with the mainland out of service.
- LL: represented by the 4th of June of MC2 at 2:00 a.m., characterized by low load and almost zero wind production.
- LooS: it is the Low Load profile with the Favara_Chiaramonte and Caracoli_Sorgente 230 kV lines out of service.

In Figure 40a, the location of all the synchronous generators is shown; Figure 40b presents the location of all the FCWT WFs; Figure 40c presents the location of all the DFIG WFs; Figure 40d presents the locations of the DFIGs WFs, synchronous generators and the FCWT WFs substations. Since we will focus on EM modes, in Table 11 the 23 synchronous generators present in the Sicilian grid, their location, the rated power and the inertia constant are presented.

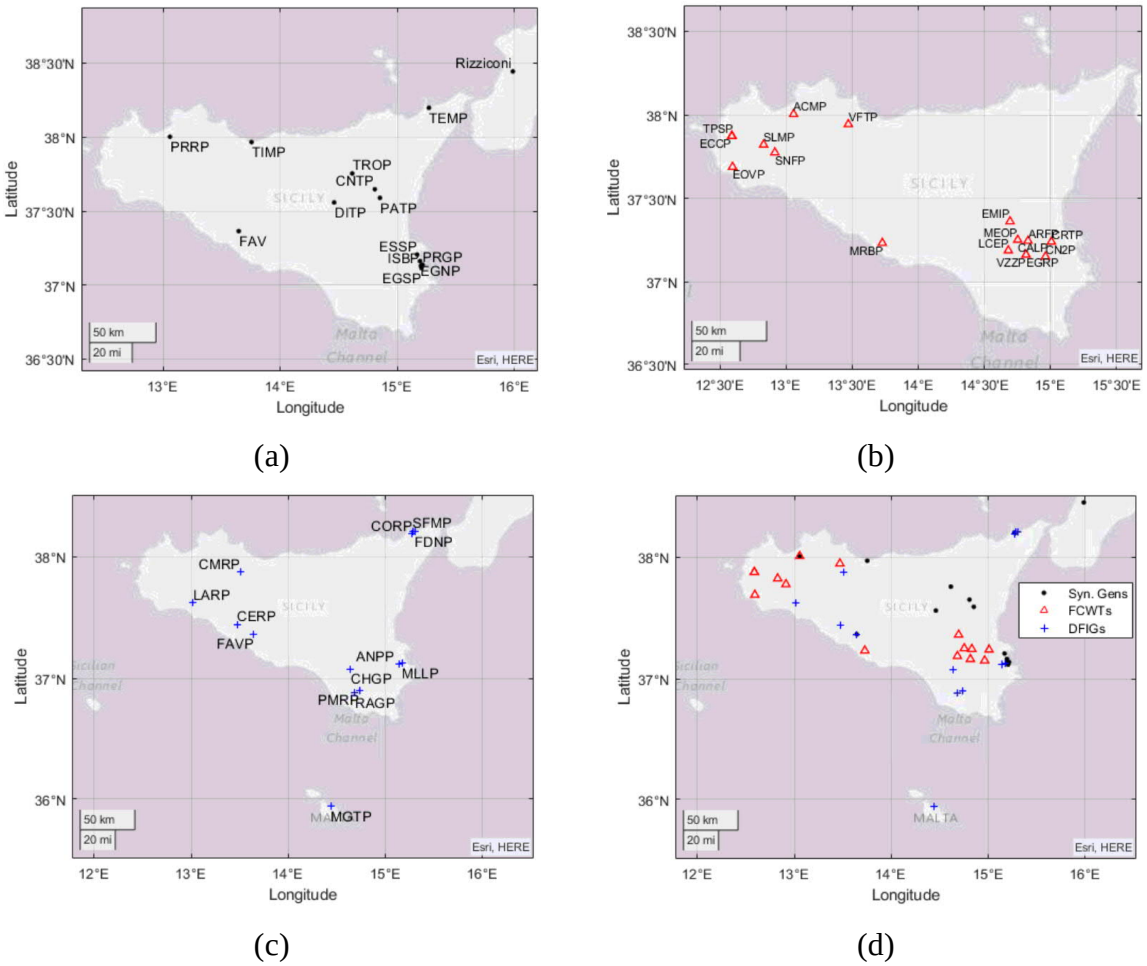

Figure 40. Locations of the (a) SGs, (b) FCWTs (c) DFIGs and (d) SGs, the FCWTs, and the DFIGs substations in the networks. The DFIGs are present only in the 2050 network. The slack generator is located on the peninsula in the substation in Rizziconi.

Table 11. List of synchronous generators in the Sicilian grid.

No.	Synchronous Generators	Location	Rating (MVA)	H (s)
1	CNTP	Catania	24	3.75
2	DITP	Enna	22.8	3.75
3	EGNP1	Siracusa	102	3.75
4	EGNP2	Siracusa	102	3.75
5	EGNP3	Siracusa	93.2	6
6	EGNP4	Siracusa	93.2	6
7	EGNP5	Siracusa	93.2	6
8	EGNP6	Siracusa	93.2	6
9	EGSP1	Siracusa	30	3.75
10	EGSP2	Siracusa	30	3.75
11	EGSP3	Siracusa	30	3.75
12	ESSP2	Siracusa	58.1	3.75
13	ESSP1	Siracusa	18.2	3.75
14	ISBP1	Siracusa	144	6
15	ISBP2	Siracusa	200	6
16	PATP	Catania	9	3.75
17	PRGP2	Siracusa	288	3.75
18	PRGP1	Siracusa	370	7.5
19	TEMP	Messina	185	3.75
20	TIMP3	Palermo	288	7.5
21	TIMP2	Palermo	288	7.5
22	TIMP1	Palermo	370	3.75
23	TROP	Enna	14	3.75

6.3 Modal Analysis: Base Cases

For the base case of the model without any IR control, the eigenvalues of the system state matric which shows the real and imaginary components, the frequency and damping ratio of each oscillatory mode and the associated dominant states are presented.

6.3.1 2030 network

The base case scenarios for the 2030 forecasted network are given as:

A. High export

The modal analysis revealed five EM modes with damping ratio below 10 % as shown in Table 12. Mode M1, that represents an inter-area mode, is the only mode with an unacceptable value of damping ratio below 5 %. Hence, this DP presents small-signal stability concerns.

Table 12. Electromechanical modes with damping ratio below 10% for the 2030 High Export dispatching profile.

Mode	Eigenvalues	Frequency, $f\ (Hz)$	Damping, ζ (%)	Involved Plants
M1	-0.07 ± 4.59j	0.73	1.48	TIMP, PRGP, SLACK
M2	-0.61 ± 8.18j	1.30	7.47	EGSP, PRGP
M3	-0.45 ± 5.58j	0.89	8.04	EGNP, PRGP, ISBP
M4	-0.88 ± 9.96j	1.58	8.84	EGSP
M5	-0.89 ± 9.95j	1.58	8.92	EGSP

The characteristics and the generators involved in M1-M5 are given below:

- M1: In Figure 41a, the oscillation vector of mode M1 is shown. The generators mainly affected by this oscillatory mode are the generators of the thermoelectric plant in Termini Imerese, named TIMP1 and TIMP2. It can also be noted that the mode is an inter-area mode (as the frequency suggests) in which the slack generator in Rizziconi oscillates against TIMP1, TIMP2 and the generator in Priolo Gargallo, named PRGP1. However, the participation factors of PRGP1 and of the slack are significantly lower.
- M2: In Figure 41b, the oscillation vector of mode M2 is shown. This is a local mode in which the generators EGSP1, EGSP2 and EGSP3 oscillate against the generators PRGP1 and PRGP2 which do however have a very low participation factor.
- M3: In Figure 41c, the oscillation vector of mode M3 is shown. This local mode is characterized by generators EGNP1 and EGNP2 oscillating against generators ISBP1 and PRGP1.

- M4: In Figure 41d, the oscillation vector of mode M4 is reported. This is an intra-plant mode in which EGSP3 oscillates against EGSP1 and EGSP2.
- M5: In Figure 41e, the oscillation vector of mode M5 is shown. This is another intra-plant mode of the same plant in which EGSP1 oscillates against EGSP2 and EGSP3.

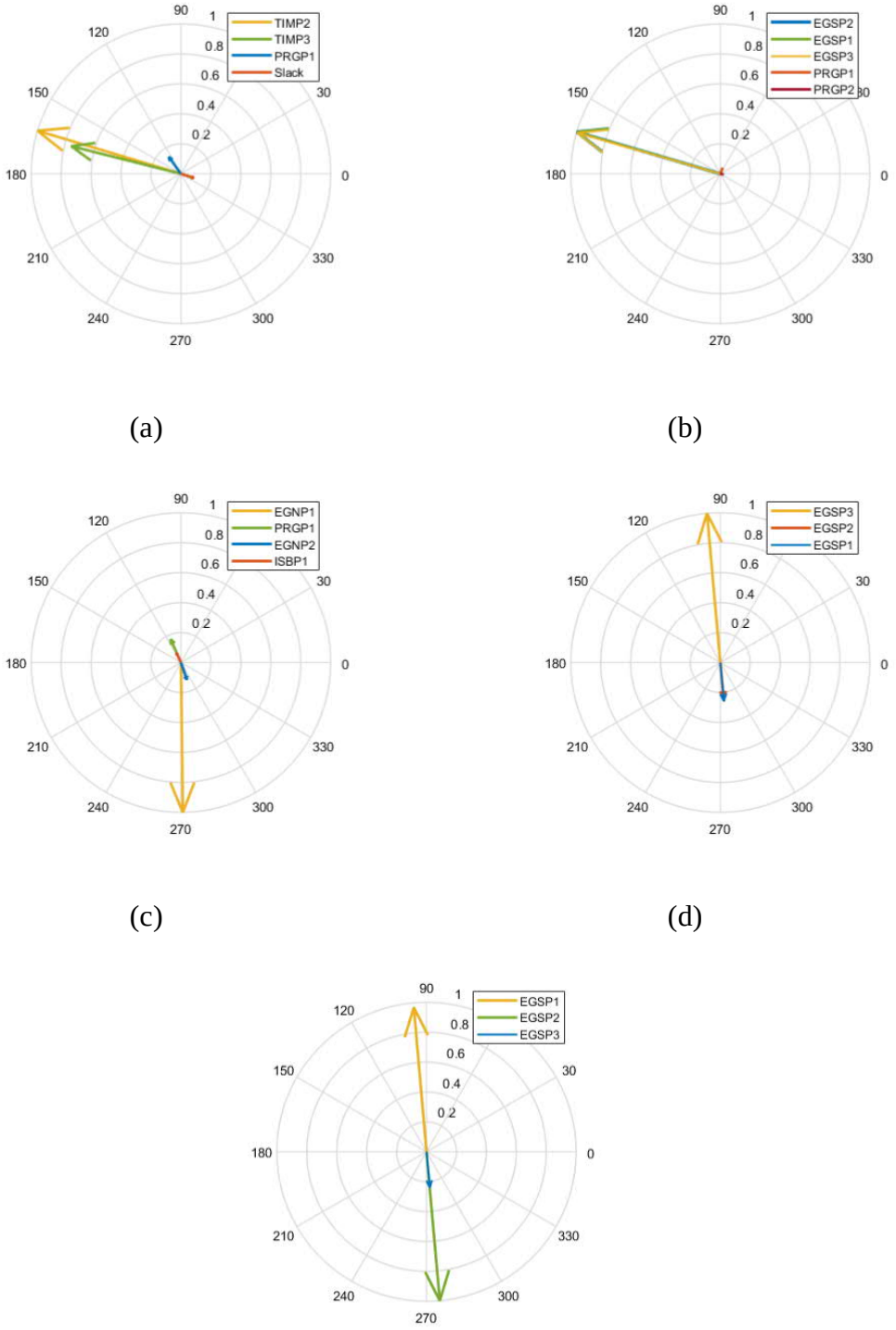

Figure 41. Oscillation vector of mode: (a) M1, (b) M2, (c) M3, (d) M4 and (e) M5.

B. High import

For the High Import DP, the modal analysis revealed M1 and M3 with a damping ratio below 10 % but above the 5 % threshold as shown in Table 13. Hence, this DP presents no small-signal stability concerns.

Table 13. Electromechanical modes with damping ratio below 10% for the 2030 High Import dispatching profile.

Mode	Eigenvalues	Frequency, $f\ (Hz)$	Damping, $\zeta\ (\%)$	Involved Plants
M1	-0.33 ± 4.25j	0.68	7.69	TIMPP, PRGP, SLACK
M3	-0.50 ± 5.56j	0.89	8.98	EGNP, PRGP, ISBP

C. High load

In the High Load DP, all EM modes have a damping ratio above 10 %. Hence, this DP presents no small-signal stability concerns.

D. Low load/ low gas

In the Low Load DP, all EM modes have a damping ratio above 10 %. Hence, this DP presents no small-signal stability concerns.

E. Island

In the Island DP, all EM modes have a damping ratio above 10 %. Hence, this DP presents no small-signal stability concerns.

F. Line out of service

In the Lines out of Service DP, all EM modes have a damping ratio above 10 %. Hence, this DP presents no small-signal stability concerns.

6.3.2 2050 network

The base case scenarios for the 2050 forecasted network are given as:

A. High export

In the High Export DP, all EM modes have a damping ratio above 10 %. Hence, this DP presents no small-signal stability concerns.

B. High import

For the High Import DP, the modal analysis revealed M1, M2, M4, M5 and M6 with a damping ratio below 10 % but above the 5 % threshold as shown in Table 14. Hence, this DP presents no small-signal stability concerns.

Table 14. Electromechanical modes with damping ratio below 10% for the 2050 High Import dispatching profile.

Mode	Eigenvalues	Frequency, $f\ (Hz)$	Damping, ζ (%)	Involved Units/Plants
M1	-0.31 ± 4.83j	0.77	6.41	TIMP, PRGP, SLACK
M2	-0.59 ± 8.18j	1.30	7.22	EGSP, PRGP
M4	-0.88 ± 9.98j	1.59	8.83	EGSP
M5	-0.89 ± 9.97j	1.59	8.90	EGSP
M6	-1.04 ± 10.4j	1.66	9.89	DITP, ESSP, PRGP

The characteristics and the generators involved in M6 are given below:

- M6: In Figure 42, the oscillation vector of mode M6 is shown. This is a local mode in which generator in Dittaino (DITP) and the generator in Augusta (ESSP2) oscillate against the larger generator located in Priolo Gargallo, PRGP1.

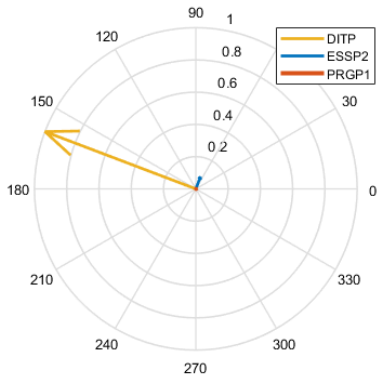

Figure 42. Oscillation vector of mode M6.

C. High load

In the High Load DP, all oscillatory modes have a damping ratio above 10 %; hence, it does not present any small-signal stability concern.

D. Low load/ low gas

For the Low Load DP, the modal analysis revealed M1, M7 and M8 with a damping ratio below 10 % but above the 5 % threshold as shown in Table 15. Hence, this DP presents no small-signal stability concerns.

Table 15. Electromechanical modes with damping ratio below 10% for the 2050 Low Load/ Low Gas dispatching profile.

Mode	Eigenvalues	Frequency, $f\ (Hz)$	Damping, ζ (%)	Involved Plants
M1	-0.23 ± 4.96j	0.79	4.65	TIMP, PRGP, SLACK
M7	-0.80 ± 10.89j	1.73	7.38	CNTP, PRGP
M8	-0.85 ± 11.09j	1.77	7.67	PATP, CNTP

The characteristics and the generators involved in M7 and M8 are given below:

- M7: In Figure 43a, the oscillation vector of mode M7 is shown. In this mode the generator in Contrasto (CNTP) oscillates against the unit in Priolo Gargallo (PRGP1).
- M8: In Figure 43b, the oscillation vector of mode M8 is shown. This mode involves the unit in Paternò (PATP) oscillating against the unit in Contrasto (CNTP).

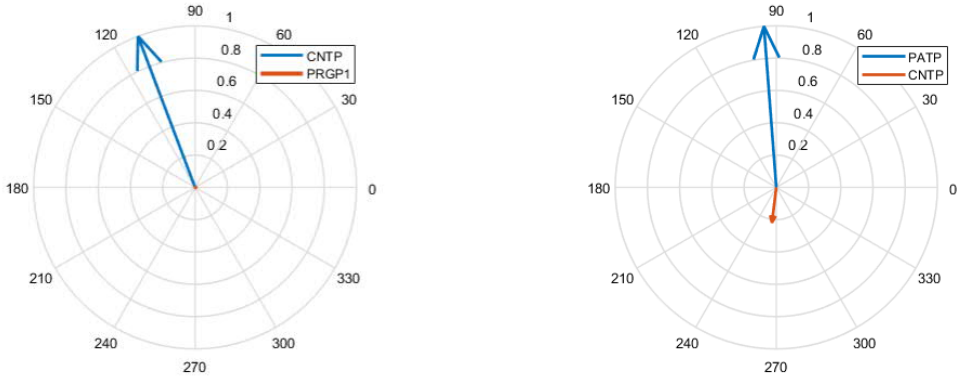

(a) (b)

Figure 43. Oscillation vector of mode (a) M7 and (b) M8.

E. Island

In the Island DP, all oscillatory modes have a damping ratio greater than 10 %; hence, it does not present any small-signal stability concerns.

F. Lines out of service

For the Line out of service DP, the modal analysis revealed M1, M7 and M8 with a damping ratio below 10 % but above the 5 % threshold as shown in Table 16. Hence, this DP presents no small-signal stability concerns.

Table 16. Electromechanical modes with a damping ratio below 10% for the 2050 Lines out of Service dispatching profile.

Mode	Eigenvalues	Frequency, f (Hz)	Damping, ζ (%)	Involved Plants
M1	-0.08 ± 4.74j	0.75	1.78	TIMP, PRGP, SLACK
M7	-0.86 ± 10.82j	1.72	7.95	CNTP, PRGP
M8	-0.92 ± 11.05j	1.76	8.26	PATP, CNTP

6.4 Influence of RES Contribution

In this section, the contribution of IR provision by WPPs to the small perturbation stability is evaluated. Among the considered DPs of the 2030 and 2050 forecasted networks, only the 2030 HE, 2030 HI, 2050 HI, 2050 LL, and 2050 LooS DPs present EM modes with damping ratio less than 10 % and hence will be investigated further. Also, the three modes M4, M5 and M8 are not sensitive to the contributions from the IR support and therefore will not be reported in the following discussion.

6.4.1 2030 network: coordinated synthetic inertia from FCWT

For the 2030 DPs, the IR provided by the FCWTs are considered. A modal analysis has been performed and repeated for different combinations of the FCWT IR controllers gain (i.e., K_{RKC} and K_{in_V}). For the 2030 HL, 2030 LL, 2050 LooS and 2030 Island, the variation in value of the IR gains does not introduce any mode with a damping ratio below 10 % hence the analysis will be focused on 2030 HE and 2030 HI DPs.

For the 2030 HE DP, the results are shown in Table 17. It can be observed that increasing either, or both, K_{in_V} and K_{RKC} above zero significantly improves the damping ratio of M1 above the 5% threshold, although for values of the gains too high (i.e., for K_{RKC} and K_{in_V} above 20) the damping ratio of M1 decreases. M2 and M3 experience a minor decrease in damping ratio with the increase of both the two gains.

For the 2030 HI DP, the results are presented in Table 18. The damping ratio of M1 increases, increasing either, or both, K_{in_V} and K_{RKC} above zero, from a value of 7.2% to a value of 13.6%. M3 experiences a minor decrease in damping ratio with the increase of the two gains.

Table 17. Influence of coordinated IR gain combinations on the modes of the High Export dispatching profile of 2030.

(K_{RKC}, K_{in_V})	M1		M2		M3	
	f (Hz)	ζ (%)	f (Hz)	ζ (%)	f (Hz)	ζ (%)
(0, 0)	0.73	1.48	1.30	7.47	0.89	8.04
(0,10)	0.73	6.75	1.31	7.20	0.89	7.65
(0,20)	0.75	7.33	1.31	7.14	0.89	7.39
(0,30)	0.76	6.47	1.31	7.12	0.89	7.28
(10, 0)	0.74	5.24	1.31	7.24	0.89	7.71
(20,0)	0.75	5.30	1.31	7.18	0.89	7.53
(30,0)	0.76	5.15	1.31	7.15	0.89	7.43
(10,10)	0.75	6.21	1.31	7.17	0.89	7.47
(20, 20)	0.77	5.56	1.31	7.13	0.89	7.31
(30,30)	0.77	4.93	1.31	7.11	0.89	7.25

Table 18. Influence of coordinated IR gain combinations on the modes of the High Import dispatching profile of 2030.

(K_{RKC}, K_{in_V})	M1		M3	
	f (Hz)	ζ (%)	f (Hz)	ζ (%)
(0, 0)	0.68	7.69	0.89	8.98
(0,10)	0.74	13.6	0.89	8.81
(0,20)	0.74	13.6	0.89	8.62
(0,30)	0.74	13.7	0.89	8.55
(10, 0)	0.74	13.6	0.89	8.83
(20,0)	0.74	13.6	0.89	8.71
(30,0)	0.74	13.6	0.89	8.64
(10,10)	0.74	13.6	0.89	8.67
(20, 20)	0.74	13.6	0.89	8.56
(30,30)	0.74	13.6	0.89	8.53

6.4.2 2050 network: coordinated synthetic inertia from FCWT and BESS

For the 2050 DPs, the IR provided by the FCWTs and BESS are analysed individually and then their combined effect is investigated. The modal analysis has been performed and repeated for different combinations of the BESS IR controllers (i.e., K_I) and FCWT gain (i.e., K_{RKC} and K_{in_V}). For the 2050 HE, 2050 HL and 2050 Island DPs, the variation in value of the gains of the does not introduce any mode with a damping ratio below 10 % hence the analysis will be focused on 2050 HI, 2050 LL, and 2050 LooS DPs.

For the 2050 HI DP, the results are shown in Table 19. It can be observed that increasing either, or both, K_{in_V} and K_{RKC} above zero improves the damping ratio of M1, however for (K_{RKC}, K_{in_V}) above (10,10) the damping ratio of M1 starts to decrease. M2 and M6 experience a minor decrease in damping ratio with the increase of either, or both, the two gains. Regarding K_I, high

values produce minor effect on modes M1, while the damping ratios of modes M2 and M6 are significantly improved with that of M6 above the threshold of 10 %. The combined effect of all the IR gains produces major improvements in the damping ratios of all the modes.

For the 2050 LL DP, the results are presented in Table 20. Similarly, increasing either, or both, K_{in_V} and K_{RKC} above zero improves the damping ratio M1 above the 5% threshold; however, it decreases for high values of the gains (e.g., above (K_{RKC}, K_{in_V}) of (10,10)). M7 experienced a minor decrease in damping ratio with increasing values of both the gain values. Regarding K_I, higher values provide a minor improvement in the damping of mode M1, and no effect on M7. The combined effect of all the IR gains produces major improvements in the damping ratio of M1.

For the 2050 LooS DP, the results are reported in Table 21. Increasing either, or both, K_{in_V} and K_{RKC} above zero significantly improves the poorly damped M1 above the 5% threshold. However, the damping ratio of M1 starts to decrease for high gain values (e.g., above (K_{RKC}, K_{in_V}) of (10,10)). M7 experiences a minor decrease in damping ratio with increasing values of both the gain values. Regarding K_I, higher values provide a minor improvement in the damping of mode M1, and no effect on M7. The combined effect of all the IR gains produces major improvements in the damping ratio of M1.

Table 19. Influence of coordinated IR gain combinations on the modes of the High Import dispatching profile of 2050.

(K_I, K_{RKC}, K_{in_V})	M1		M2		M6	
	f (Hz)	ζ (%)	f (Hz)	ζ (%)	f (Hz)	ζ (%)
(0, 0, 0)	0.77	6.41	1.30	7.22	1.66	9.89
(0, 0,10)	0.77	8.21	1.31	7.04	1.67	9.62
(0, 0, 20)	0.78	8.05	1.31	6.98	1.67	9.60
(0, 0, 30)	0.78	7.97	1.31	6.96	1.67	9.59
(0, 10, 0)	0.77	7.48	1.31	7.05	1.66	9.43
(0, 20, 0)	0.78	7.70	1.31	7.00	1.69	9.12
(0, 30, 0)	0.78	7.61	1.31	6.98	1.69	9.00
(10, 0, 0)	0.77	6.42	1.30	7.88	1.66	10.2
(20, 0, 0)	0.77	6.43	1.30	8.57	1.66	10.4
(30, 0, 0)	0.77	6.44	1.30	9.27	1.67	10.7
(10, 10, 10)	0.78	7.97	1.30	7.66	1.67	9.89
(20, 20, 20)	0.78	7.57	1.30	8.29	1.67	10.1
(30, 30, 30)	0.79	7.19	1.30	8.98	1.67	10.3

Table 20. Influence of coordinated IR gain combinations on the modes of the Low Load dispatching profile of 2050.

(K_I, K_{RKC}, K_{in_V})	M1		M7	
	f (Hz)	ζ (%)	f (Hz)	ζ (%)
(0, 0, 0)	0.79	4.65	1.73	7.38
(0, 0,10)	0.79	5.77	1.73	7.26
(0, 0, 20)	0.79	6.12	1.73	7.25
(0, 0, 30)	0.80	6.11	1.73	7.24
(0, 10, 0)	0.79	5.35	1.73	7.32
(0, 20, 0)	0.79	5.70	1.73	7.29
(0, 30, 0)	0.80	5.76	1.73	7.27
(10, 0, 0)	0.79	4.66	1.73	7.38
(20, 0, 0)	0.79	4.67	1.73	7.38
(30, 0, 0)	0.79	4.67	1.73	7.38
(10, 10, 10)	0.79	5.97	1.73	7.25
(20, 20, 20)	0.80	5.87	1.73	7.24
(30, 30, 30)	0.80	5.64	1.73	7.24

Table 21. Influence of coordinated IR gain combinations on the modes of the Line out of Service dispatching profile of 2050.

(K_I, K_{RKC}, K_{in_V})	M1		M7	
	f (Hz)	ζ (%)	f (Hz)	ζ (%)
(0, 0, 0)	0.75	1.78	1.72	7.95
(0, 0,10)	0.76	7.39	1.73	7.84
(0, 0, 20)	0.79	6.09	1.73	7.83
(0, 0, 30)	0.79	5.38	1.73	7.82
(0, 10, 0)	0.76	4.75	1.73	7.92
(0, 20, 0)	0.78	5.34	1.73	7.88
(0, 30, 0)	0.78	4.98	1.73	7.86
(10, 0, 0)	0.75	1.81	1.72	7.95
(20, 0, 0)	0.75	1.83	1.72	7.95
(30, 0, 0)	0.75	1.86	1.72	7.95
(10, 10, 10)	0.78	6.03	1.73	7.84
(20, 20, 20)	0.79	5.22	1.73	7.83
(30, 30, 30)	0.80	4.05	1.73	7.82

6.5 Dynamic Simulation: Loss of Lines of 2030 High Export DP

By just looking at the modal analysis results, it could be concluded that the best damping for all the DPs is obtained with the combination (K_{RKC}, K_{in_V}) equal to (0,20), i.e., given only by the dc-link IR support. This sub-section aims to compare the small-signal stability performances of the individual IR schemes and their combined action via time domain simulations. The initial generator speed deviation and steady state speed damping are used as performance indicators.

However, to correctly assess the stability of a power system, it is also fundamental to analyse both frequency response and small-signal stability. Concerning frequency response (discussed in Chapter 5), the effects of the combined support from the dc-link and RKC schemes have already been validated to provide a better improvement in terms of maximum frequency deviation and initial rate of change of frequency compared to when only one of the schemes is employed.

A non-linear dynamic simulation is carried out considering the 2030 HE DP. Under this operating condition, Sicily exports 750 MW of active power towards continental Italy via the three transmission lines (Lines 1, 2 and 3), where each line is exporting 250 MW. During the simulation, a disturbance is initiated by the loss of two of the three interconnections with continental Italy (Lines 1 and 2) at the time of 1s to excite the inter-area mode M1. The results are presented for the network (a) without any IR support with (K_{RKC}, K_{in_V}) = (0, 0), (b) with dc-link IR support with (K_{RKC}, K_{in_V}) = (0, 20), (c) with RKC IR support with (K_{RKC}, K_{in_V}) = (20, 0) and (d) with coordinated IR support with (K_{RKC}, K_{in_V}) = (20, 20). These values are considered as they maintain the damping ratios of all the EM modes above the 5% threshold.

In Figure 44a, the speed of synchronous generator ‘TIMPP 2’ (which has the highest participation factor in mode M1) is shown. The case without any IR support presents the highest initial generator speed zenith. Moreover, without IR support, the speed oscillations are poorly damped. With the introduction of either of the IR control schemes, the speed oscillations are properly damped. In terms of initial speed zenith, the best results are obtained with the coordinated control.

The WF active power outputs are shown in Figure 44c. Without any IR support, the WFs maintain their output power constant, even during the transient, and do not participate in frequency support. With the IR support schemes, the WFs initially reduce their output in response to Sicily's initial increase in frequency. The low-frequency oscillation of ‘TIMPP 2’ is damped with the active powers of the WFs controlled in the opposite direction to the frequency change in the Sicilian network.

Figure 44d and 34e show the power exchanged through Lines 1 and 3, respectively, for the four considered case studies. Immediately after the event, the power exported by the lost connections (Lines 1 and 2) is entirely exported by Line 3. The initial rise in generated power due to the loss of the two lines increases the Sicilian network frequency. The frequency returns to the nominal value of 1 p.u. at the end of the transient, thanks to the damping effect of the IR provision.

In conclusion, the coordinated control should be preferred to the “dc-link support IR only”, as it provides better results in terms of frequency response, maintaining the damping ratios above the 5% threshold for all the EM modes.

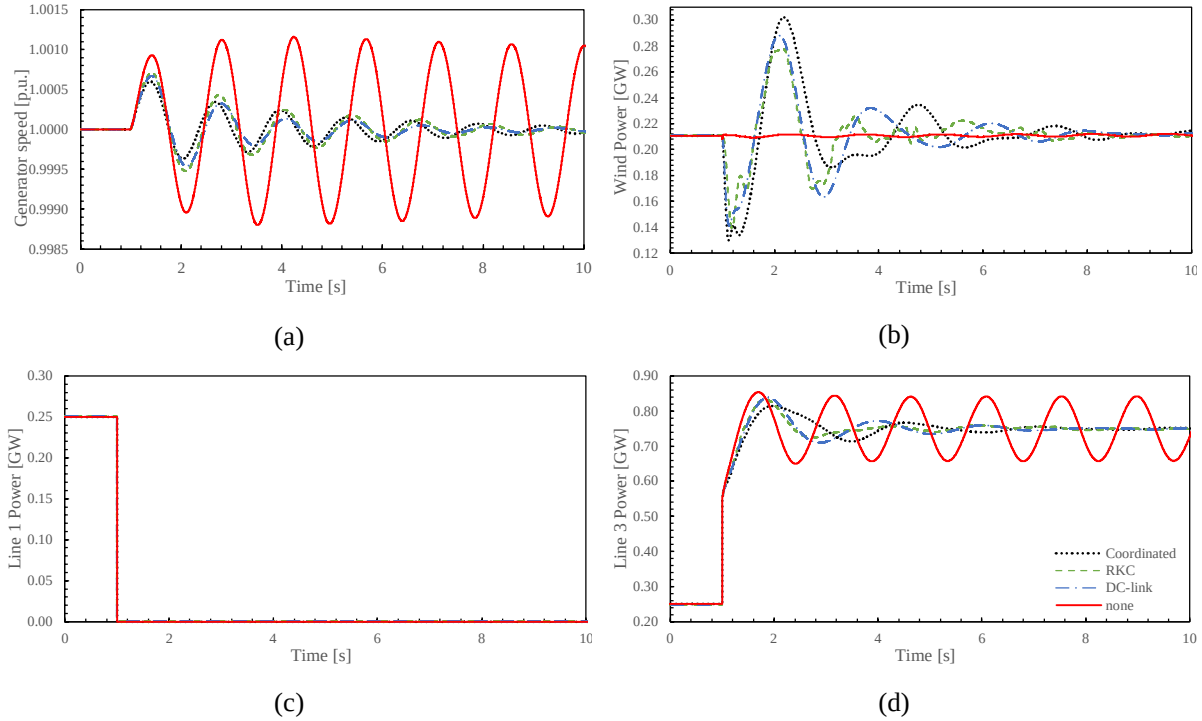

Figure 44. (a) Speed of SG ‘TIMPP 2’, (b) total active power of WFs, (c) power exported through line 1 and (d) power exported through line 3. Results presented for 2030 HE DP.

6.6 Summary

In this chapter, the impact of IR provision by wind power plants on power system small-signal stability is studied on the Sicilian grid in some significant scenarios forecasted for the years 2030 and 2050. Regarding the stability of the system to small perturbations, the simulations performed on the developed models allow concluding that the system present major stability concerns for some considered DPs. For both the forecasted networks, the 2030 HE, 2050 LL and 2050 LooS DPs are the only ones presenting in the base conditions (without IR support from WPPs) a not properly damped oscillatory mode. That mode is inter-area, involving the equivalent generator in Calabria and the power plant near Termini Imerese, and its stability can be improved thanks to the IR contribution provided by the WPPs. The 2030 HI and 2050 HI DPs present, respectively, two and three EM modes with damping ratio above 5 % and below 10 %, thus well damped. All the other DPs, 2030 HL, 2030 LL, 2030 Island, 2030 LooS, 2050 HE, 2050 HL and 2050 Island do not show any mode with a damping ratio below the conservative threshold of 10 %.

The IR support schemes adopted include: (a) for the 2030 network, the coordinated use of both the dc-link IR scheme and the RKC IR scheme. (b) for the 2050 network, the coordinated use of the dc-link IR scheme, the RKC IR scheme and IR provision by BESS units installed close to the WPPs. The chapter refers to a FCWT WPPs, but the main characteristics of the proposed approach can be adapted for other types of VSWTs. A sensitivity analysis of the EM modes with respect to the IR gain has been performed. The results show how the stability of poorly damped modes improves introducing the contribution of IR. The main conclusions drawn from the analyses performed are:

- Among the considered DPs, the 2030 HE, 2050 LL and 2050 LooS DPs present instability conditions that have been detailed in the paper, and that highlight how the IR support could improve the small-signal stability of the network.
- Unlike frequency response, where increasing inertia always provides a positive impact, very large inertia may have negative impact on the small-signal stability of the network, and such an effect has been quantified. From the results presented, it was observed while increasing the gains of the IR schemes improved the damping ratio of some modes, other modes experience a reduction in damping ratio. Also, for the modes that do benefit from the introduction of IR support, it can be observed that for values of the gains that are too high, the damping ratios of the modes start to decrease. Therefore, to achieve good frequency response and small-signal stability, a trade-off is necessary. IR control schemes are needed (achieved by the coordination of the RKC, dc-link support schemes and BESS IR), but the values of the two gains need to be carefully selected. In this way, initial network frequency nadir/zenith is limited while at the same time, the small-signal stability is granted by having all the damping ratios of the electromechanical modes above the required threshold of 5%.

In conclusion, the proposed coordinated control seems to effectively improve the damping of generator speed oscillations following the most common faults that a network may experience.

Chapter 7. Conclusion Remarks

This thesis focused on large integration of wind power in the power system and on developing control algorithm that enables variable speed wind turbines, VSWT, power plants to contribute to power system stability improvement, with focus on enhanced frequency control and small-signal stability.

The second chapter of this thesis has been devoted to the problem of power system frequency control and the possibility of wind power plants, WPPS, aiding in inertial response, IR, and primary frequency response, PFR, services. Mathematical derivations and parameter sensitivity analysis have been presented to detail how employing fast reserves with PFR and/or IR based control can mitigates the impacts of both frequency deviation and rate of change of frequency, RoCoF, of the power network during power imbalances.

The third chapter focuses on VSWT modelling and the frequency support techniques.
Since IR requires short term power provision, additional controllers that exploits both the electrostatic energy, EE, stored in the dc-link capacitors and kinetic energy, KE, stored in rotor (using the rotor kinetic energy control, RKC, IR scheme) have been developed. Under the dc-link IR scheme, two major architectures (i.e., current-controlled mode, CCM, and voltage-controlled mode, VCM) usually found in the literature are first identified, implemented in the simulation environment, and compared. In both architectures, the active power released from the capacitors are related to the grid frequency via a derivative relationship. Detailed analysis of the dc-link voltage limits for IR provision has been provided and protection schemes that aim to keep the dc voltage in the required limits for the proper operation of the grid-side converter, GSC, are duly proposed. From the analysis, it has been shown that the in steady state operation, the minimum dc voltage required to meet pulse width modulation requirements is mainly affected by the transferred reactive power, while the transferred active power effect is negligible. In dynamic conditions, the minimum required dc voltage is more sensitive to the transferred active power changes rather than the transferred reactive power. The maximum allowable voltage has been indicated to be determined by the voltage ratings of active and passive components of the GSC unit. Finally, a procedure for sizing dc-link capacitors for the IR provision is given.

Chapter 7. Conclusion Remarks

The RKC IR scheme used for exploiting the KE of the wind turbines, WTs, rotating mass has been developed. The proposed control acts directly on the active power reference by adding an addition signal which consists of both frequency derivative and frequency deviation proportional components. The IR coefficient derived depends on several factors, including of the pre-disturbance rotor speed and WT natural inertia. Also, proposals involving the right selection of rotor speed controller proportional-integral gains have been presented; this is to ensure transient speed variation for the RKC support and fast rotor speed recovery afterwards.
On the other hand, PFR requires long-term power provision which is achieved in this work by operating the WTs at non-optimal operating conditions, a method known as deloading. The proposed control for the PFR does not directly act on the active power reference but on adjusting the rotor speed set-point and the pitch angle directly in response to the frequency deviation. The deloading scheme presented adopts a combination of both over-speed deloading and pitch deloading at different wind speed levels as follows: over-speed deloading is adopted at the low-speed regime, a coordinated use of both over-speed and pitch deloading is adopted at the medium-speed regime, and pitch deloading is adopted at the high-speed regime. The possibility of using external storage systems, ESS, to provide both IR and PFR has been discussed.
Different ESS technologies, along with their potential locations and control strategies have been analysed. A detailed description of a battery energy storage system, BESS, unit controlled in the grid-supporting mode (adopted in Section 2.2, Chapter 5 and Chapter 6) has been presented. In the grid-supporting control mode considered, additional power reference consisting of both frequency deviation and frequency derivative components is added to the active power reference signal.

The fourth chapter first validates the CCM and VCM DC-link IR architectures using detailed simulations. Presented results show that, with the same value of IR coefficient realised, the response time of the VCM architecture is lower than that of the CCM architecture when the same frequency disturbance is applied. In terms of IR active power and energy, the VCM architecture releases higher values as compared to the CCM architecture. In case of a permanent steady-state network frequency disturbance, the VCM results in the dc voltage converging to a non-nominal steady state value whereas for the CCM architecture, the dc voltage recovers its initial state.
The chapter also highlights the possible coordination between either of the two dc-link IR architectures and the RKC IR scheme. The analysis is presented by means of frequency response and modal analysis. Due to the slow response of the dc-link voltage controller adopted

in the CCM strategy, any transient increase in power from the rotor-side converter, RSC, side leads to an increase in the dc voltage instead of increase in dc current or active power flow to the network. In this way, transient active power increase from the RSC, as a result of either the RKC IR or PFR scheme achieved through deloading, is unable to be delivered to the network during network disturbance required to support small-signal stability or the frequency response. However, for the VCM architecture, the fast response of the dc-link voltage controller maintains a fixed dc voltage required to deliver transient active power increase from the RSC to the network in support of network stability.

The fifth chapter focuses on frequency response improvement by WPPS. Particularly, two different networks representing grids with either fast or slow dynamics are employed for the analysis to ascertain how the individual frequency support schemes and their combined effect affect different kind of networks. Parameters that are considered in the networks modelling include inertia, droop coefficient, damping ratio, time constants, generation capacity, load disturbance etc. For the fast dynamics network, the system is characterized by very low inertia and with units equipped with fast acting governors such as hydro turbine governors. The fast-acting governors reacts in a short time frame to arrest the fast network frequency decline after a perturbation. A single bus model with a SG equipped with a hydro turbine governor has been adopted to represent the fast dynamics network. For the slow dynamics network, the system is characterized by very large inertia and with units equipped with slow acting governors such as steam turbine governors. The slow-acting governors takes a longer time to fully react to restore the network frequency to a new steady-state value after a perturbation. A modified version of the New England 10-machine 39-bus network, which represents a simplified model of the transmission system in New England area, USA has been employed for such a system. For different network disturbances, such as active load power steps and three-phase short circuit faults, wind conditions (low wind speed, medium wind speed and high wind speed ranges) and total available reserved power obtained by deloading the WPPs, the performance of the support schemes and the proposed coordinated one are compared. For the slow dynamics network, the possibility of employing a large-scale centralized BESS unit is presented and the performance compared to the proposed schemes of the WPPs.

It is observed that employing only the RKC IR scheme may either have a positive or negative impact on system frequency nadir based on the dynamics of the network and the WTs rotor speed recovery times. During speed recovery, the turbine absorbs energy which leads to a period of under-production (with output power lower than the pre-disturbance value) in the WT output

power; this may be detrimental especially if the speed recovery occurs while the conventional generators have not increased their output enough to arrest the frequency decline, which is the case of networks with slow dynamics. In this way, the speed-recovery process contributes to the frequency drop and this effect further disintegrates the network frequency response (achieving even lower nadirs). However, for fast dynamics networks, the fast response of the conventional generators in the network allows the WTs to contribute to arresting the frequency decline before their speed recovery processes take place. A smooth speed-recovery follows after the frequency has passed the nadir; in this way, the speed recovery does not contribute negatively to the frequency nadir.

Also, for networks with fast dynamics, it has been observed that the response time of the storage unit providing frequency support services is critical. For example, employing slow acting regulations, such as the pitch angle control provides less effect on the frequency nadir since the pitch angle control does not have enough time to react to arrest the fast-dropping frequency. For this reason, fast acting power sources like supercapacitor storage, BESS, or flywheels have been suggested for such networks.

For all the considered operating conditions of the WPPs and different network faults simulated, the proposed coordinated control has provided the best improvement in the network frequency response, irrespective of the grid dynamics.

The sixth chapter focuses on small-signal stability improvement by WPPS. The network adopted in this chapter is a portion of the Italian transmission grid (representing the Sicilian grid) where the most recent and innovative flexibility services have been implemented to preserve the dynamic stability for the scenarios selected within the OSMOSE European project. The most typical and critical generation/demand conditions, referred to as dispatching profiles, DPs, have been recreated on the Sicilian grid for 2030 and 2050, which represent two target years for the European Union objectives concerning climate/carbon neutrality. The DPs that have been considered consists of the high export, HE, the high import, HI, the high load, HL, the low load, LL, the Island and the lines out of service, LooS. Using the modal analysis tool present in DIgSILENT software, small-signal stability analyses have been performed focusing on the electro-mechanical, EM, modes with a damping ratio below 10% (being this value the conservative threshold) and lower than 5% considered as the critical ones.

For the considered DPs of the 2030 network, the installation of 20 wind farms, WFs, capable of providing IR services has been considered. On the IR provision, supercapacitor units sized to provide 10% of the WTs nominal power rating are interfaced to the WTs dc-links and are

utilized for the dc-link IR while the rotor KE of the individual WTs has been utilized for the RKC IR support. In addition to the 20 WFs of the 2030 network, the installation of BESS units, capable of providing IR, either near each new WFs or at the sites of the few synchronous generators, SGs, not decommissioned have been considered. The rated power of each BESS unit has been set equal to 20 % of the rating of the close-connected plant.

In the Base cases without any IR support, modal analysis indicated that only the 2030 HE, 2050 LL and 2050 LooS DPs are the only ones presenting a not properly damped EM mode represented in this work as M1. The 2030 HI and 2050 HI DPs present, respectively, two and three EM modes with damping ratio above 5 % and below 10 %, thus well damped. All the other DPs, 2030 HL, 2030 LL, 2030 Island, 2030 LooS, 2050 HE, 2050 HL and 2050 Island do not show any mode with a damping ratio below the conservative threshold of 10 %. Oscillation vectors have been shown for each EM to determine the magnitude and angle of participation of the speed of influential SGs in the EM of interest. From the oscillation vector of M1, it involves the equivalent generator in Calabria and the power plant near Termini Imerese.

The effect of IR provision on the EM have been presented by means of modal analysis and dynamic simulations. For the 2030 network, the coordinated use of both the dc-link IR scheme and the RKC IR scheme has been proposed whereas for the 2050 network, the coordinated use of the dc-link IR scheme, the RKC IR scheme and IR provision by BESS units has been proposed. For an optimal coordinated IR gain combination, i.e., (K_{RKC}, K_{in_V}) = (20, 20) for the 2030 network and (K_I, K_{RKC}, K_{in_V}) = (20, 20, 20) for the 2050 network, all the EM modes achieve a damping ratio of above the 5% critical threshold while few others go above the 10% conservative limit.

Combining the results presented in both Chapter 5 and Chapter 6, it can be concluded that, the proposed coordinated controllers provide the best overall improvement in power system stability (in this work both frequency response and small-signal stability) as compared to when the individual support schemes are employed during network disturbances

.

Bibliography

[1] P. Kundur, J. Paserba, V. Ajjarapu, G. Andersson, A. Bose, C. Canizares, N. Hatziargyriou, D. Hill, A. Stankovic, C. Taylor, T. Van Cutsem, and V. Vittal, "Definition and Classification of Power System Stability," vol. 19, no. 2, pp. 1387–1401, 2004.

[2] N. Hatziargyriou, J. Milanovic, C. Rahmann, V. Ajjarapu, C. Canizares, I. Erlich, D. Hill, I. Hiskens, I. Kamwa, B. Pal, P. Pourbeik, J. Sanchez-Gasca, A. Stankovic, T. Van Cutsem, V. Vittal, and C. Vournas, "Definition and Classification of Power System Stability - Revisited & Extended," *IEEE Trans. Power Syst.*, vol. 36, no. 4, pp. 3271–3281, 2021.

[3] International Renewable Energy Agency, "Renewable capacity statistics 2021 Statistiques de capacité renouvelable 2021 Estadísticas de capacidad renovable 2021," pp. 1–300, 2021.

[4] Global Wind Energy Council, "GWEC | GLOBAL WIND REPORT 2021," 2021.

[5] International Energy Agency, "Renewables 2020 Analysis and Forecast to 2025," 2020.

[6] J. Kabouris and N. Hatziargyriou, "Wind Power in Greece – Current Situation , Future Developments and Prospects," pp. 1–8, 2010.

[7] J. Kabouris and F. D. Kanellos, "Impacts of Large-Scale Wind Penetration on Designing and Operation of Electric Power Systems," vol. 1, no. 2, pp. 107–114, 2010.

[8] A. Chakraborty, "Advancements in power electronics and drives in interface with growing renewable energy resources," *Renew. Sustain. Energy Rev.*, vol. 15, no. 4, pp. 1816–1827, 2011.

[9] L. Xiong, X. Liu, Y. Liu, and F. Zhuo, "Modeling and stability issues of voltage-source converter dominated power systems: A review," *CSEE J. Power Energy Syst.*, pp. 1–18, 2020.

[10] Z. Wu, W. Gao, T. Gao, W. Yan, H. Zhang, S. Yan, and X. Wang, "State-of-the-art review on frequency response of wind power plants in power systems," *J. Mod. Power Syst. Clean Energy*, vol. 6, no. 1, pp. 1–16, Jan. 2018.

[11] I. S. Naser, A. Garba, O. Anaya-Lara, and K. L. Lo, "Voltage Stability of Transmission Network with Different Penetration Levels of Wind Generation," *Univ. Power Eng. Conf. (UPEC), 2010 45th Int. IEEE*, pp. 1–5, 2010.

[12] L. Meegahapola, S. Member, and D. Flynn, "Impact on Transient and Frequency Stability for a Power System at Very High Wind Penetration," *Power Energy Soc. Gen. Meet. 2010*, pp. 1–8, 2010.

[13] S. Impram, S. Varbak, and B. Oral, "Challenges of renewable energy penetration on power system flexibility : A survey," *Energy Strateg. Rev.*, vol. 31, no. April, p. 100539, 2020.

[14] L. Meegahapola and D. Flynn, "Transient Stability Analysis of a Power System with High Wind Penetration."

[15] J. A. Adu, F. Napolitano, J. D. R. Penaloza, T. Pontecorvo, and F. Tossani, "Influence of Fast Frequency Response Services in DFIG-Based Wind Power Plants on Power Grids Stability," *Proc. - 2020 IEEE Int. Conf. Environ. Electr. Eng. 2020 IEEE Ind. Commer. Power Syst. Eur. EEEIC / I CPS Eur. 2020*, pp. 18–23, 2020.

[16] N. Modi, S. Member, T. K. Saha, S. Member, and N. Mithulananthan, "Effect of Wind Farms with Doubly Fed Induction Generators on Small-Signal Stability – A Case Study on Australian

Equivalent System," vol. 4072, 2011.

[17] H. R. Chamorro, S. Member, M. Ghandhari, and R. Eriksson, "Wind Power Impact on Power System Frequency Response," 2013.

[18] J. M. Mauricio, A. Marano, A. Gómez-Expósito, and J. L. M. Ramos, "Frequency regulation contribution through variable-speed wind energy conversion systems," *IEEE Trans. Power Syst.*, vol. 24, no. 1, pp. 173–180, 2009.

[19] J. Licari, J. Ekanayake, and I. Moore, "Inertia response from full-power converter-based permanent magnet wind generators," *J. Mod. Power Syst. Clean Energy*, vol. 1, no. 1, pp. 26–33, 2013.

[20] C. Pradhan, C. N. Bhende, and A. K. Samanta, "Adaptive virtual inertia-based frequency regulation in wind power systems," *Renew. Energy*, vol. 115, pp. 558–574, Jan. 2018.

[21] A. Berizzi, A. Bolzoni, A. Bosisio, V. Ilea, D. Marchesini, R. Perini, and A. Vicario, "Synthetic Inertia from Wind Turbines for Large System Stability," *Proc. - 2020 IEEE Int. Conf. Environ. Electr. Eng. 2020 IEEE Ind. Commer. Power Syst. Eur. EEEIC / I CPS Eur. 2020*, 2020.

[22] J. F. Conroy and R. Watson, "Frequency response capability of full converter wind turbine generators in comparison to conventional generation," *IEEE Trans. Power Syst.*, vol. 23, no. 2, pp. 649–656, 2008.

[23] Y. Wang, J. Meng, X. Zhang, and L. Xu, "Control of PMSG-Based Wind Turbines for System Inertial Response and Power Oscillation Damping," *IEEE Trans. Sustain. Energy*, vol. 6, no. 2, pp. 565–574, 2015.

[24] Z. Wu, W. Gao, T. Gao, W. Yan, H. Zhang, S. Yan, and X. Wang, "State-of-the-art review on frequency response of wind power plants in power systems," *J. Mod. Power Syst. Clean Energy*, vol. 6, no. 1, pp. 1–16, 2018.

[25] L. R. Chang-Chien, W. T. Lin, and Y. C. Yin, "Enhancing frequency response control by DFIGs in the high wind penetrated power systems," *IEEE Trans. Power Syst.*, vol. 26, no. 2, pp. 710–718, May 2011.

[26] X. Zeng, T. Liu, S. Wang, Y. Dong, and Z. Chen, "Comprehensive Coordinated Control Strategy of PMSG-Based Wind Turbine for Providing Frequency Regulation Services," *IEEE Access*, vol. 7, pp. 63944–63953, 2019.

[27] J. Zhu, J. Hu, W. Hung, C. Wang, X. Zhang, S. Bu, Q. Li, H. Urdal, and C. D. Booth, "Synthetic Inertia Control Strategy for Doubly Fed Induction Generator Wind Turbine Generators Using Lithium-Ion Supercapacitors," *IEEE Trans. Energy Convers.*, vol. 33, no. 2, pp. 773–783, 2018.

[28] U. Datta, A. Kalam, and J. Shi, "Battery Energy Storage System for Aggregated Inertia-Droop Control and a Novel Frequency Dependent State-of-Charge Recovery," *Energies*, vol. 13, no. 8, p. 2003, Apr. 2020.

[29] X. Zhang, X. Zha, S. Yue, and Y. Chen, "A Frequency Regulation Strategy for Wind Power Based on Limited Over-Speed De-Loading Curve Partitioning," *IEEE Access*, vol. 6, pp. 22938–22951, 2018.

[30] F. Díaz-González, M. Hau, A. Sumper, and O. Gomis-Bellmunt, "Participation of wind power plants in system frequency control: Review of grid code requirements and control methods," *Renew. Sustain. Energy Rev.*, vol. 34, pp. 551–564, 2014.

[31] M. Garmroodi, G. Verbic, and D. J. Hill, "Frequency Support from Wind Turbine Generators with a Time-Variable Droop Characteristic," *IEEE Trans. Sustain. Energy*, vol. 9, no. 2, pp. 676–684, 2018.

[32] Z. S. Zhang, Y. Z. Sun, J. Lin, and G. J. Li, "Coordinated frequency regulation by doubly fed induction generator-based wind power plants," *IET Renew. Power Gener.*, vol. 6, no. 1, pp. 38–

47, 2012.

[33] M. Dreidy, H. Mokhlis, and S. Mekhilef, “Inertia response and frequency control techniques for renewable energy sources: A review,” *Renewable and Sustainable Energy Reviews*, vol. 69. pp. 144–155, Mar-2017.

[34] H. Liu and Z. Chen, “Contribution of VSC-HVDC to Frequency Regulation of Power Systems With Offshore Wind Generation,” *IEEE Trans. Energy Convers.*, vol. 30, no. 3, pp. 918–926, Sep. 2015.

[35] G. Lalor, J. Ritchie, S. Rourke, D. Flynn, and M. J. O’Malley, “Dynamic frequency control with increasing wind generation,” *IEEE Power Eng. Soc. Gen. Meet. 2004.*, pp. 1715–1720, 2005.

[36] Gabriele Michalke, “Variable Speed Wind Turbines-Modelling, Control, and Impact on Power Systems,” Darmstadt University of technology, Darmstadt, 2008.

[37] M. Pöller and S. Achilles, “Aggregated Wind Park Models for Analyzing Power System Dynamics,” *4th Int. Work. Large-scale Integr. Wind Power Transm. Networks Offshore Wind Farms*, pp. 1–10, 2003.

[38] J. F. Medina Padrón and A. E. Feijóo Lorenzo, “Calculating steady-state operating conditions for doubly-fed induction generator wind turbines,” *IEEE Trans. Power Syst.*, vol. 25, no. 2, pp. 922–928, 2010.

[39] P. Tielens and D. Van Hertem, “The relevance of inertia in power systems,” *Renew. Sustain. Energy Rev.*, vol. 55, no. 2016, pp. 999–1009, 2016.

[40] J. M. Carrasco, L. G. Franquelo, J. T. Bialasiewicz, E. Galván, R. C. Portillo Guisado, M. Á. M. Prats, J. I. León, and N. Moreno-Alfonso, “Power-electronic systems for the grid integration of renewable energy sources: A survey,” *IEEE Trans. Ind. Electron.*, vol. 53, no. 4, pp. 1002–1016, 2006.

[41] F. Blaabjerg, Z. Chen, and S. B. Kjaer, “Power electronics as efficient interface in dispersed power generation systems,” *IEEE Trans. Power Electron.*, vol. 19, no. 5, pp. 1184–1194, 2004.

[42] B. Singh, B. N. Singh, A. Chandra, K. Al-Haddad, A. Pandey, and D. P. Kothari, “A review of three-phase improved power quality ac-dc converters,” *IEEE Trans. Ind. Electron.*, vol. 51, no. 3, pp. 641–660, 2004.

[43] H. Wang and F. Blaabjerg, “Reliability of capacitors for DC-link applications in power electronic converters - An overview,” *IEEE Trans. Ind. Appl.*, vol. 50, no. 5, pp. 3569–3578, 2014.

[44] E. Rakhshani and P. Rodriguez, “Inertia Emulation in AC / DC Interconnected Power,” *Ieee Trans. Power Syst.*, vol. 32, no. 5, pp. 3338–3351, 2017.

[45] J. Fang, R. Zhang, H. Li, and Y. Tang, “Frequency Derivative-based Inertia Enhancement by Grid-Connected Power Converters with a Frequency-Locked-Loop,” *IEEE Trans. Smart Grid*, vol. 10, no. 5, pp. 4918–4927, 2018.

[46] S. Yang, J. Fang, Y. Tang, H. Qiu, C. Dong, and P. Wang, “Modular Multilevel Converter Synthetic Inertia-Based Frequency Support for Medium-Voltage Microgrids,” *IEEE Trans. Ind. Electron.*, vol. 66, no. 11, pp. 8992–9002, 2019.

[47] A. Bolzoni and R. Perini, “Feedback Couplings Evaluation on Synthetic Inertia Provision for Grid Frequency Support,” *IEEE Trans. Energy Convers.*, vol. 8969, no. c, pp. 1–1, 2020.

[48] Y. Li, Z. Xu, and K. P. Wong, “Advanced Control Strategies of PMSG-Based Wind Turbines for System Inertia Support,” *IEEE Trans. Power Syst.*, vol. 32, no. 4, pp. 3027–3037, 2017.

[49] J. Fang, H. Li, Y. Tang, and F. Blaabjerg, “Distributed Power System Virtual Inertia Implemented by Grid-Connected Power Converters,” *IEEE Trans. Power Electron.*, vol. 33, no. 10, pp. 8488–8499, 2018.

[50] S. Wang, J. Hu, X. Yuan, and L. Sun, “On Inertial Dynamics of Virtual-Synchronous-Controlled DFIG-Based Wind Turbines,” *IEEE Trans. Energy Convers.*, vol. 30, no. 4, pp. 1691–1702, 2015.

[51] M. Merai, M. W. Naouar, I. Slama-Belkhodja, and E. Monmasson, “Grid connected converters as reactive power ancillary service providers: Technical analysis for minimum required DC-link voltage,” *Math. Comput. Simul.*, vol. 158, pp. 344–354, 2019.

[52] C. Y. Tang, Y. F. Chen, Y. M. Chen, and Y. R. Chang, “DC-Link Voltage Control Strategy for Three-Phase Back-to-Back Active Power Conditioners,” *IEEE Trans. Ind. Electron.*, vol. 62, no. 10, pp. 6306–6316, 2015.

[53] Y. Wang, Y. Wang, S. Z. Chen, G. Zhang, and Y. Zhang, “A simplified minimum DC-link voltage control strategy for shunt active power filters,” *Energies*, vol. 11, no. 9, p. 2407, Sep. 2018.

[54] S. I. Abouzeid, Y. Guo, and H. C. Zhang, “Dynamic control strategy for the participation of variable speed wind turbine generators in primary frequency regulation,” *J. Renew. Sustain. Energy*, vol. 11, no. 1, 2019.

[55] X. Zhao and Y. Xue, “Systems by Arresting Frequency Nadir Close to Settling Frequency,” vol. 7, no. February, 2020.

[56] Y. Fu, Y. Wang, and X. Zhang, “Integrated wind turbine controller with virtual inertia and primary frequency responses for grid dynamic frequency support,” *IET Renewable Power Generation*, vol. 11, no. 8. pp. 1129–1137, 2017.

[57] N. A. Janssens, G. Lambin, and N. Bragard, “Active power control strategies of DFIG wind turbines,” *2007 IEEE Lausanne POWERTECH, Proc.*, no. July, pp. 516–521, 2007.

[58] Z. A. Styczynski, P. Lombardi, R. Seethapathy, and M. Piekutowski, “Electric Energy Storage and its tasks in the integration of wide-scale renewable resources.,” *Proc. Integr. Wide-Scale Renew. Resour. into Power Deliv. Syst.*, 2009.

[59] I. Hadjipaschalis, A. Poullikkas, and V. Efthimiou, “Overview of current and future energy storage technologies for electric power applications,” *Renew. Sustain. Energy Rev.*, vol. 13, no. 6–7, pp. 1513–1522, 2009.

[60] C. A. Hill, M. C. Such, D. Chen, J. Gonzalez, and W. M. K. Grady, “Battery energy storage for enabling integration of distributed solar power generation,” *IEEE Trans. Smart Grid*, vol. 3, no. 2, pp. 850–857, 2012.

[61] X. Luo, J. Wang, M. Dooner, and J. Clarke, “Overview of current development in electrical energy storage technologies and the application potential in power system operation,” *Appl. Energy*, vol. 137, pp. 511–536, 2015.

[62] Aurecon, “Hornsdale Power Reserve Year 1 Technical and Market Impact Case Study,” 2018.

[63] VISTRA Energy B., “Annual Sustainability Report 2018,” 2018.

[64] G. Mandic, A. Nasiri, E. Ghotbi, and E. Muljadi, “Lithium-ion capacitor energy storage integrated with variable speed wind turbines for power smoothing,” *IEEE J. Emerg. Sel. Top. Power Electron.*, vol. 1, no. 4, pp. 287–295, 2013.

[65] M. F. M. Arani and E. F. El-Saadany, “Implementing virtual inertia in DFIG-based wind power generation,” *IEEE Trans. Power Syst.*, vol. 28, no. 2, pp. 1373–1384, 2013.

[66] Y. Ma, Z. Lin, R. Yu, and S. Zhao, “Research on improved VSG control algorithm based on capacity-limited energy storage system,” *Energies*, vol. 11, no. 3, 2018.

[67] M. Ghofrani, A. Arabali, M. Etezadi-Amoli, and M. S. Fadali, “A framework for optimal placement of energy storage units within a power system with high wind penetration,” *IEEE Trans. Sustain. Energy*, vol. 4, no. 2, pp. 434–442, 2013.

[68] B. Weise, A. Korai, and A. Constantin, “Comparison of Selected Grid-Forming Converter Control

Strategies for Use in Power Electronic Dominated Power Systems," *18th Wind Integr. Work.*, no. October, pp. 16–18, 2019.

[69] U. Tamrakar, D. Shrestha, M. Maharjan, B. Bhattarai, T. Hansen, and R. Tonkoski, "Virtual Inertia: Current Trends and Future Directions," *Appl. Sci.*, vol. 7, no. 7, p. 654, 2017.

[70] Cigre Technical Brochure 604, "Guide for the Development of Models for HVDC Converters in a HVDC Grid," 2014.

[71] Q. C. Zhong, P. L. Nguyen, Z. Ma, and W. Sheng, "Self-synchronized synchronverters: Inverters without a dedicated synchronization unit," *IEEE Trans. Power Electron.*, vol. 29, no. 2, pp. 617–630, 2014.

[72] Q. C. Zhong, "Virtual Synchronous Machines: A unified interface for grid integration," *IEEE Power Electron. Mag.*, vol. 3, no. 4, pp. 18–27, 2016.

[73] J. Van De Vyver, J. D. M. De Kooning, B. Meersman, L. Vandevelde, and T. L. Vandoorn, "Droop Control as an Alternative Inertial Response Strategy for the Synthetic Inertia on Wind Turbines," *IEEE Trans. Power Syst.*, vol. 31, no. 2, pp. 1129–1138, 2016.

[74] Y. K. Wu, W. H. Yang, Y. L. Hu, and P. Q. Dzung, "Frequency regulation at a wind farm using time-varying inertia and droop controls," *IEEE Trans. Ind. Appl.*, vol. 55, no. 1, pp. 213–224, 2019.

[75] C. Pradhan and C. Bhende, "Enhancement in Primary Frequency Contribution using Dynamic Deloading of Wind Turbines," *IFAC-PapersOnLine*, vol. 48, no. 30, pp. 13–18, Jan. 2015.

[76] K. V. Vidyanandan and N. Senroy, "Primary frequency regulation by deloaded wind turbines using variable droop," *IEEE Trans. Power Syst.*, vol. 28, no. 2, pp. 837–846, 2013.

[77] S. Ghosh, S. Kamalasadan, N. Senroy, and J. Enslin, "Doubly fed induction generator (DFIG)-based wind farm control framework for primary frequency and inertial response application," *IEEE Trans. Power Syst.*, vol. 31, no. 3, pp. 1861–1871, 2016.

[78] M. Saeed Uz Zaman, S. B. A. Bukhari, R. Haider, M. O. Khan, S. Baloch, and C. H. Kim, "Sensitivity and stability analysis of power system frequency response considering demand response and virtual inertia," *IET Gener. Transm. Distrib.*, vol. 14, no. 6, pp. 986–996, 2020.

[79] DIgSILENT GmbH, "39 bus New England system," pp. 1–16, 2018.

[80] J. Ma, Y. Qiu, Y. Li, W. Zhang, Z. Song, and J. S. Thorp, "Research on the impact of DFIG virtual inertia control on power system small-signal stability considering the phase-locked loop," *IEEE Trans. Power Syst.*, vol. 32, no. 3, pp. 2094–2105, May 2017.

[81] E. Lucas, D. Campos-Gaona, and O. Anaya-Lara, "Assessing the impact of DFIG synthetic inertia provision on power system small-signal stability," *Energies*, vol. 12, no. 18, 2019.

[82] W. Du, Q. Fu, and H. F. Wang, "Power System Small-Signal Angular Stability Affected by Virtual Synchronous Generators," *IEEE Trans. Power Syst.*, vol. 34, no. 4, pp. 3209–3219, 2019.

[83] J. Liu, Z. Yang, J. Yu, J. Huang, and W. Li, "Coordinated control parameter setting of DFIG wind farms with virtual inertia control," *Int. J. Electr. Power Energy Syst.*, vol. 122, no. February, p. 106167, 2020.

[84] S. Pizarro-Gálvez, H. Pulgar-Painemal, and V. Hinojosa-Mateus, "Parameterized Modal Analysis Using DIgSILENT Programming Language," in *PowerFactory applications for power system analysis*, Springer, 2014, pp. 221–248.

[85] "Home - Osmose." [Online]. Available: https://www.osmose-h2020.eu/. [Accessed: 22-Sep-2021].

[86] J. Weibezahn, L. Göke, L. Orrù, N. Grisey, "European Long-Term Scenarios Description," no. 773406, 2019.

[87] N. Grisey and J. Bourmaud, “T.1.2 - Optimal Mix of Flexibility. Internal document. Description of the E-highway 2030 grid clustering,” 2020.

[88] P. Kundur, *Power System Stability and Control*. McGraw-Hill, 1994.